PB-239 323

INVARIANT MODELING OF TURBULENCE AND DIFFUSION IN THE PLANETARY BOUNDARY LAYER

W. S. Lewellen, et al

Aeronautical Research Associates of Princeton, Incorporated

Prepared for:

National Environmental Research Center

September 1974

DISTRIBUTED BY:

NTIS

National Technical Information Service
U. S. DEPARTMENT OF COMMERCE

TECHNICAL REPORT DATA
(Please read Instructions on the reverse before completing)

1. REPORT NO.	2.	3. RE PB 239 323
EPA-650/4-74-035		

4. TITLE AND SUBTITLE	5. REPORT DATE
Invariant Modeling of Turbulence and Diffusion in the Planetary Boundary Layer	September 1974
	6. PERFORMING ORGANIZATION CODE

7. AUTHOR(S)	8. PERFORMING ORGANIZATION REPORT NO.
R. Contiliano, W.S. Lewellen, G. Hilst, M. Teske, C. duP. Donaldson	A.R.A.P. No. 225

9. PERFORMING ORGANIZATION NAME AND ADDRESS	10. PROGRAM ELEMENT NO.
Aeronautical Research Associates of Princeton, Inc. 50 Washington Road, Princeton, New Jersey 08540	1AA009
	11. CONTRACT/GRANT NO. EPA 68-02-1310

12. SPONSORING AGENCY NAME AND ADDRESS	13. TYPE OF REPORT AND PERIOD COVERED
Office of Research and Development U.S. Environmental Protection Agency Washington, D. C. 20460	Interim
	14. SPONSORING AGENCY CODE

15. SUPPLEMENTARY NOTES

16. ABSTRACT

Significant progress has been made at A.R.A.P. over the last year toward the goal of developing a viable computer model based on second-order closure of the turbulent correlation equations for predicting the fate of nonchemically reacting contaminants released in the atmospheric boundary layer. The invariant turbulent model discussed in previous reports has been modified both by extending its capabilities and by developing approximations to the full system of equations which may be used in complicated flow geometries where economy of computing time justifies some compromise in accuracy. Sample calculations of several flow problems of current practical interest are included. These are: that of the diurnal variations in the turbulence distributions in the planetary boundary layer induced by the unsteady surface heat flux; the spatial variation of turbulence occurring when the wind blows over an abrupt change in surface roughness; and the dispersal of a plume released at different heights, under different stability conditions, and over different terrain.

PRICES SUBJECT TO CHANGE

17. KEY WORDS AND DOCUMENT ANALYSIS

a. DESCRIPTORS	b. IDENTIFIERS/OPEN ENDED TERMS	c. COSATI Field/Group
Atmospheric turbulence Planetary boundary layer Pollutant dispersal Turbulence models Atmospheric motion Plume meandering	Second-order closure modeling of turbulence Diurnal variations in the planetary boundary layer Atmospheric stability influences on pollutant dispersal	

18. DISTRIBUTION STATEMENT	19. SECURITY CLASS (This Report)	21. NO. OF PAGES
Reproduced by NATIONAL TECHNICAL INFORMATION SERVICE US Department of Commerce Springfield, VA. 22151	unclassified	115
	20. SECURITY CLASS (This page) unclassified	22. PRICE 5.25-2.25

EPA Form 2220-1 (9-73)

EPA-650/4-74-035

INVARIANT MODELING OF TURBULENCE AND DIFFUSION IN THE PLANETARY BOUNDARY LAYER

by

W. S. Lewellen, M. Teske,
R. Contiliano, G. Hilst, C. duP. Donaldson

Aeronautical Research Associates of Princeton, Inc.
50 Washington Road
Princeton, N. J. 08540

Contract No. 68-02-1310
ROAP No. 21ADO
Program Element No. 1AA009

EPA Project Officer: Douglas G. Fox

Meteorology Laboratory
National Environmental Research Center
Research Triangle Park, North Carolina 27711

Prepared for

OFFICE OF RESEARCH AND DEVELOPMENT
U. S. ENVIRONMENTAL PROTECTION AGENCY
WASHINGTON, D.C. 20460

September 1974

This report has been reviewed by the Environmental Protection Agency and approved for publication. Approval does not signify that the contents necessarily reflect the views and policies of the Agency, nor does mention of trade names or commercial products constitute endorsement or recommendation for use.

ABSTRACT

Significant progress has been made at A.R.A.P. over the last year toward the goal of developing a viable computer model based on second-order closure of the turbulent correlation equations for predicting the fate of nonchemically reacting contaminants released in the atmospheric boundary layer. The invariant turbulent model discussed in previous reports has been modified both by extending its capabilities and by developing approximations to the full system of equations which may be used in complicated flow geometries where economy of computing time justifies some compromise in accuracy. Sample calculations of several flow problems of current practical interest are included. These are: that of the diurnal variations in the turbulence distributions in the planetary boundary layer induced by the unsteady surface heat flux; the spatial variation of turbulence occurring when the wind blows over an abrupt change in surface roughness; and the dispersal of a plume released at different heights, under different stability conditions, and over different terrain.

CONTENTS

		Page
Abstract		ii
List of Figures		iv
Sections		
I	Conclusions	1
II	Recommendations	2
III	Introduction	3
IV	Modifications of the Turbulent Model	5
V	Modifications to the Pollutant Dispersal Model	20
VI	Sample Calculations and Model Verification	39
VII	References	81
VIII	Nomenclature	84
IX	Appendix	3[illegible]

FIGURES

No.		Page
1	Macroscale variation with height for a neutral planetary boundary layer as given by the dynamic equation, eq. (24); and by the gross features of the flow, eq. (25).	13
2	Velocity distributions in the neutral planetary boundary layer (z_o = .0774 m, $f = 10^{-4}$ sec^{-1}, u_g = 10 m/sec) computed from the quasi-equilibrium approximation (——) and from the full set (— —).	17
3	Dynamic response of variables within the planetary boundary layer to an increase in the surface heat flux as predicted by the full equations, and by the quasi-equilibrium set.	18
4	Comparison of numerical and analytical predictions for one-dimensional wave propagation.	26
5	Comparison of numerical and analytical predictions for one-dimensional diffusion.	27
6	Comparison of numerical and analytical predictions for one-dimensional diffusion far downstream of the release point.	28
7	Plume scale as a function of the proportionality constant in eq. (52).	31
8	Centerline plume concentration normalized by the local maximum concentration plotted as a function of distance from the release point for various values of the scale factor β.	32

No.		Page
9	Mean concentration profiles 100 m downstream of a Gaussian plume release for different values of scale factor β. ($u = 10$ m/sec, $\overline{w'w'} = 1$ m^2/sec^2, $q^2 = 3$ m^2/sec^2, neutral stability, $\sigma_1 = 1$ m, $C_{max_1} = 1$).	33
10	Mean concentration profiles at 1 km for the same conditions as fig. 9.	34
11	Mean concentration profiles at 10 km for the same conditions as fig. 9.	35
12	Influence of initial values of $\overline{C'w'}$ on subsequent distortion of the concentration profiles.	37
13	Comparison of velocity distributions in the neutral planetary boundary layer ($z_o = 0.008$ m, $f = 10^{-4}$ sec^{-1}, $u_g = 10$ m/sec) as predicted by the model with dynamic scale equation with Deardorff's model predictions (---)(ref. 15).	40
14	Surface shear velocity as a function of time for a diurnal surface heat variation as predicted by a calculation using the dynamic scale equation (compare with fig. A9).	43
15	Contours of constant q^2 as a function of altitude and time of day as predicted by the model using the dynamic scale equation (compare with fig. A4).	44
16	Contours of constant length scale Λ as a function of altitude and time of day as predicted by the model using the dynamic scale equation (compare with fig. A8).	45
17	Surface shear stress as a function of distance downwind of a step change in surface roughness as predicted by the model (---) and as observed by Bradley (o)(ref. 18).	47
18	Contours of constant shear stress in the vicinity of a change in roughness from 0.002 m to 0.25 m ($u_g = 10$ m/sec, neutral stability).	48
19	Atmospheric conditions assumed for the unstable plume calculations.	50

No.		Page
20	Decay of maximum concentration as a function of distance downwind of an effective 100 m stack in atmospheric conditions prescribed by fig. 19.	51
21	Contours of constant mean concentration at various distances downstream of a 100 m stack in atmospheric conditions prescribed by fig. 19 a) x = 0 m, b) x = 10 m, c) x = 50 m, d) x = 250 m, e) x = 500 m, f) x = 1 km (the contours are labeled with 9 = 90% of maximum, 7 = 70%, etc.).	52
22	The same information as supplied in fig. 21 with the concentration profiles now shown in perspective. Note the scale changes at different x stations.	55
23	Standard deviation of the unstable plume as a function of distance downwind of release point.	61
24	Ratio of meander area to instantaneous plume area as a function of distance downwind of release as predicted by the model for unstable conditions and as observed by Wasko and Moses[22].	62
25	Contours of constant values of $\overline{C'C'}$ at the same x stations as given in fig. 21.	64
26	Atmospheric conditions assumed for the stable plume calculation.	66
27	Decay of maximum mean concentration as a function of distance downwind of a 100 m stack in atmospheric conditions prescribed by fig. 26.	67
28	Contours of constant mean concentration at various distances downstream of a 100 m stack in a stable atmosphere. a) x = 0, b) x = 10 m, c) x = 50 m, d) x = 100 m, e) x = 250 m, f) x = 500 m, g) x = 5000 m, h) x = 10,000 m, i) x = 20,000 m.	68
29	Contours of constant values of $\overline{C'C'}$ at the same x stations as given in fig. 28.	72

No.		Page
30	Decay of maximum concentration as a function of distance downwind of three different stack heights in an unstable atmosphere.	75
31	Ground level maximum mean concentration as a function of distance downwind of three different stack heights.	76
32	Maximum ground level mean concentration plotted as a function of effective stack height.	77
33	Decay of maximum concentration as a function of distance downwind of a 100 m stack in a neutral atmosphere. Plume A is released directly above an abrupt change in surface roughness (from z_o = .002 m to z_o = .25 m) and Plume B is released far downstream of the change in roughness.	79
34	Ground level contours of mean concentration for Plumes A and B of fig. 33.	80

SECTION I

CONCLUSIONS

We believe that significant progress has been made toward our goal of developing a viable computer model for predicting the fate of nonchemically reacting pollutants released in the atmospheric boundary layer. We have both strengthened the foundation of our model and increased its capability. This is not to imply that the turbulence model is cast in concrete at this point. Rather, we expect continual modification, particularly with respect to the treatment of the scale as more and better experimental data becomes available. However, the sample calculations of several flow problems of practical interest presented in Section VI demonstrate that the model is currently capable of providing results directly useful to EPA.

More specifically, interesting conclusions from the sample calculations are that:

1. There are significant unsteady influences on the surface shear stress induced by the planetary boundary layer on a typical day which cannot be predicted as a function of stability alone. The surface shear stress under neutral surface conditions can vary as much as a factor of two between conditions where the surface heat flux is increasing or decreasing.

2. The same model of turbulence is capable of computing the dispersing plume during both its early time meandering phase and its late time diffusive phase.

3. For a single plume with an effective stack height of 100 m the maximum mean ground level concentration will occur around noon for the turbulence field predicted by the diurnal calculation.

4. Model predictions for shear stress distribution in the neighborhood of an abrupt change in surface roughness agree with atmospheric surface data.

5. Model predictions of plume dispersion from different stack heights show a dependence (close to a -2 power law) of maximum ground concentration on effective stack height.

SECTION II

RECOMMENDATIONS

In order for EPA to gain maximum advantage from this program we recommend that the coupled set of equations for turbulence generation and diffusion be programmed to run on EPA's UNIVAC 1110 computer. The development of the turbulence generation model to this point in time has been limited to two-dimensional situations with one of these dimensions time or a streaming direction in which the program can march. With the confidence gained in verifying the model results with experimental data, it now appears appropriate to upgrade the model capability by adding an additional dimension to simulate a three-dimensional problem with the variables parabolic in one dimension. The pollutant dispersal model presently capable of computing such 3-D problems can be directly coupled to the turbulence program. This extended model would require a few hours to run on our company computer (Digital Scientific Corporation's META-4), but should only require a few minutes on the UNIVAC 1110.

It is also important to carry through a number of model calculations of plume dispersal to determine under what conditions the standard Gaussian plume assumptions lead to unacceptable error.

SECTION III

INTRODUCTION

The goal of our research is the development of a viable computer model for predicting the fate of nonchemically reacting contaminants released in the atmosphere. Since most atmospheric pollutants are released within one kilometer of the earth's surface, this necessitates also developing a reasonably accurate model for computing the distributions of winds and turbulent fluctuations within the planetary boundary layer. This report details the progress made at A.R.A.P. towards this goal in the past year.

Our approach is to use the Reynolds stress equations to compute the turbulent fluctuations with invariant modeling techniques applied to close the system of equations. Details of this approach have been given by Donaldson [1, 2]. The basic assumption is that the dependence of third-order correlations of the velocity fluctuations on the second-order correlations, the mean flow properties and their derivatives, is invariant with respect to changes in the flow geometry. This permits data from relatively simple flow experiments to be used in evaluating the necessary coefficients in the modeled terms.

The previous report presented the derivation of the set of equations on which the A.R.A.P. model of atmospheric turbulence and pollutant transport is based. It included a discussion of the process used to obtain the closure model and the values of the basic model coefficients. It also contained some typical examples of computations as well as a discussion of the relationship of our second-order closure model to first-order, eddy diffusivity models.

In the past year we have extended the capability of our model in several significant ways: by incorporating a dynamic scale equation when necessary; by incorporating the capability for boundary conditions varying in either time or one dimension of space; and by incorporating the capability to compute the dispersing plume in its meandering phase. We have also strengthened the foundation of our model by further comparisons with field data and have developed approximations to our

full system of equations that with some slight degree of approximation may be used in more complicated flow geometries where economy of computing time dictates a simpler method.

In addition to detailing the model extensions, we include in the following sections sample calculations of several flow problems that are of current practical interest: that of the diurnal variations in the turbulence distributions in the planetary boundary layer; the spatial distribution of turbulence occurring when the wind blows over an abrupt change in surface roughness; and the dispersal of a plume released at different heights in the boundary layer at different times of the day over different terrain.

SECTION IV

MODIFICATIONS OF THE TURBULENT MODEL

When the Boussinesq approximation for density variations is used, the mean flow equations and the Reynolds stress equations may be written as (See ref. 1 for a derivation of these equations.):

$$\frac{Du_i}{Dt} = -\frac{\partial}{\partial x_j}\overline{u_i'u_j'} + \frac{\partial}{\partial x_j}\left(\nu\frac{\partial u_i}{\partial x_j}\right) - \frac{1}{\rho}\frac{\partial p}{\partial x_i} + \frac{g_i\theta}{T_o} - 2\epsilon_{ijk}\Omega_j u_k \tag{1}$$

$$\frac{\partial u_i}{\partial x_i} = 0 \tag{2}$$

$$\frac{D\theta}{Dt} = -\frac{\partial\overline{u_i'\theta'}}{\partial x_i} - \dot{Q} + \frac{\partial}{\partial x_i}\left(\kappa\frac{\partial\theta}{\partial x_i}\right) \tag{3}$$

$$\begin{aligned}\frac{D\overline{u_i'u_j'}}{Dt} = &-\overline{u_i'u_k'}\frac{\partial u_j}{\partial x_k} - \overline{u_j'u_k'}\frac{\partial u_i}{\partial x_k} + \frac{g_i}{T_o}\overline{u_j'\theta'} + \frac{g_j\overline{u_i'\theta'}}{T_o}\\ &- \frac{\partial}{\partial x_k}\left(\overline{u_k'u_i'u_j'}\right) - \frac{1}{\rho}\frac{\partial\overline{p'u_i'}}{\partial x_j} - \frac{1}{\rho}\frac{\partial\overline{p'u_j'}}{\partial x_i} + \overline{\frac{p'}{\rho}\left(\frac{\partial u_i'}{\partial x_j} + \frac{\partial u_j'}{\partial x_i}\right)}\\ &+ \nu\frac{\partial^2\overline{u_i'u_j'}}{\partial x_k^2} - 2\nu\overline{\frac{\partial u_i'}{\partial x_k}\frac{\partial u_j'}{\partial x_k}} - 2\epsilon_{ik\ell}\Omega_k\overline{u_\ell'u_j'} - 2\epsilon_{j\ell k}\Omega_\ell\overline{u_k'u_i'}\end{aligned} \tag{4}$$

$$\frac{D\overline{u_i'\theta'}}{Dt} = - \overline{u_i'u_j'} \frac{\partial\theta}{\partial x_j} - \overline{\theta'u_j'} \frac{\partial u_i}{\partial x_j} - \frac{\partial(\overline{\theta'u_i'u_j'})}{\partial x_j} - \frac{1}{\rho} \frac{\partial}{\partial x_i} (\overline{p'\theta'})$$

$$+ \overline{\frac{p'}{\rho} \frac{\partial\theta'}{\partial x_i}} + \overline{\theta'^2} \frac{g_i}{T_o} - \overline{\nu\theta' \frac{\partial^2 u_i'}{\partial x_j^2}} - \overline{\kappa u_i' \frac{\partial^2\theta'}{\partial x_j^2}}$$

$$- 2\epsilon_{ijk} \Omega_j \overline{u_k'\theta'} \qquad (5)$$

$$\frac{D\overline{\theta'^2}}{Dt} = - 2\overline{u_j\theta'} \frac{\partial\theta}{\partial x_j} - \frac{\partial}{\partial x_j} \overline{u_j\theta'^2} + \kappa \frac{\partial^2\overline{\theta'^2}}{\partial x_j^2} - 2\kappa \overline{\frac{\partial\theta'}{\partial x_j} \frac{\partial\theta'}{\partial x_j}} \qquad (6)$$

The closure model we currently use to close this system may be written as:

$$\frac{\partial}{\partial x_k} (\overline{u_i'u_j'u_k'}) + \frac{1}{\rho} \overline{\frac{\partial p'u_j'}{\partial x_i}} + \frac{1}{\rho} \overline{\frac{\partial p'u_i'}{\partial x_j}} = - V_c \frac{\partial}{\partial x_k} q\Lambda \overline{\frac{\partial u_i'u_j'}{\partial x_k}} \qquad (7)$$

$$\overline{\frac{p'}{\rho} \left(\frac{\partial u_i'}{\partial x_j} + \frac{\partial u_j'}{\partial x_i} \right)} = - \frac{q}{\Lambda} \left(\overline{u_i'u_j'} - \frac{\delta_{ij}q^2}{3} \right) \qquad (8)$$

$$\overline{\frac{\partial u_i'}{\partial x_k} \frac{\partial u_j'}{\partial x_k}} = \frac{\delta_{ij}q^2}{3\lambda^2}$$

$$+ \frac{a}{\Lambda^2} \left(\overline{u_i'u_j'} - \frac{\delta_{ij}q^2}{3} \right) \qquad (9)$$

$$\overline{\frac{\partial\theta'}{\partial x_i} \frac{\partial\theta'}{\partial x_i}} = s \frac{\overline{\theta'^2}}{\lambda^2} \qquad (10)$$

$$\overline{\frac{p'}{\rho} \frac{\partial\theta'}{\partial x_i}} = - \frac{A_1 q}{\Lambda} \overline{u_i'\theta'} \qquad (11)$$

This model differs slightly from that used in the calculations of refs. 1 and 2. Velocity and pressure diffusion in eq. (7) are combined into one simple gradient diffusion term requiring only one coefficient rather than the two of the previous model. This present model will be used until some experimental evidence provides the information required to evaluate the coefficients in the more elaborate expression. The model of the dissipation term (eq. (9)) has been modified so that for very high Reynolds numbers when $\lambda \ll \Lambda$ dissipation will be isotropic. The coefficients s and A_1 have been added to the temperature terms in eqs. (10) and (11). The desirability of this generalization was indicated by comparing model predictions with the experimentally determined Monin-Obukhov functions for turbulence in the atmospheric surface layer[3].

With $\lambda^2 = \Lambda^2/(a + bq\Lambda/\nu)$ the modeled equations contain five constant coefficients (a, b, V_c, s and A_1) and one model variable, Λ, the macroscale of the turbulence. The value of the coefficient a was chosen to be 2.5 in ref. 1, but some recent numerical experiments indicate that it may more properly be as high as 3.25 to obtain good agreement within the laminar sublayer of the flat plate boundary layer. The high Reynolds number of all of the flows considered in this report make the value of a inconsequential. The coefficient in the high Reynolds number dissipation term, b, may be determined to be approximately 1/8 by equating the dissipation terms to the production terms in the constant stress wall layer of a boundary layer. This value of b agrees with that chosen in ref. 1. The diffusion coefficient V_c is set equal to 0.3 by comparing model results with axisymmetric jets and wakes [4].

The remaining coefficients A_1 and s were chosen by comparison with measurements in the atmospheric surface layer[3]. Near the surface the turbulence equilibrates rapidly to any changing surface conditions and the flow may be considered steady, so that eqs. (1) to (3) reduce to the conditions that the shear stress and heat flux be independent of height. In this constant flux region eqs. (4) to (6) with the model terms from eqs. (7) to (11) lead to a set of ordinary differential equations as a function of the single dimensionless variable, the height z normalized by the Monin-Obukhov scale length. The parameter A_1 was chosen (= .75) to make the turbulent Prandtl number agree with observations for neutral conditions, and s was chosen (= 1.8) so that the temperature variance was properly scaled. Comparisons of the distributions as a function of stability for the variables $\partial u/\partial z$, $\partial\theta/\partial z$, $\overline{w'w'}$, $\overline{u'\theta'}$, $\overline{\theta'\theta'}$ with observations are given in ref. 3. All the comparisons are quite favorable.

The numerical technique used to solve our model equations was described in Appendix A of ref. 1. This fully implicit technique was used for all the solutions discussed in this report except for the numerical experiments described in Section V A.4.

A. ADDITION OF A SCALE EQUATION*

In all previous calculations using our turbulence model, the pertinent macroscale length Λ has been determined at any time by the gross features of the turbulence distribution, with no influence permitted on local conditions or past history. Other researchers have used a dynamic equation for their equivalent scale, such as may be obtained from modeling the dynamic equation for either the dissipation function[5], the two-point velocity correlations[1, 6], or the vorticity fluctuations[7]. As Bradshaw[8] and Mellor and Herring[9] have pointed out, when the turbulent energy equation is used to derive a scale equation, the principal terms in the resulting Λ are essentially the same for all formulations, namely

$$\frac{D\Lambda}{Dt} = - s_1 \frac{\Lambda}{q^2} \overline{u_i u_j} \frac{\partial u_i}{\partial x_j} - s_2 \frac{\nu\Lambda}{\lambda^2} + \text{diffusion terms} + \text{possible stratification terms} \qquad (12)$$

Constants s_1 and s_2 multiply the production and dissipation terms respectively. The principal difference in expressions lies in the construction of the turbulent diffusion terms, and unfortunately these turn out to be more important in the scale equation than in the Reynolds stress equations. Our approach has been to start with a rather general diffusion term of the form

$$\text{diffusion terms} = s_0 \frac{\partial}{\partial x_i}\left(V_c q\Lambda \frac{\partial \Lambda}{\partial x_i} \right) + s_3 \frac{\Lambda}{q^2} \frac{\partial}{\partial x_i}\left(q\Lambda \frac{\partial q^2}{\partial x_i} \right)$$

$$+ s_4 q \left(\frac{\partial \Lambda}{\partial x_i} \right)^2 + s_6 \frac{\Lambda}{q^2} \left(\frac{\partial q}{\partial x_i} \right)^2 + s_7 \Lambda \frac{\partial q}{\partial x_i} \frac{\partial \Lambda}{\partial x_i} \qquad (13)$$

As pointed out by Mellor and Herring[9] this covers the possibility of starting with equations for the quantity $q^m \Lambda^n$ and

*Work on this section was partially supported by DARPA through ONR Contract N00014-72-C-0413.

in combination with the energy equation reducing it to eq. (12). As in the formulations of refs. 1 and 7 we will add a term proportional to $(\Lambda/q^2)\, g_1 \overline{u_1'\theta'}/T_o$ to permit the direct effect of stratification.

It is immediately obvious that the scale equation contains much more arbitrariness than the Reynolds stress equations where many of the terms were determined precisely without recourse to modeling or coefficients. With such a large number of coefficients in the scale equation, a correspondingly large number of different experiments must be matched concurrently if the resulting coefficients are to have any invariant validity.

The coefficient s_2 may be estimated from the decay of homogeneous grid turbulence. If homogeneous turbulence is assumed to decay as

$$q^2 \sim x^{-n} \tag{14}$$

then from the q^2 equation

$$\Lambda = bq^3/\left(-\frac{1}{2} U \frac{\partial q^2}{\partial x}\right) \tag{15}$$

Equation (12) then leads to

$$s_2 = -\frac{U}{bq}\frac{\partial \Lambda}{\partial x} = -\frac{(2-n)}{n} \tag{16}$$

A recent review of grid turbulence experiments by Gad-el-Hak and Corrsin[10] shows values of n predominantly between 1 and 1.3 with more of the values lying near 1.25. This value of n gives a value of $s_2 = -0.6$.

To reduce the number of diffusion coefficients it is desirable to keep the coefficient of the direct diffusion term, s_0, the same as in the Reynolds stress equation. This calls for $s_0 = 1$. It is compatible with this assumption to take $s_3 = 0$, since with $s_0 = 1$ any combination of m and n for an expression of the form

$$\frac{Dq^m\Lambda^n}{Dt} - V_c \frac{\partial}{\partial x_i}\left(q\Lambda \frac{\partial q^m \Lambda^n}{\partial x_i}\right) \tag{17}$$

would lead to an equation for $D\Lambda/Dt$ with $s_3 = 0$.

A simple relationship between s_0, s_1, s_2 and s_4 may be obtained by looking at the reduced form of the scale equation in the steady, neutral, constant-shear-stress layer near a solid

boundary where we know that

$$\Lambda = \alpha z \tag{18}$$

with z the distance from the wall and α a constant set equal to approximately 0.6 in ref. 3. In this region the scale equation reduces to

$$0 = s_1 \frac{\alpha z u^{*2}}{q^2} \frac{\partial u}{\partial z} - s_2 bq + s_0 V_c q\alpha^2 - s_4 q\alpha^2 \tag{19}$$

which, with the aid of the energy equation, may be reduced to

$$s_4 = s_0 V_c + (b/\alpha^2)(s_1 - s_2) \tag{20}$$

An estimate for s_5, the coefficient of the stratification term, can be obtained from the stable, constant flux layer for Richardson number equal to its critical value, where both Λ and q become constant. Under these conditions the scale equation reduces to

$$0 = - s_1 \frac{\Lambda}{q^2} \overline{u'w'} \frac{\partial u}{\partial z} - s_2 bq + s_5 \frac{\Lambda}{q^2} \frac{g}{T_o} \overline{w'\theta'} \tag{21}$$

which, with the aid of the simplified Reynolds stress equations for this region[3], reduces to

$$s_5 = s_1 + \frac{bq^3}{u^{*3}\Lambda} (s_1 - s_2) \tag{22}$$

When the values of the parameters used in ref. 3 are chosen, this yields

$$s_5 = 5.6\, s_1 - 4.6\, s_2 \tag{23}$$

This leaves s_1, s_6, and s_7 to be determined by computer optimization. Prior to doing this we must determine boundary conditions for the scale.

The boundary conditions on the scale equation are not as straightforward as those on the Reynolds stress equations, since the scale need not go to zero at the free boundary of a region of turbulence. In fact, the eddies extending the farthest are expected to be the largest eddies present in the region. At a free boundary we therefore set Λ equal to some fraction of the spread of the region of turbulence. For axisymmetric problems a good choice appears

to be $\Lambda_{edge} = 0.4$ times the spread of the region of turbulence as measured by the radius of the region where q^2 equals 1/4 of its maximum value. This boundary condition is 2 times the algebraic approximation used everywhere for Λ in ref. 4. For a two-dimensional region of turbulence a value of $\Lambda_{edge} = 0.6$ times the spread of the region of turbulence seems to be appropriate. The other boundary condition is that near the surface of a solid boundary Λ should go to zero like α times the distance normal to the surface, consistent with eq. (18).

The edge boundary condition appears simpler if one chooses to use the dissipation equation, since $\epsilon = bq^3/\Lambda$ clearly approaches zero. However, this leaves Λ free to approach any value from 0 to ∞ as $q \to 0$ and no independent information is gained.

Since the production term is small for a momentumless wake, this provides a flow for estimating s_6 and s_7 to lie between 0.3 and 1. To reduce the uncertainty in these coefficients we have rather arbitrarily set $s_4 = s_6 = s_7/2$. The last coefficient may now be determined by computer fit with the free-jet result. As noted previously in ref. 4 we have some difficulty precisely fitting the free-jet data (possibly due to our simplified modeling of the pressure-strain terms) but $s_1 = -.35$ appears to provide a reasonable compromise. This is in the middle of the range of values used by Rodi[6] who found it necessary to vary his analogous coefficient from 1.2 to 2 (corresponding to varying s_1 in our case from - 1 to 0.6.)

With the above choices for the coefficients, our proposed scale equation becomes

$$\frac{D\Lambda}{Dt} = -0.35 \frac{\Lambda}{q^2} \overline{u_i' u_j'} \frac{\partial u_i}{\partial x_j} + 0.6 \frac{\nu}{\lambda^2} \Lambda + 0.3 \frac{\partial}{\partial x_i} q\Lambda \frac{\partial \Lambda}{\partial x_i}$$

$$- \frac{0.375}{q} \left(\frac{\partial q\Lambda}{\partial x_i} \right)^2 + \frac{0.8\Lambda}{q^2} \frac{g_i \overline{u_i' \theta'}}{T_o} \qquad (24)$$

As noted earlier, we cannot assign as high a confidence level to this equation as to our modeled Reynolds stress equations. In fact, it appears that unless the turbulence is far out of equilibrium, our previous approach[11] of simply limiting the Λ to be equal to the lowest of the three bounds

$$\text{i)}\quad \Lambda \leq 0.65\, z$$

$$\text{ii)}\quad \Lambda \leq 0.2\, \delta_T$$

$$\text{iii)}\quad \Lambda \leq 0.5\, q \left[\frac{T_o}{g\ \partial\theta/\partial z} \right]^{1/2} \qquad (25)$$

is quite satisfactory for the planetary boundary layer problem.

The scale variation with height for the neutral planetary boundary layer is shown in fig. 1 using both eqs. (24) and (25). The upper value was given whatever small value permitted a smooth tail to the curve, rather than a fixed boundary value for this flow.

In summary, eq. (24) appears to provide a reasonable estimate of the macroscale for a number of different flow geometries; i.e., for homogeneous turbulence behind a grid; for flat plate boundary layer flow; for a free jet; for self-preserving drag wake; for a momentumless wake; and for the atmospheric boundary layer under both neutral and stable conditions. Thus we will tentatively use this equation, but may anticipate modifications as further flows are considered.

B. TRANSFORMATION TO STREAM FUNCTION COORDINATES TO PERMIT SPATIAL VARIATION IN ROUGHNESS

The planetary boundary layer program for ref. 1 set the mean vertical velocity, w, zero everywhere. As seen by eq. (2), this is appropriate as long as the other velocity components have no horizontal spatial variation. To permit spatial inhomogeneity, we may transform eqs. (1) and (4) to stream function coordinates without adding any further equations. This may be done by defining a stream function ψ such that

$$\frac{\partial \psi}{\partial z} = u, \quad \frac{\partial \psi}{\partial x} = -\, w \qquad (26)$$

so that eq. (2) is satisfied automatically as long as v is independent of y. Then the convective derivatives in eqs. (1) and (4) reduce to $u\partial/\partial x$ for steady flow and $\partial/\partial z = u\partial/\partial\psi$.

For steady flow, our transformed equations, as programmed in coordinates x and ψ, now may be written as

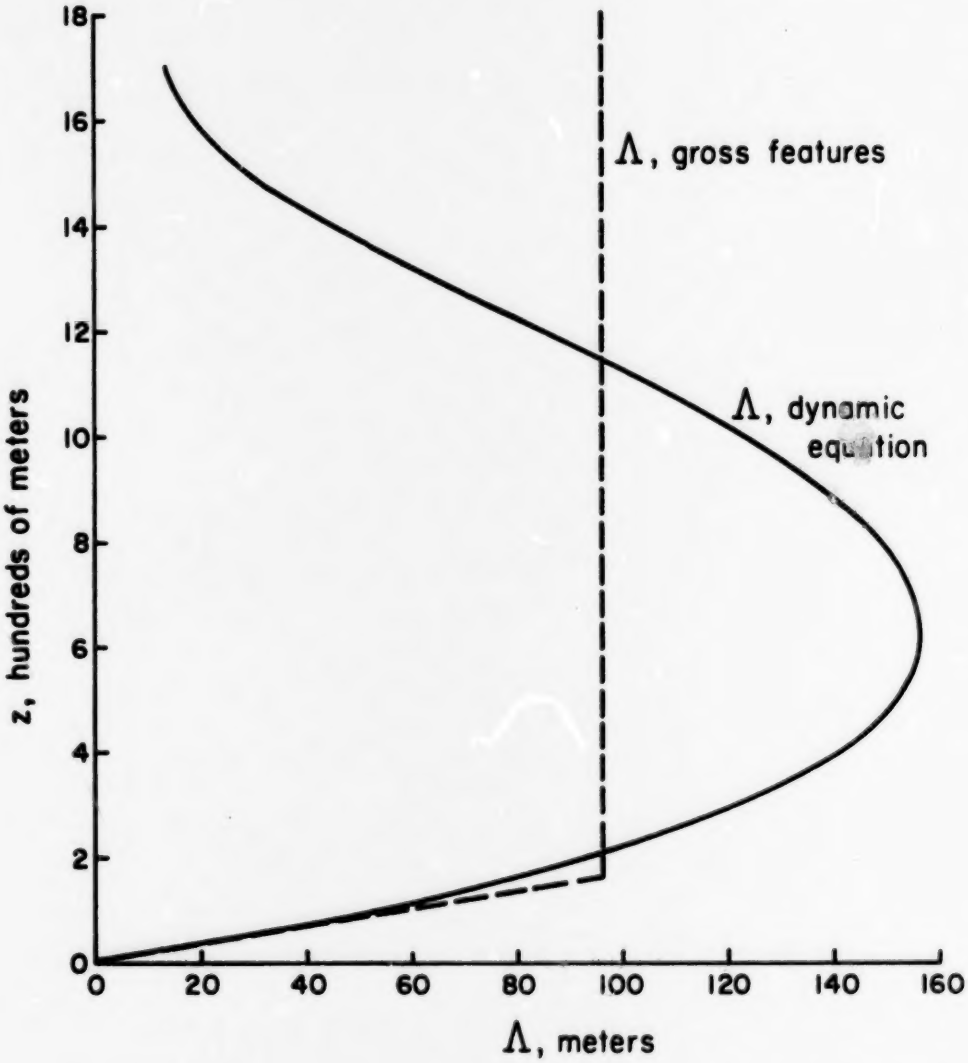

Figure 1: Macroscale variation with height for a neutral planetary boundary layer as given by the dynamic equation, eq. (24); and by the gross features of the flow, eq. (25).

$$\frac{\partial u}{\partial x} = \left(\frac{v - v_g}{u}\right) 2\Omega \sin \phi - \frac{\partial \overline{u'w'}}{\partial \psi} \tag{27}$$

$$\frac{\partial v}{\partial x} = \left(\frac{u_g}{u} - 1\right) 2\Omega \sin \phi - \frac{\partial \overline{v'w'}}{\partial \psi} \tag{28}$$

$$\frac{\partial \overline{u'u'}}{\partial x} = - 2\overline{u'w'} \frac{\partial u}{\partial \psi} + V_c \frac{\partial}{\partial \psi}\left(qu\Lambda \frac{\partial \overline{u'u'}}{\partial \psi}\right) - \frac{q}{u\Lambda}\left(\overline{u'u'} - \frac{q^2}{3}\right)$$

$$- \frac{2bq^3}{3u\Lambda} + \frac{4\Omega}{u}\left(\overline{u'v'} \sin \phi - \overline{u'w'} \cos \phi\right) \tag{29}$$

$$\frac{\partial \overline{v'v'}}{\partial x} = - 2\overline{v'w'} \frac{\partial v}{\partial \psi} + V_c \frac{\partial}{\partial \psi}\left(qu\Lambda \frac{\partial \overline{v'v'}}{\partial \psi}\right) - \frac{q}{u\Lambda}\left(\overline{v'v'} - \frac{q^2}{3}\right)$$

$$- \frac{2bq^3}{3u\Lambda} - \frac{4\Omega}{u} \overline{u'v'} \sin \phi \tag{30}$$

$$\frac{\partial \overline{w'w'}}{\partial x} = V_c \frac{\partial}{\partial \psi}\left(qu\Lambda \frac{\partial \overline{w'w'}}{\partial \psi}\right) - \frac{q}{u\Lambda}\left(\overline{w'w'} - \frac{q^2}{3}\right) - \frac{2bq^3}{3u\Lambda}$$

$$+ \frac{4\Omega}{u} \overline{u'w'} \cos \phi \tag{31}$$

$$\frac{\partial \overline{u'w'}}{\partial x} = - \overline{w'w'} \frac{\partial u}{\partial \psi} + V_c \frac{\partial}{\partial \psi}\left(qu\Lambda \frac{\partial \overline{u'w'}}{\partial \psi}\right) - \frac{q\overline{u'w'}}{u\Lambda}$$

$$+ \frac{2\Omega}{u}\left[\overline{v'w'} \sin \phi - \overline{w'w'} \cos \phi + \overline{u'u'} \cos \phi\right] \tag{32}$$

$$\frac{\partial \overline{v'w'}}{\partial x} = - \overline{w'w'} \frac{\partial v}{\partial \psi} + V_c \frac{\partial}{\partial \psi}\left(qu\Lambda \frac{\partial \overline{v'w'}}{\partial \psi}\right) - \frac{q}{u\Lambda} \overline{v'w'}$$

$$+ \frac{2\Omega}{u}\left[- \overline{u'w'} \sin \phi + \overline{u'v'} \cos \phi\right] \tag{33}$$

$$\frac{\partial \overline{u'v'}}{\partial x} = - \overline{v'w'} \frac{\partial u}{\partial \psi} - \overline{u'w'} \frac{\partial v}{\partial \psi} + V_c \frac{\partial}{\partial \psi} \left(q u \Lambda \frac{\partial \overline{u'v'}}{\partial \psi} \right) - \frac{q}{u \Lambda} \overline{u'v'}$$

$$+ \frac{2\Omega}{u} \left[\overline{v'v'} \sin \phi - \overline{v'w'} \cos \phi - \overline{u'u'} \sin \phi \right] \qquad (34)$$

In the equations given above, x and u are in the direction of the surface wind, with y and v normal to the surface wind.

The boundary conditions are that: at $\psi = \infty$, $u = u_g$, $v = v_g$, and all the turbulent correlations are equal to zero; and at $\psi = 0$, $u = v = q = 0$. In practice, the surface condition forces a large number of mesh points to be carried in the laminar sublayer. To avoid computations in this extremely thin region, the surface condition for most of our atmospheric computations is set above this layer in the constant flux region where

$$\left.\begin{aligned} \frac{\partial u}{\partial z} &= \frac{u}{z \, \ell n (z/z_o)} \\ v &= 0 \\ q^2 &= \frac{5.77 \, u^2}{(\ell n \, z/z_o)^2} \end{aligned}\right\} \qquad (35)$$

where the factor 5.77 is determined from the superequilibrium expressions valid in the constant flux region of the boundary layer[3].

All the computations made for flows with inhomogeneous surface roughness in this report are for neutral stability conditions. There appears to be no significant obstacle to extending these computations to either stable or unstable conditions.

C. QUASI-EQUILIBRIUM APPROXIMATION

Along with upgrading the capabilities of the model, we wish to investigate the possibility of simplifying the model in those circumstances where such simplification may be valid. Reference 1 considered a superequilibrium approximation which produced a very informative first-order-closure model with the Reynolds stresses all determined by mean flow gradients at a point. Herein we explore a quasi-equilibrium approximation intermediate between solving the full equations and solving the superequilibrium equations.

The simplified set of quasi-equilibrium (QE) equations may be obtained by neglecting the convective and diffusive terms in the second-order correlation equations (eqs. (4) - (6)) to form a set of algebraic relationships between the individual correlations and the mean flow derivatives, but retaining convection and diffusion of the turbulence by carrying the full equation for q^2. In this case, eqs. (4) through (11) are replaced by

$$\frac{Dq^2}{Dt} = -2\overline{u_i'u_j'}\frac{\partial u_i}{\partial x_j} + 2\frac{g_i}{T_o}\overline{u_i'\theta'} + V_c\frac{\partial}{\partial x_i}\left(q\Lambda\frac{\partial q^2}{\partial x_i}\right) - 2\nu\frac{q^2}{\lambda^2} \tag{36}$$

$$\overline{u_i'u_j'} = \delta_{ij}\frac{q^2}{3}[1 - 2(b - c)] - \frac{\Lambda}{q}\left[\overline{u_i'u_k'}\frac{\partial u_j}{\partial x_k} + \overline{u_j'u_k'}\frac{\partial u_i}{\partial x_k} - g_i\frac{\overline{u_j'\theta'}}{T_o} - g_j\frac{\overline{u_i'\theta'}}{T_o}\right] \tag{37}$$

$$\overline{u_i'\theta'} = -\frac{\Lambda}{A_1 q}\left(\overline{u_i'u_j'}\frac{\partial\theta}{\partial x_j} + \overline{u_j'\theta'}\frac{\partial u_i}{\partial x_j} - g_i\frac{\overline{\theta'^2}}{T_o}\right) \tag{38}$$

$$\overline{\theta'^2} = -\frac{\Lambda}{sbq}\overline{u_j'\theta'}\frac{\partial\theta}{\partial x_j} \tag{39}$$

Note that a new function s has been added to eq. (37) to allow eq. (36) to be added without making the system overdetermined. The term is added in such a way that the influence of the convective and diffusive terms in eq. (36) are distributed equally between the three components of q^2. We have also eliminated the Coriolis parameter in the Reynolds stress equations, based on the observation that $\Omega\Lambda/q \ll 1$ within the planetary boundary layer.

Figure 2 gives a comparison of the quasi-equilibrium results with that for the full set for a sample calculation of the equilibrium distributions in the planetary boundary layer (PBL). The figure shows that the approximate model gives nearly the same result as the full set for this steady flow. Results for a tougher test involving the dynamic response of the PBL to a change with time of the surface condition are given in fig. 3. The equilibrium distributions obtained

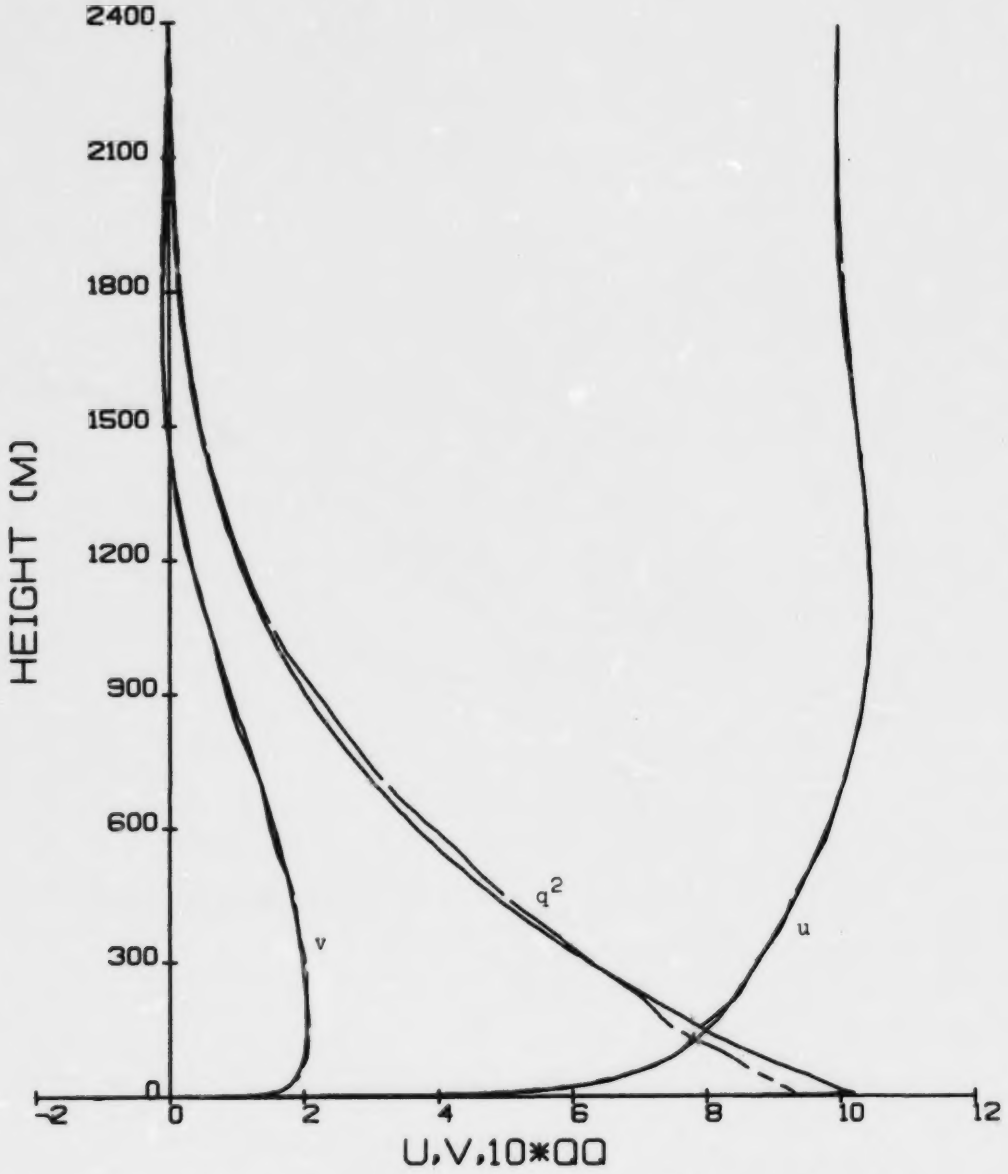

Figure 2: Velocity distributions in the neutral planetary boundary layer (z_o = .0774 m, f = 10^{-4} sec^{-1}, u_g = 10 m/sec) computed from the quasi-equilibrium approximation (—) and from the full set (— —).

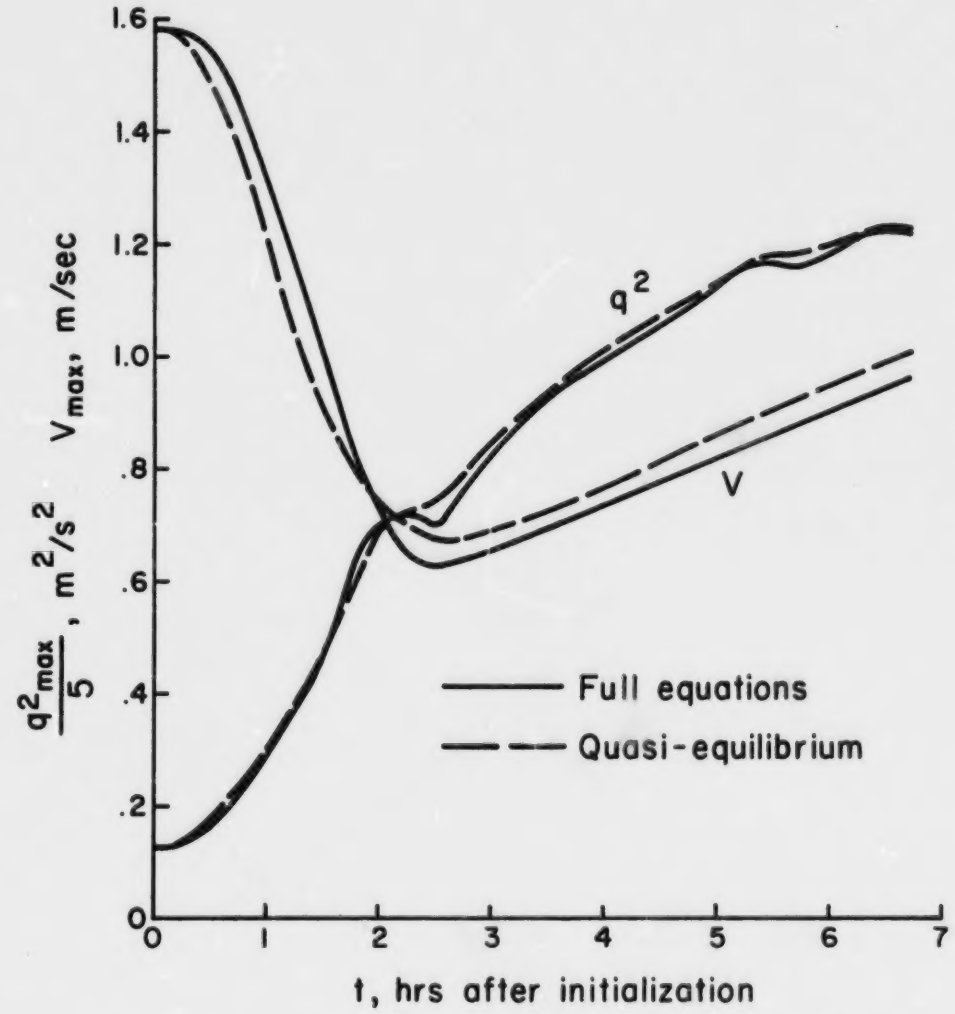

Figure 3: Dynamic response of variables within the planetary boundary layer to an increase in the surface heat flux as predicted by the full equations, and by the quasi-equilibrium set.

by the full equations (as shown in fig. 2) are taken as initial conditions but surface heat flux is varied with time as given later in eq. (53). Figure 3 shows the response of the maximum normal velocity v and the maximum q^2 as a function of time for 8 hours beginning at sunrise. Maximum deviation between the two solutions is 10% during this part of the day when turbulence is undergoing its most rapid changes. Although the quasi-equilibrium solution has some problems in tracking the turbulence, the overall agreement is acceptable.

Comparisons of the two methods have also been made in calculations of an axisymmetric, momentumless wake[12] which show approximately a 10% difference in the resulting distributions. The great simplification made possible by the QE approximation appears to be ample justification for accepting the slight loss in accuracy exhibited in these comparisons. Encouraged by these results, we applied the QE approximation to a calculation of the diurnal variation in the PBL (see Section VI), a calculation which would require excessive time on our small computer with the full set of equations.

SECTION V

MODIFICATIONS TO THE POLLUTANT DISPERSAL MODEL

A. INCLUSION OF THE CAPABILITY TO COMPUTE MEANDER

A.1 Background

The diffusion of a pollutant plume released into a turbulent field strongly depends on the scale length of the plume as well as the scale of the turbulence. In the A.R.A.P. invariant model, turbulent diffusion is proportional to the product of the plume scale and the root mean square of the turbulent kinetic energy in the plume. Much of the work described below deals with improving the computational techniques for both the scale and energy during the early stages of plume growth before the plume scale has spread to the scale of the turbulence.

The impetus for this study is the frequent experimental observation that pollutant diffusion during the first few minutes after release is primarily caused by the large-scale meandering of the center of the plume. This is most evident when relatively small plumes are released into unstable (i.e., large-scale) turbulence. The A.R.A.P. model is capable of predicting this meander contribution provided (1) the plume scale is properly computed and (2) the energy associated with the scale of the plume is considered separately from the energy contained in the larger turbulent eddies.

In Section IV A., the development of a dynamic equation for the scale of the turbulence and the average energy contained in this turbulence was described. In this section a parallel effort for the plume scale is described. It should be recognized that an explicit dynamic equation for the plume scale similar to that for the turbulence scale is not possible at this time. The available data are simply inadequate for such a task. However, it should also be recognized that even the smallest plume scales of practical interest are still large enough to be in the inertial subrange of the energy spectrum. In this range it has been experimentally established that the energy dissipation is nearly constant in the energy cascade from large to small

eddies. It is this property of the energy spectrum that provides the relation between the plume-scale energy and the turbulence-scale energy.

This property is developed quantitatively in Section V, A.2. The set of partial differential equations must, of course, be solved numerically. Fortunately, two extreme cases can be postulated for which exact analytical solutions exist. These solutions, with emphasis on estimates of numerical accuracy, are described in A.3. A.4 describes the sensitivity of various model parameters using a one-dimensional (vertical) diffusion program. This program requires less than 5% of the time required by the larger two-dimensional program and, therefore, is more convenient for sensitivity analysis. Two typical cases of plume diffusion using the large two-dimensional program for extreme stability conditions of the atmospheric boundary layer are illustrated in Section VI.

A.2 Diffusion Model

For ease of explanation, we will consider the one-dimensional diffusion of a passive pollutant plume. The invariant model of turbulence yields the following set of equations for the mean concentration $\bar{C}$, average vertical flux $\overline{C'w'}$, average temperature correlation $\overline{w'\theta'}$, and the concentration correlation $\overline{C'\theta'}$.

$$\frac{\partial \bar{C}}{\partial t} = - \frac{\partial}{\partial z} \overline{C'w'} \tag{40}$$

$$\frac{\partial \overline{C'w'}}{\partial t} = - \overline{w'w'} \frac{\partial \bar{C}}{\partial z} + V_c \frac{\partial}{\partial z} \left(\Lambda_p q_p \frac{\partial}{\partial z} \overline{C'w'} \right) - \frac{q_p A_1}{\Lambda_p} \overline{C'w'} + \frac{g}{T_o} \overline{C'\theta'} \tag{41}$$

$$\frac{\partial \overline{C'\theta'}}{\partial t} = - \overline{w'\theta'} \frac{\partial \bar{C}}{\partial z} - \overline{C'w'} \frac{\partial \bar{\theta}}{\partial z} + V_c \frac{\partial}{\partial z} \left(\Lambda_p q_p \frac{\partial}{\partial z} \overline{C'\theta'} \right) - \frac{2bsq_p}{\Lambda_p} \overline{C'\theta'} \tag{42}$$

$$\frac{\partial \overline{c'c'}}{\partial t} = -2\overline{c'w'}\frac{\partial c}{\partial z} + V_c \frac{\partial}{\partial z}\left(\Lambda_p q_p \frac{\partial \overline{c'c'}}{\partial z}\right) - \frac{2bq_p s}{\Lambda_p}\overline{c'c'} \qquad (43)$$

In eqs. (40) - (43) we assume that the Reynolds number is high enough so that viscous diffusion terms may be neglected compared to the turbulent diffusion terms. The development of these equations is described in ref. 1 for the interested reader.

The values for the various model parameters are, as explained in Section IV, $V_c = 0.3$, $A_1 = 0.75$, $s = 1.8$, and $b = 0.125$. The coefficients A_1 and s have been retained from the analogous terms in the $\overline{u'\theta'}$ and $\overline{\theta'\theta'}$ equations, eqs. (5) and (6). This assumes that the turbulent Schmidt number is equal to the turbulent Prandtl number under neutral stability conditions, and that the spectra of concentration fluctuations is similar to that of temperature fluctuation spectra.

Because the plume is passive, the turbulence field may be decoupled from this set of equations. Hence, the quantities $\overline{w'w'}(z)$ and $\overline{w'\theta'}(z)$ which appear in the production terms of eqs. (41) and (42) may be considered known functions of z, as is the potential temperature lapse rate $\partial\theta/\partial z$.

The plume scale Λ_p is perhaps the most difficult term to model in the equations because of the paucity of useful experimental data. At present, the plume scale is computed from the equation

$$\Lambda_p = \ell\sigma_z \qquad (44)$$

where σ_z is the standard deviation of the mean concentration distribution and $\ell = 0.5$, and is subject to the following constraint:

$$\Lambda_p \leq \Lambda_t \qquad (45)$$

The constraint simply states that the mixing scale cannot be larger than the largest turbulent eddy. The proportionality factor ℓ is a model input and can be adjusted as better data become available. The sensitivity to this parameter will be described later.

The major improvement to the model during the present study is the computation of the energy term q_p which appears in these equations. Previously, q_p was defined as the square root of twice the average kinetic energy contained in the major turbulent eddies with a scale length Λ_t. This definition, however, is inconsistent with the experimental observation of the distribution of energy contained in the spectrum of eddy sizes. As long as the plume scale is the same order as the turbulence scale, this definition is appropriate. Such is the case, for example, when relatively large plumes are released into stable environments. However, when small plumes ($\Lambda_p \sim 1$ m) are released into unstable environments ($\Lambda_t > 100$ m), this definition assigns too much turbulent energy to the plume. The diffusion terms become the dominant terms in the equations and this, in turn, does not permit the meander contribution to plume diffusion.

The turbulent energy distribution function shows that small-scale eddies have much less energy than large-scale eddies. Even more important, though, is the observation that in the inertial subrange the rate of energy dissipation is constant from large to small eddies, as postulated by Kolmogorov[13]. In the invariant model, energy dissipation, ϵ, is modeled as

$$\epsilon = \frac{q^3}{\Lambda} \qquad (46)$$

Therefore, if ϵ is constant, then

$$q_t = q_{t_0}\left(\frac{\Lambda_t}{\Lambda_{t_0}}\right)^{\frac{1}{3}} \qquad (47)$$

where q_{t_0} is the average energy in the turbulent eddy whose scale is Λ_{t_0}. Equation (47) thus becomes a reasonable estimate to use for q_p in eqs. (41) - (43).

A.3 Exact Solutions of Diffusion Equations

For convenience, we will consider only neutral conditions. This assumption greatly simplifies the solution of eqs. (40) - (43) because the last term in eq. (41) and all of eq. (42) may be dropped. We will consider the lower limit of $q_p \rightarrow 0$ first, recalling that this limit nearly approximates the case of small plumes embedded in large-scale turbulence.

In the limit $q_p \to 0$, eq. (41) reduces to

$$\frac{\partial \overline{c'w'}}{\partial t} = - \overline{w'w'} \frac{\partial c}{\partial z} \tag{48}$$

Equations (40) and (48) can be used to eliminate $\overline{c'w'}$ to yield

$$\frac{\partial^2 c}{\partial t^2} - \overline{w'w'} \frac{\partial^2 c}{\partial z^2} = 0 \tag{49}$$

Equation (49) is the classical wave equation in one space dimension. Its solution is two plane waves traveling in the positive and negative z directions without change of form and with a velocity of $(\overline{w'w'})^{1/2}$. Thus, the early stages of plume diffusion (in which $\Lambda_p \ll \Lambda_t$) may be termed the wave-dominated region.

If we now consider the opposite limit in which the plume scale is constant and equal to the turbulence scale, and assume that the turbulence is isotropic (i.e., $\overline{w'w'} = q^2/3$) and, further, that $A_1 = 1.0$ and $V_0 = 1/3$ (rather than 0.75 and 0.3), then it may be shown that eqs. (40) and (41) have the rather simple solution

$$c = c_1 \sqrt{\frac{x_1}{x}} \exp\left(-\frac{z^2}{2\sigma^2}\right) \tag{50}$$

where

$$\sigma^2 = \frac{2}{3} \frac{x}{U} q \Lambda \tag{51}$$

This, of course, is the familiar Gaussian distribution function. The region in which $\Lambda_p = \Lambda_t$ may, therefore, be termed the diffusion-dominated region.

Thus, a qualitative picture of plume diffusion is evident. Plume motion is initially wave-like in character as the plume meanders about the large eddy. As the plume diffuses and spreads, the wave motion is damped and the plume becomes completely dominated by diffusion. The two exact solutions described above provide convenient test cases with which to examine the accuracy of our numerical technique.

A.4 Accuracy of Computations

The accuracy of the numerical technique used to compute the wave-dominated portion of the plume history was investigated by considering a plume with an initial Gaussian distribution defined by a standard deviation of 1 m and a normalized centerline concentration of 1.0 released into an isotropic turbulence field with $\overline{w'w'} = 1\ m^2/sec^2$. The $q_p \to 0$ limit was achieved by setting identically to 0 the diffusion and tendency-to-isotropy terms in eq. (41). As was noted above, the analytic solution shows that the plume splits into two identical waves, each having a maximum concentration of 0.5 and traveling away from the center of the plume with a velocity of 1 m/sec.

Figure 4 shows the computed distribution in the half plane 100 m downwind of plume release. The numerical technique was a fully-implicit tridiagonal algorithm[14] with a time step permitting a maximum local concentration change of 3%. For comparative purposes the exact solution is also shown. The wave speed is accurate to within about 3% but the maximum concentration is accurate to only 20%. The small oscillations which appear in the numerical solution near the center of the plume are due to the finite (5%) noise tolerances used in the calculation.

The sensitivity of the error in maximum concentration to both the maximum time step and the numerical technique itself was investigated. In the fully-implicit technique the error is a nearly linear function of the step size, so that small steps are required to maintain even 20% accuracy for 100 m. There are two factors, however, which prohibit step changes smaller than 1%. The first is the obvious cost in computer time - a cost which is prohibitive for the large two-dimensional diffusion program. The second factor is that the smaller step size requires more steps and, therefore, accumulates larger round-off error to reach a certain distance downstream.

Numerical accuracy in the large A_p limit was investigated using a larger plume (σ = 25 m) in an isotropic turbulence field. The plume scale was held constant at 100 m and the model parameters A_1 and V_c were adjusted to 1.0 and 1/3, respectively, in order to coincide with the exact solution given by eqs. (50) and (51). Figures 5 and 6 show the computed and exact concentration profiles at distances

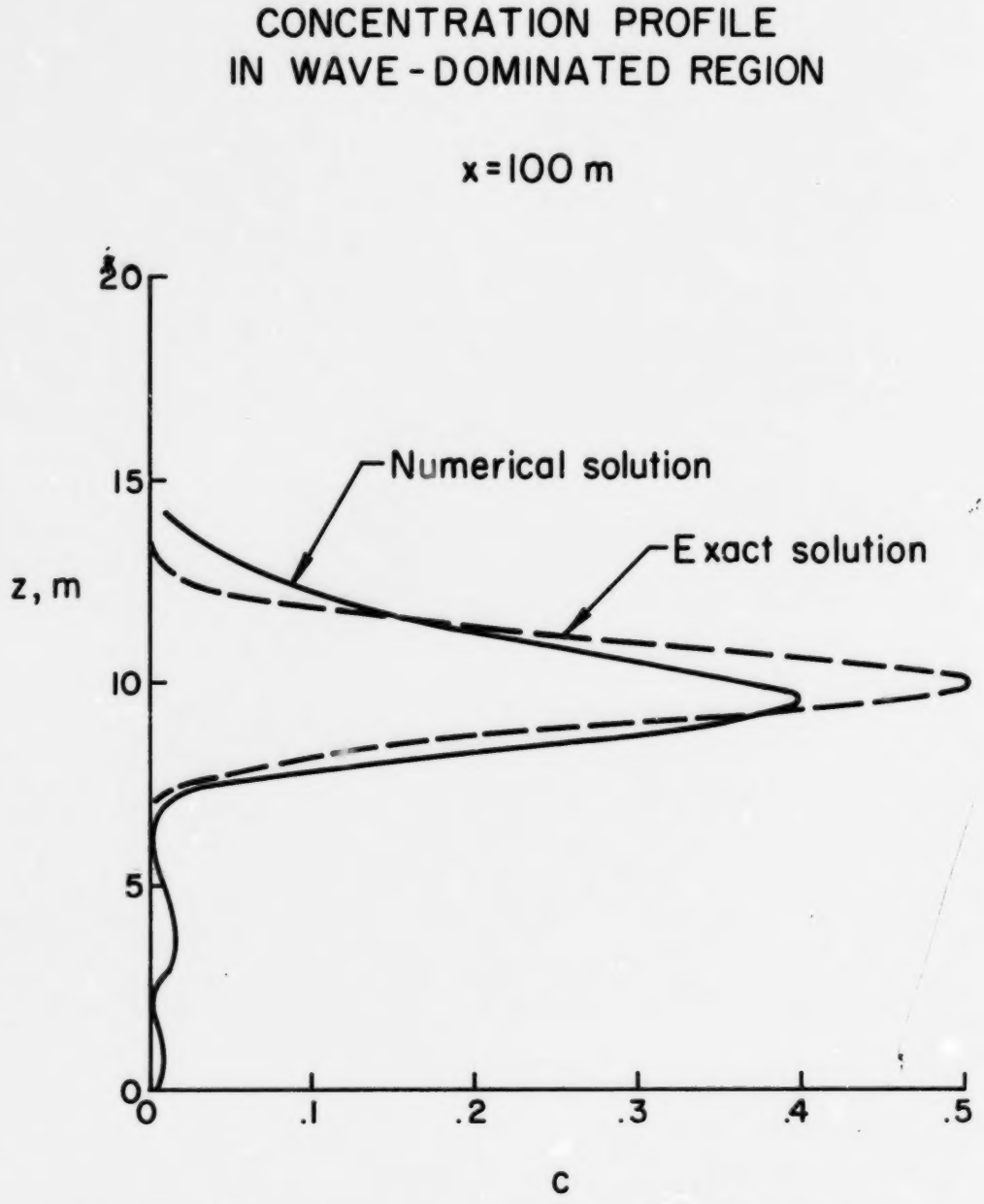

Figure 4: Comparison of numerical and analytical predictions for one-dimensional wave propagation.

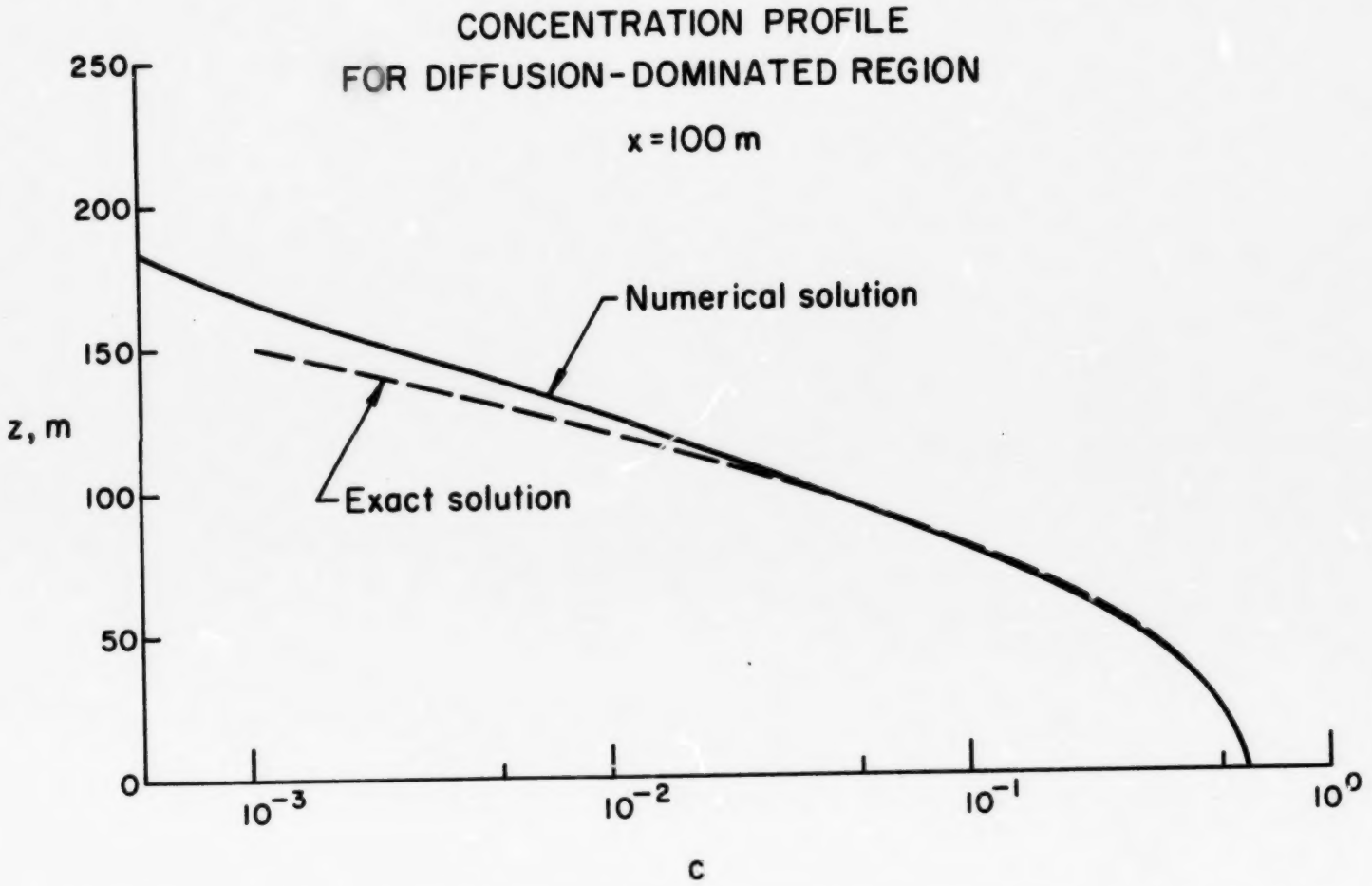

Figure 5: Comparison of numerical and analytical predictions for one-dimensional diffusion.

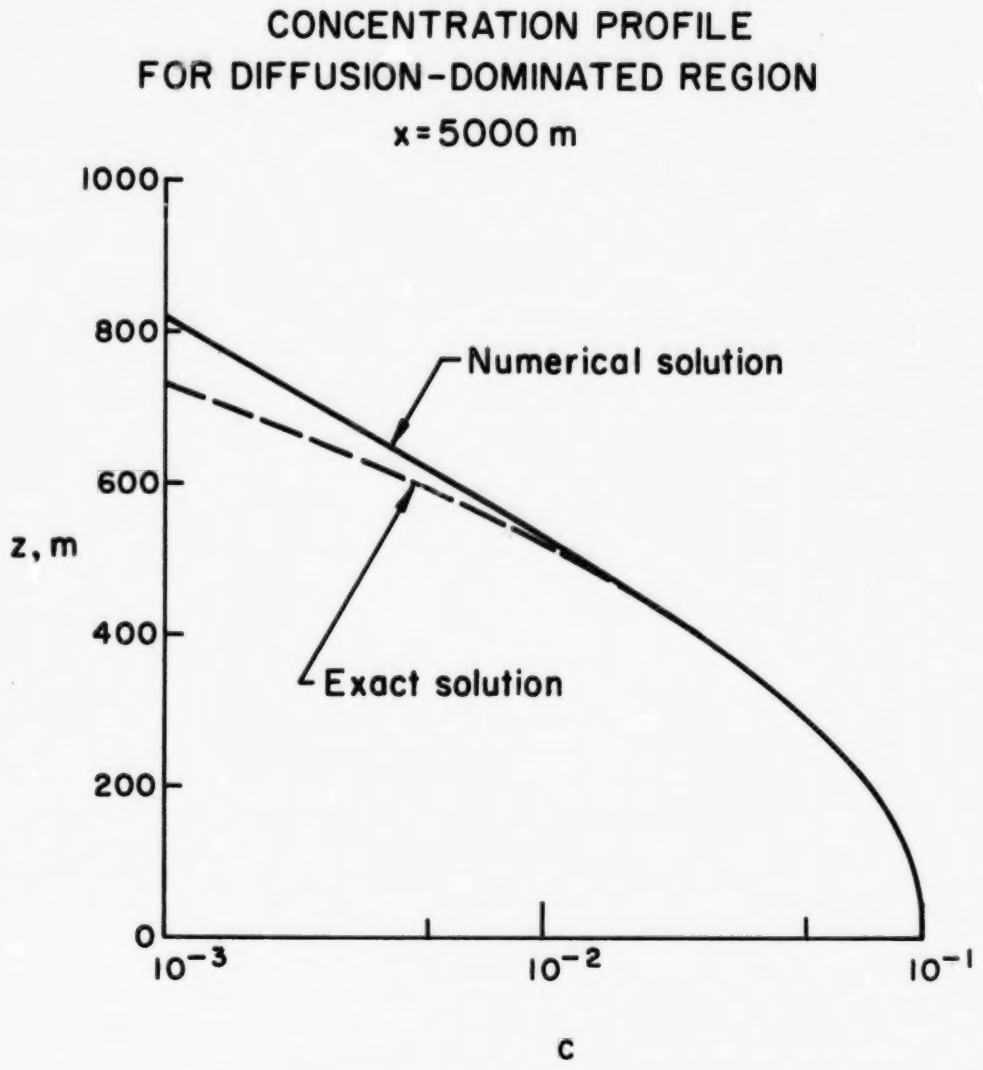

Figure 6: Comparison of numerical and analytical predictions for one-dimensional diffusion far downstream of the release point.

of 100 m and 5000 m. Although the exact values are difficult to read because of the log scale, the centerline concentration is within 5% of the exact value out to 5 km. Even at this large distance, the location at which the concentration is within 1% of its maximum value is accurate to about 10%. These computations were made with a maximum step change of 5% rather than 3%.

Based on these results, we conclude that a step size of about 5% using the fully-implicit tridiagonal technique is adequate to insure 5% accuracy in centerline dilution for a diffusion-dominated plume. This combination leads to larger errors during the early wave-dominated region, but since the extent of this region is a small portion of the plume lifetime, it is considered to be an acceptable price to pay for realistic computation time and numerical stability.

A.5 Model Sensitivity

The numerical technique described above was used to compute the one-dimensional diffusion of a pollutant plume. Our objective was to establish the sensitivity of the model to various input parameters prior to exercising the more time-consuming two-dimensional model. The primary parameters investigated were the plume scale and the initial conditions.

The conditions used for these computations were a pollutant plume with an initial Gaussian distribution defined by a centerline concentration of 1 and a standard deviation of 1 m. The turbulence field was neutral and isotropic with a turbulence intensity $\overline{w'w'}$ of 1 m^2/sec^2. The plume scale was computed using

$$\Lambda_p = \beta(z_T - z_B) \qquad (52)$$

where β is a model input and z_T and z_B are the extreme locations where the mean concentration is 25% of the maximum value. This equation differs from eq. (44) and has been found to be a poorer model for the plume scale in the wave-dominated region. However, for the purposes of demonstrating the sensitivity of the diffusion model to the plume scale, eq. (52) is adequate. For a Gaussian distribution, eqs. (44) and (52) are related by $\ell/\beta \sim 3.3$.

Figure 7 shows the growth of the plume as a function of distance downwind, with β as a parameter. The maximum scale length (60 m) corresponds to the largest turbulent eddy which can exist 100 m above the ground according to eq. (45). The rate of growth of the plume is relatively insensitive to β.

However, the shape of the plume is highly sensitive to β, especially during the first 100 meters. Figure 8 shows the ratio of centerline to maximum concentration as a function of distance and β. This ratio is a measure of the splitting of the plume. It is evident that if the scale is too large, ($\beta \rightarrow 1$) then there is little, if any, splitting of the plume. For the larger scale lengths, the diffusion term in eq. (41) is dominant and a wave cannot be formed. Perhaps more significant, from a computation standpoint, is the extent of the wave-dominated region. For those cases in which a strong wave occurs, ($\beta \rightarrow 0$) the wave region spans approximately 100 m. Beyond this point, the diffusion terms are filling in the profile and the maximum concentration returns to the center of the plume. The rate of the filling-in process depends on the balance between the diffusion and isotropy terms in eq. (41).

Reproduced from best available copy.

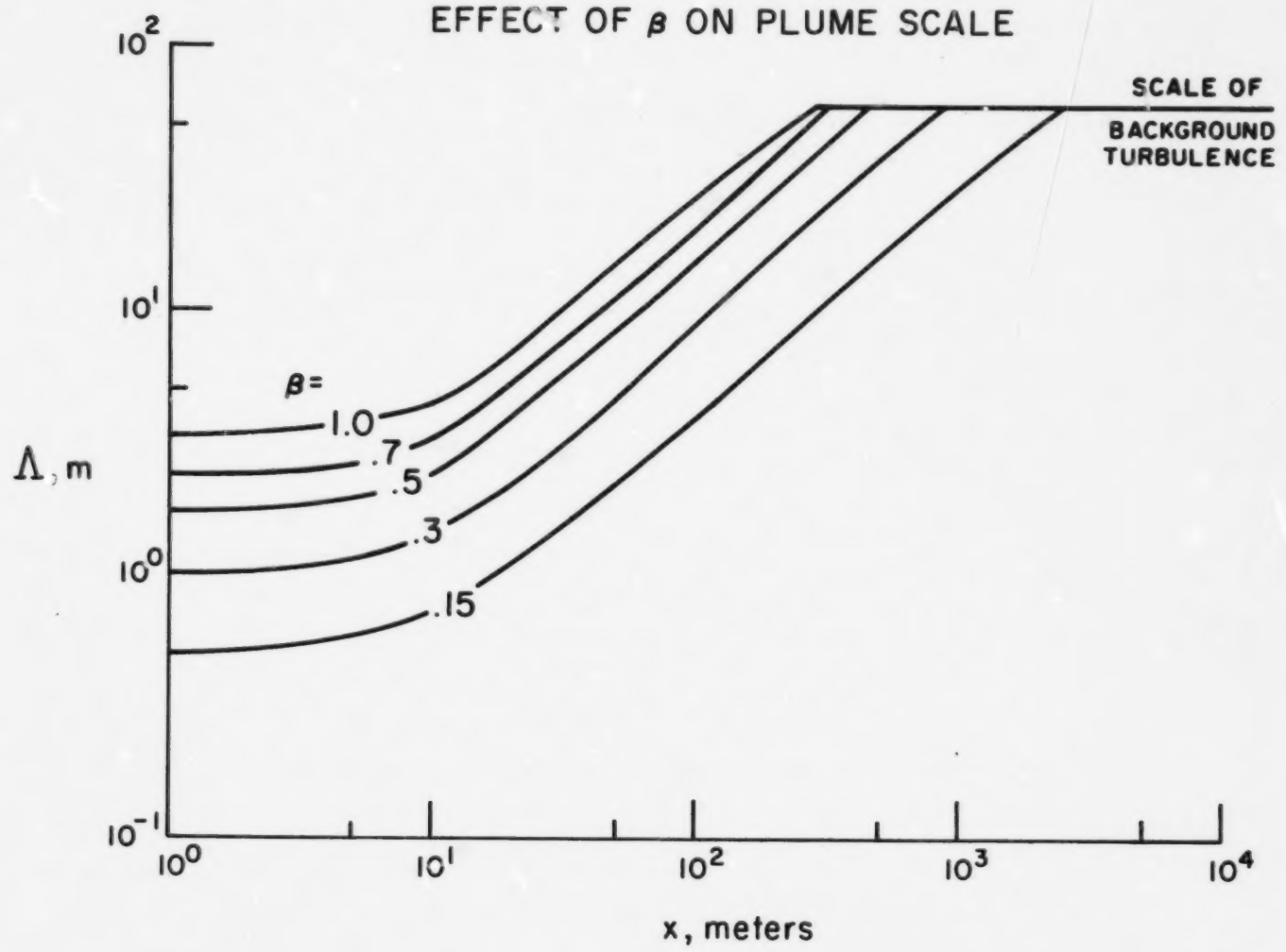

Figure 7: Plume scale as a function of the proportionality constant in eq. (52).

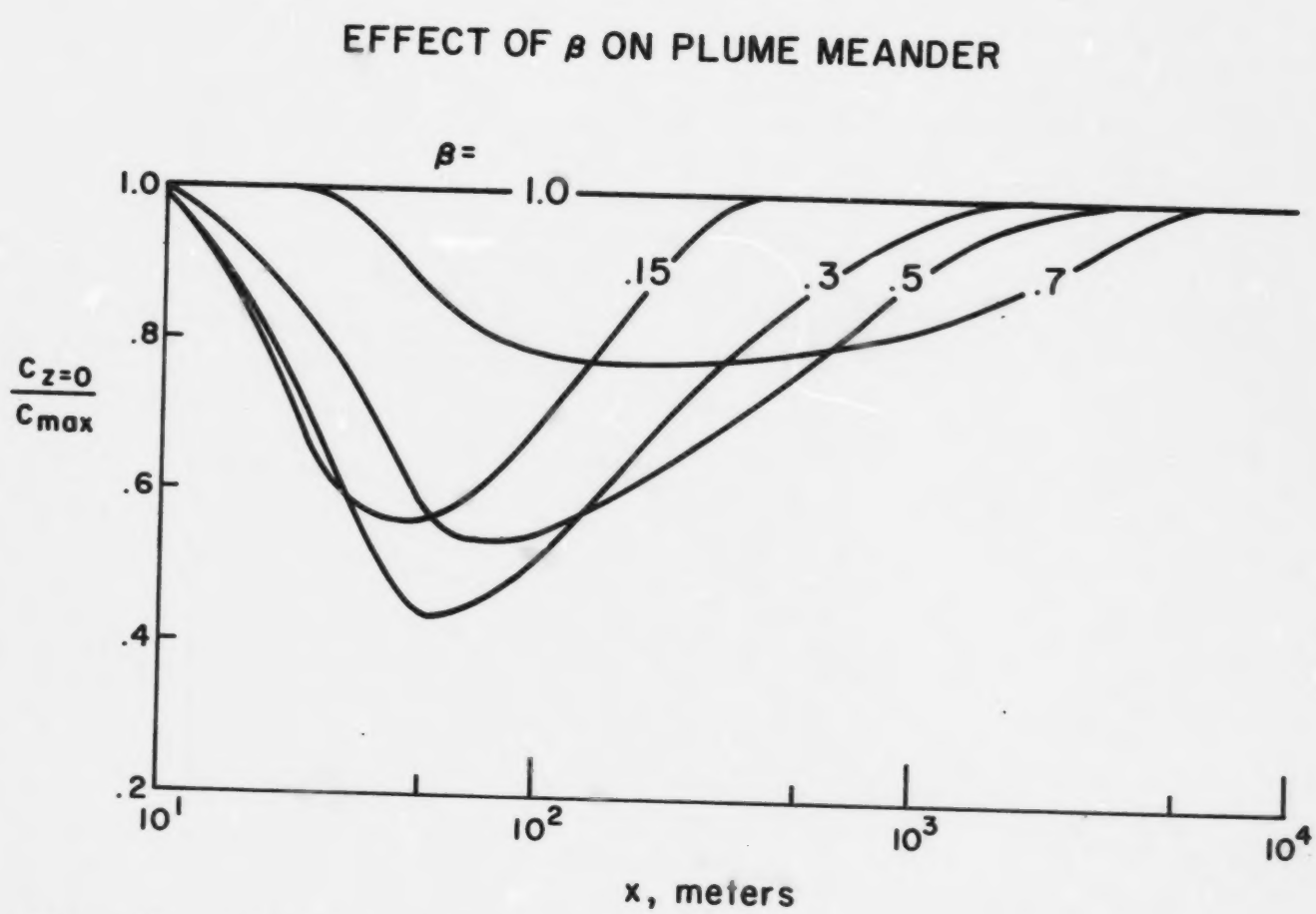

Figure 8: Centerline plume concentration normalized by the local maximum concentration plotted as a function of distance from the release point for various values of the scale factor β.

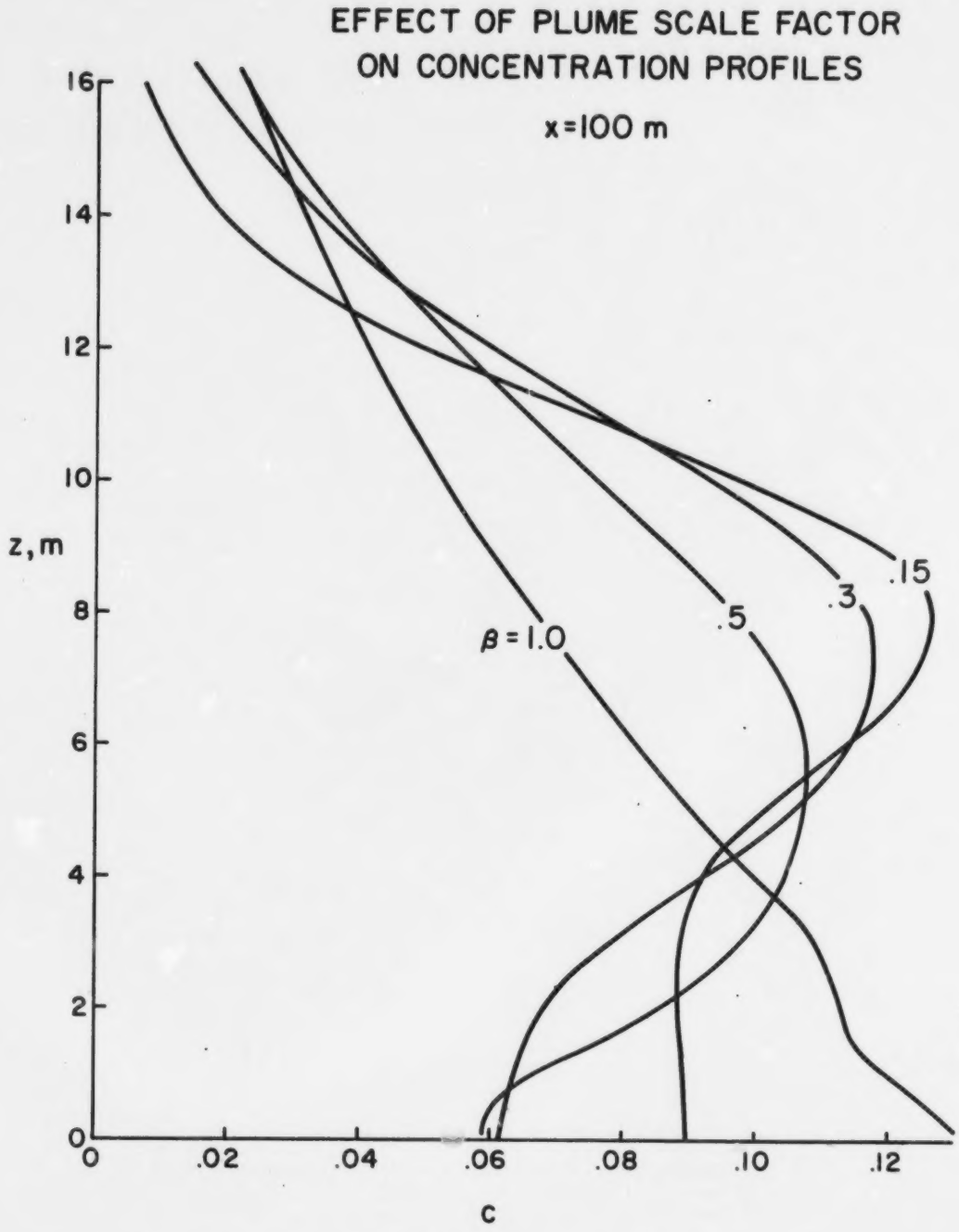

Figure 9: Mean concentration profiles 100 m downstream of a Gaussian plume release for different values of scale factor β. (u = 10 m/sec, $\overline{w'w'}$ = 1 m^2/sec^2, q^2 = 3 m^2/sec^2, neutral stability, σ_i = 1 m, C_{max_1} = 1).

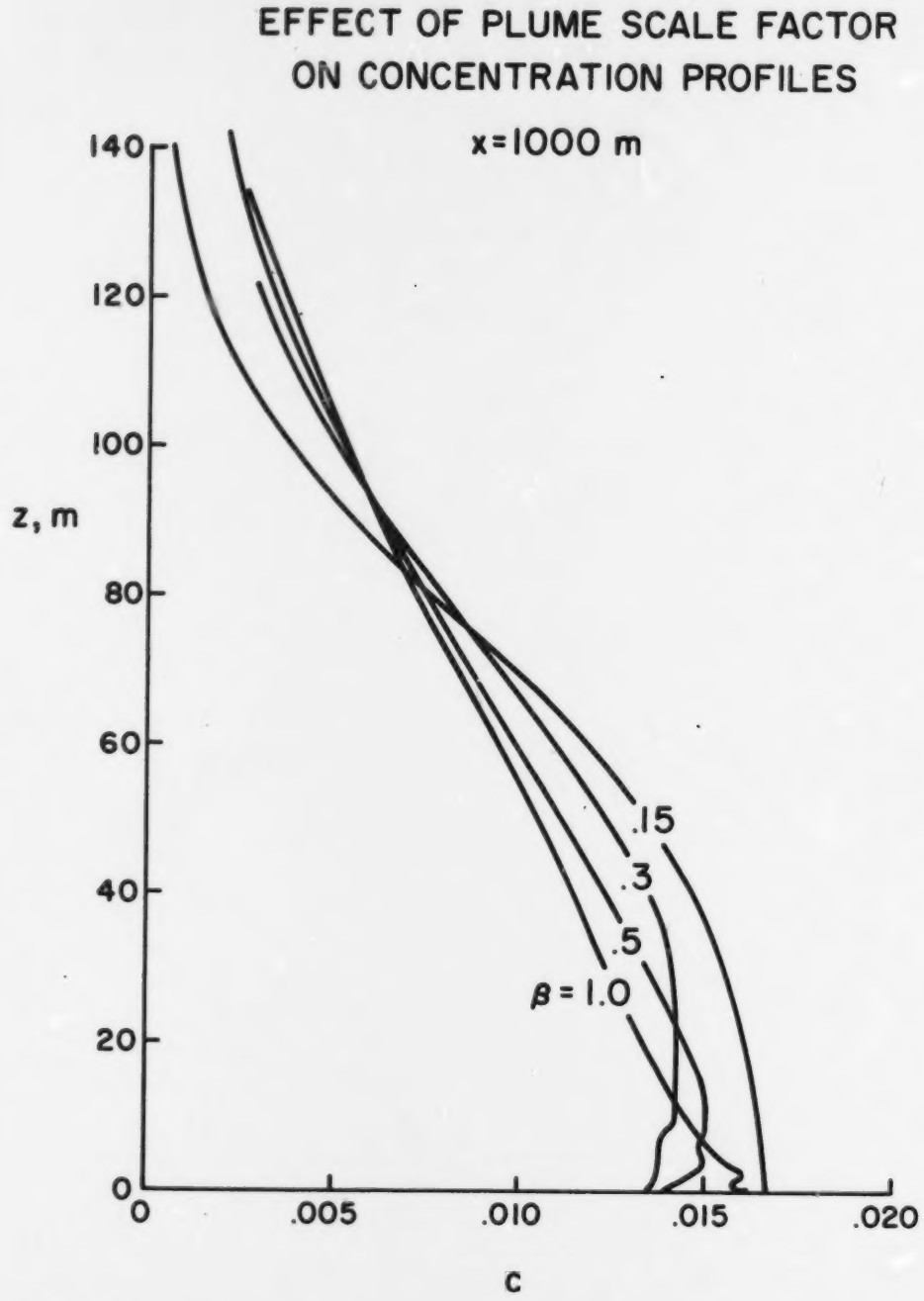

Figure 10: Mean concentration profiles at 1 km for the same conditions as fig. 9.

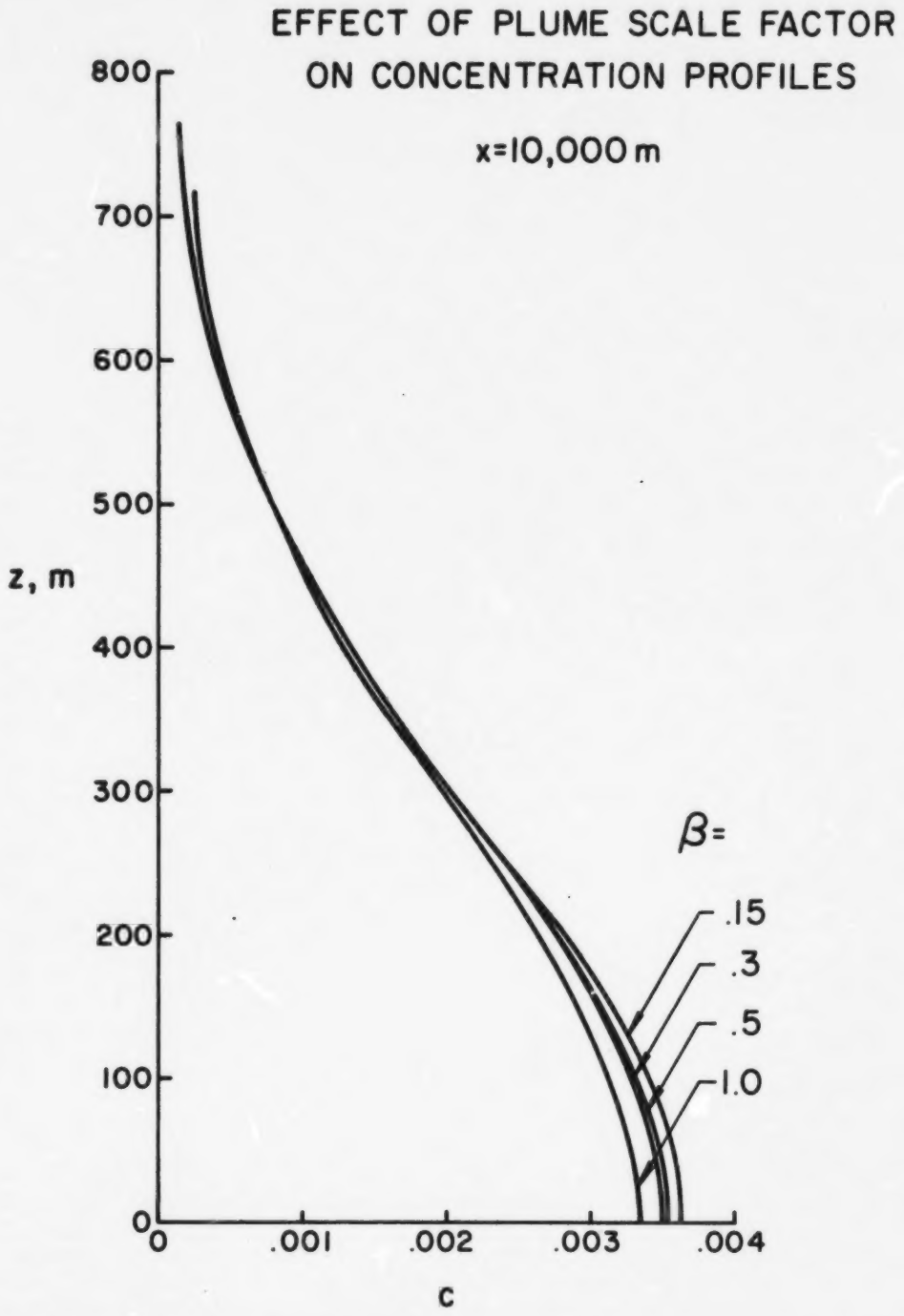

Figure 11: Mean concentration profiles at 10 km for the same conditions as fig. 9.

The amount of plume meander is also dependent on the initial condition one chooses for the plume. If one considers a finite-size plume as the initial condition, then it is reasonable to assume that there is no initial correlation between the turbulence and the pollutant i.e., $\overline{C'w'}(t=0) = 0$. This was the condition used for all the cases which were described above. If, however, one chooses a point source as the initial condition, then by the time the computation has begun (in this case when $\sigma = 1$ m), there is sufficient time for the $\overline{C'w'}$ correlation to develop. Figure 12 illustrates the differences in the initial meandering of the plume due to the initial conditions on $\overline{C'w'}$. It is evident that there is considerably more meander downstream of the point source. However, beyond x = 100 m the two computations are virtually identical.

B. COUPLING TO A TWO-DIMENSIONAL SPATIAL VARIATION OF THE TURBULENCE

Eventually we would like to combine the PBL turbulence model and the pollutant dispersal model to permit the pollutant dispersal to be fully coupled to variations in the background turbulence in either time or space, as well as to permit the internally generated plume turbulence to affect the PBL turbulence model. In the interim, we have been utilizing the PBL turbulence model and the pollutant dispersal models as separate programs with the output of the turbulence model used as input to the dispersal model. With the incorporation into the turbulence model of the capability to compute spatial variations in both x, the geostrophic wind direction, and z, the height (by using the stream function approach discussed earlier), it became possible to incorporate this as input to the turbulence file used for point source dispersal calculations. Output from the PBL program is stored as a function of z at a number of different x positions, with the values used in the dispersal computations obtained by interpolating between the values existing in this input file.

It should be noted that a slight inconsistency still remains in our treatment of three-dimensional plume dispersal. The wind direction x is assumed to be constant with respect to z, while the output of PBL clearly shows a change in wind direction with height. This introduces little error for unstable atmospheric conditions when the turning rate with altitude is quite small, but can be significant for stable conditions when a wind shift of 30 to 40 degrees may occur

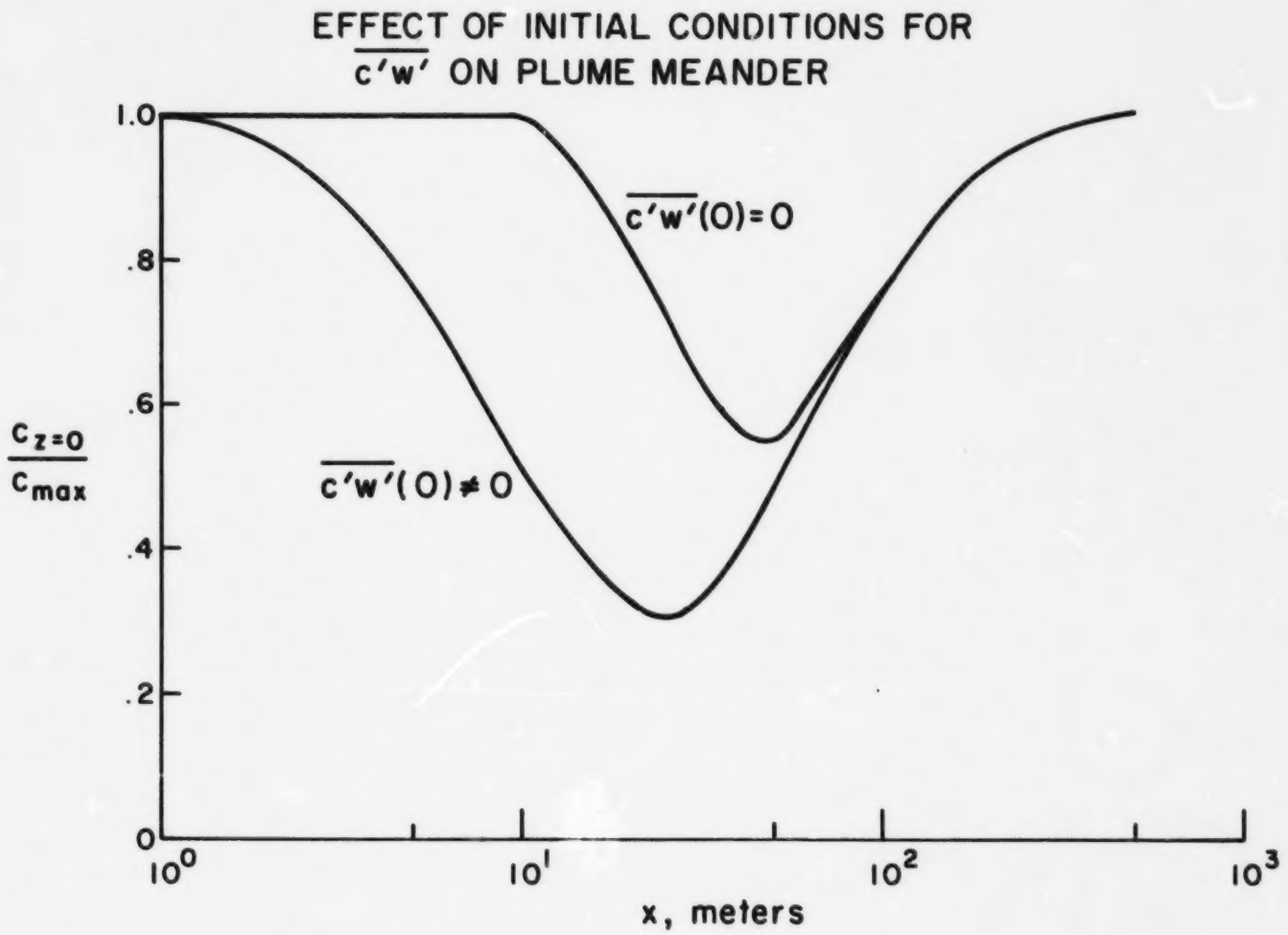

Figure 12: Influence of initial values of $\overline{c'w'}$ on subsequent distortion of the concentration profiles.

within a few hundred meters height variation. There is no fundamental difficulty in including this effect in the program since we are computing variations in y and z as a function of x, but it does require the computation of the plume in the full (y, z) plane since this will destroy the symmetry of the plume in the y direction. This would require a doubling of computer time.

SECTION VI

SAMPLE CALCULATIONS AND MODEL VERIFICATION

The computer model is now capable of making a wide range of calculations of practical interest. The following examples have been chosen for demonstrating its capabilities and for their own inherent interest.

A. STEADY STATE, NEUTRAL, PLANETARY BOUNDARY LAYER

The mean wind and Reynolds stress components existing in the steady state, neutral planetary boundary layer have been computed and reported on in ref. 11 which is included in this report as the Appendix. The macroscale used in those computations was determined by one of the bounds given in eq. (25). The results were compared (in fig. A3) with the wind and turbulence profiles computed by Deardorff[15] using his three-dimensional, unsteady calculations. Our calculation has been repeated using the dynamic scale equation given in eq. (24). These results are also compared with Deardorff's results (appropriately unnormalized) in fig. 13. There is relatively little difference between the results for the determination of u, v, and q using the two approaches to the determination of the scale. In either case, the wind profiles agree reasonably well with Deardorff's but the turbulence is significantly lower. Part of the discrepancy is probably caused by the low altitude at which Deardorff matches with the geostrophic wind, but it may also indicate that our predictions for the horizontal wind variance perpendicular to the surface wind are low. This component is difficult to determine empirically. Measurements as reported by Panofsky[16] contain an uncertainty of a factor of 2 in what this component should be. For the present, however, we will accept this discrepancy and use these resulting equilibrium profiles as a starting point for a more interesting result - the dynamic response of the earth's boundary layer to changing surface heat flux.

B. DIURNAL VARIATIONS IN THE PLANETARY BOUNDARY LAYER

In the Appendix we discuss the detailed calculation of the response of the planetary boundary layer to the changing diurnal conditions embodied in the rising and setting of the

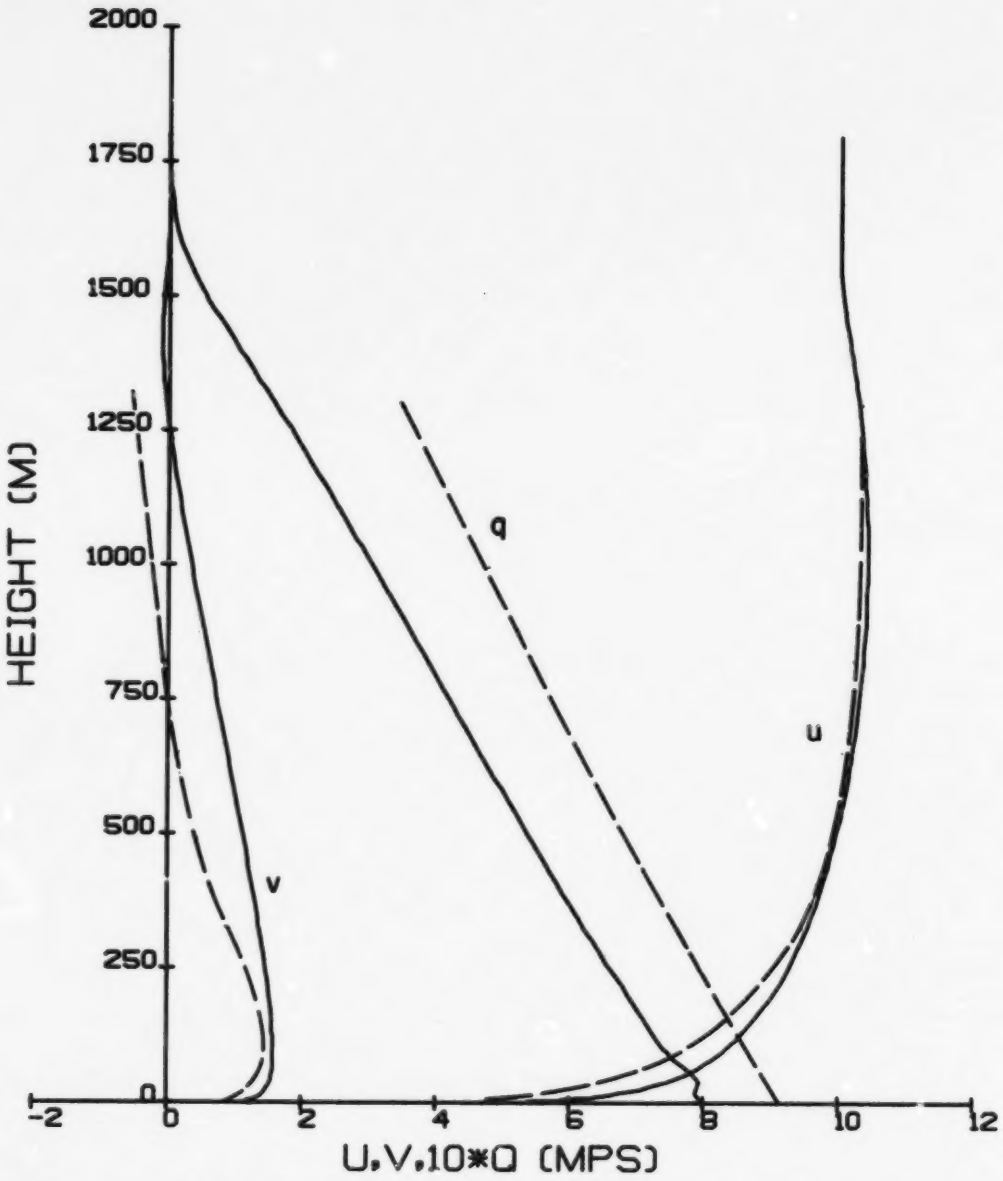

Figure 13: Comparison of velocity distributions in the neutral planetary boundary layer (z_o = 0.008 m, $f = 10^{-4}$ sec^{-1}, u_g = 10 m/sec) as predicted by the model with dynamic scale equation with Deardorff's model predictions (---)(ref. 15).

sun. The present discussion will briefly summarize the input conditions for this calculation and highlight the results. A further calculation made with the scale equation in its dynamic operation will also be touched upon.

For the actual calculation of the diurnal variation of the planetary boundary layer, we program and solve eqs. (1) - (11) subject to the quasi-equilibrium approximation. Geostrophic boundary conditions were applied at altitude while at the surface layer, conditions were matched with the results of the Monin-Obukhov similarity analysis. A temperature inversion lid was initially established at 2 km and permitted to drift up or down through the course of the three-day calculation as the computation deemed necessary. The initial profiles (with $\theta = 0$ everywhere below 2 km) are as given in fig. A3 and discussed in Section VI A. To simulate the effect of the sun, we set the surface heat flux variation as

$$(\overline{w'\theta'})_o = 0.25 \sin (0.00007275t) \geq - 0.025^{\circ}C\text{-m/sec} \qquad (53)$$

as suggested by the data of Wyngaard[17] for a summer day in Kansas. Removal of this heat source is accomplished by a constant radiation heat flux Q_R applied between the ground and 2 km for (in this computation) the entire 24 hours. The results of a typical calculation, requiring about 1/2 hour of computer time per simulated day, are given in the Appendix. The program expectedly computes the general features of the diurnal day. Of particular interest is the appearance of the low-level nocturnal jet (fig. A5) centered at 6 a.m. and 200 meters. It is worth noting also that the dynamic solution drives through neutral conditions at 8 a.m. and 8 p.m. At the morning neutral point, the surface shear stress u_* (in fig. A9) is lower than at the evening neutral point, while the surface angle α (in fig. A10) shows the reverse trend. This strongly suggests that although the turbulence equilibrates rapidly with changing surface conditions, the mean flow is noticeably slower to react. The turbulent energy q^2 (from fig. A4) establishes an inversion lid near 2.5 km. The "breaking through" of the early morning boundary layer is particularly vivid here, where by 11 a.m. the character of the q^2 profile has changed dramatically. This effect is carried over into the other variables as well. The hysteresis loop predicted for the surface shear stress as a function of stability (fig. A11) demonstrates the significant difference between a dynamic calculation of the boundary layer and a static calculation.

To gain a larger understanding of the effect of the dynamic scale equation (24), the above-noted calculations have been repeated using the same assumptions and boundary conditions with two variations. It seems clear that the heat generated during the day is probably removed during the nighttime hours. Thus, in the run here quoted, Q_R was doubled but only implemented between the hours of 8 p.m. and 8 a.m. Also, the dynamic scale equation was included in the computation. Figure 14 gives the surface stress u^* as a function of time for the three days of calculation. A comparison with fig. A9 shows a close similarity except for the times between 10 and 11 a.m. where fig. 14 shows three highly repeatable oscillations. This effect apparently may be attributed to the dynamics of the scale motion. At this time of day, the inversion lid is being blown to high altitudes, as shown in fig. 15 for the kinetic energy q^2. A comparison with fig. A4 reveals that the inversion lid now reaches 3.5 km and the intensity of the turtulence at the middle altitude has increased by 20%. The rise in q^2 before noon is still quite dramatic; its falloff past midnight is slower due primarily to the presence of large scale, as shown in fig. 16.

The dynamic scale A still reveals some of the 'boxiness' of the gross scale (shown in fig. A8) and reaches a maximum scale of nearly twice the gross scale. It behaves markedly different in the early morning hours, where the dynamic scale equation predicts a slow decay rather than the sharp drop off predicted in fig. A8. However, this large scale difference does not particularly affect the calculations, since it occurs in regions of small q^2. Plots of the other variables show much the same effects, supporting the contention that the gross scale features (eq. (25)) give a reasonable representation of the dynamics of the scale motion.

C. TURBULENCE DISTRIBUTION IN THE NEIGHBORHOOD OF AN ABRUPT CHANGE IN SURFACE ROUGHNESS

The boundary layer equations in streamline coordinates (eqs. (27) - (34)) may be used to compute the reaction of the near-wall boundary layer to an abrupt change in surface roughness z_o. A calculation was made in simulation of the atmospheric surface data of Bradley[16] who recorded drag, shear, and velocities at a little-used airfield in Australia. Transitions were made from rough-to-smooth and smooth-to-rough where the hydrodynamic height z_o was used as a measure of the roughness of the surface. Bradley's "smooth" surface consisted of sand and small pebbles for which $z_o = 0.002$ cm.

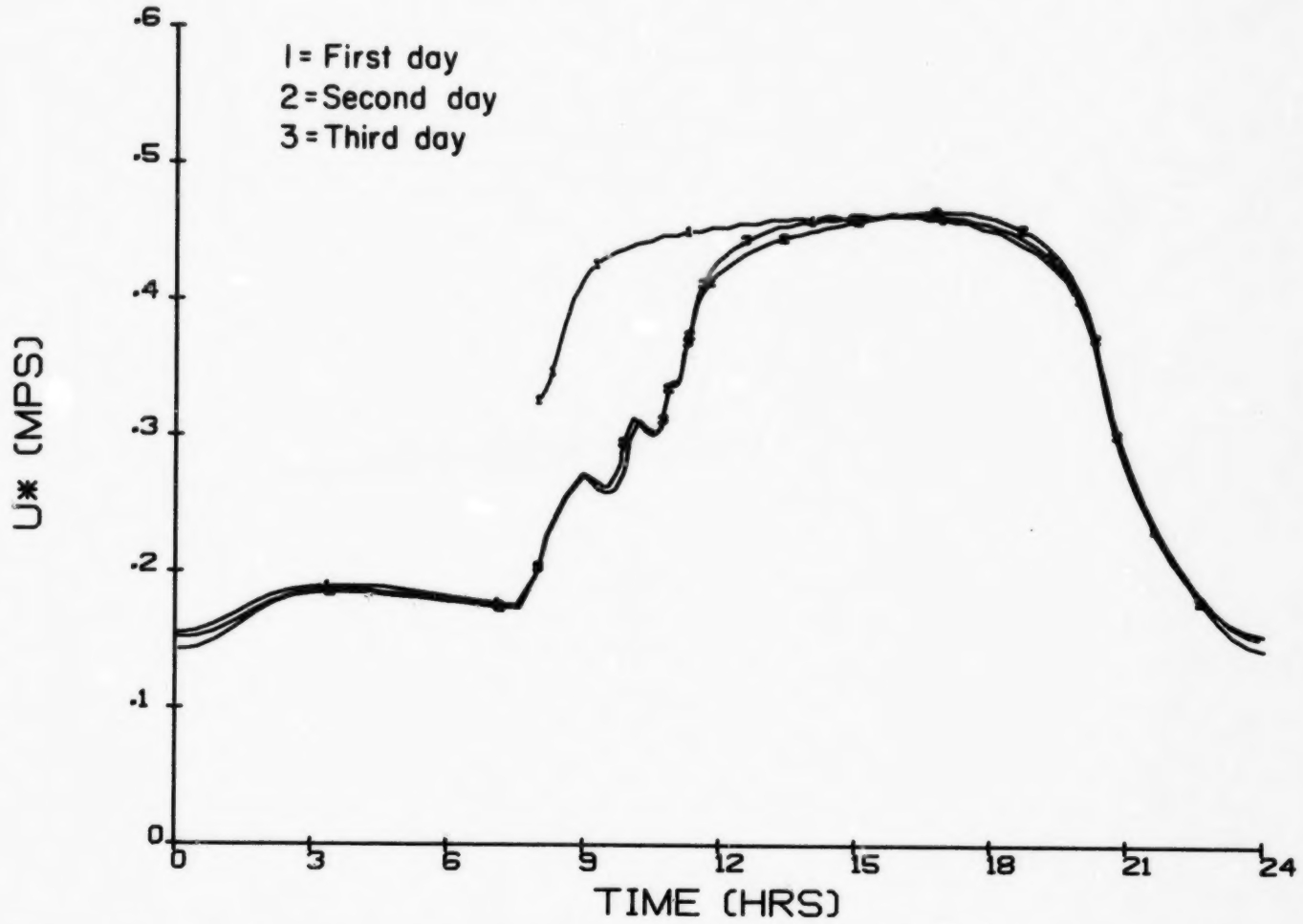

Figure 14: Surface shear velocity as a function of time for a diurnal surface heat variation as predicted by a calculation using the dynamic scale equation (compare with fig. A9).

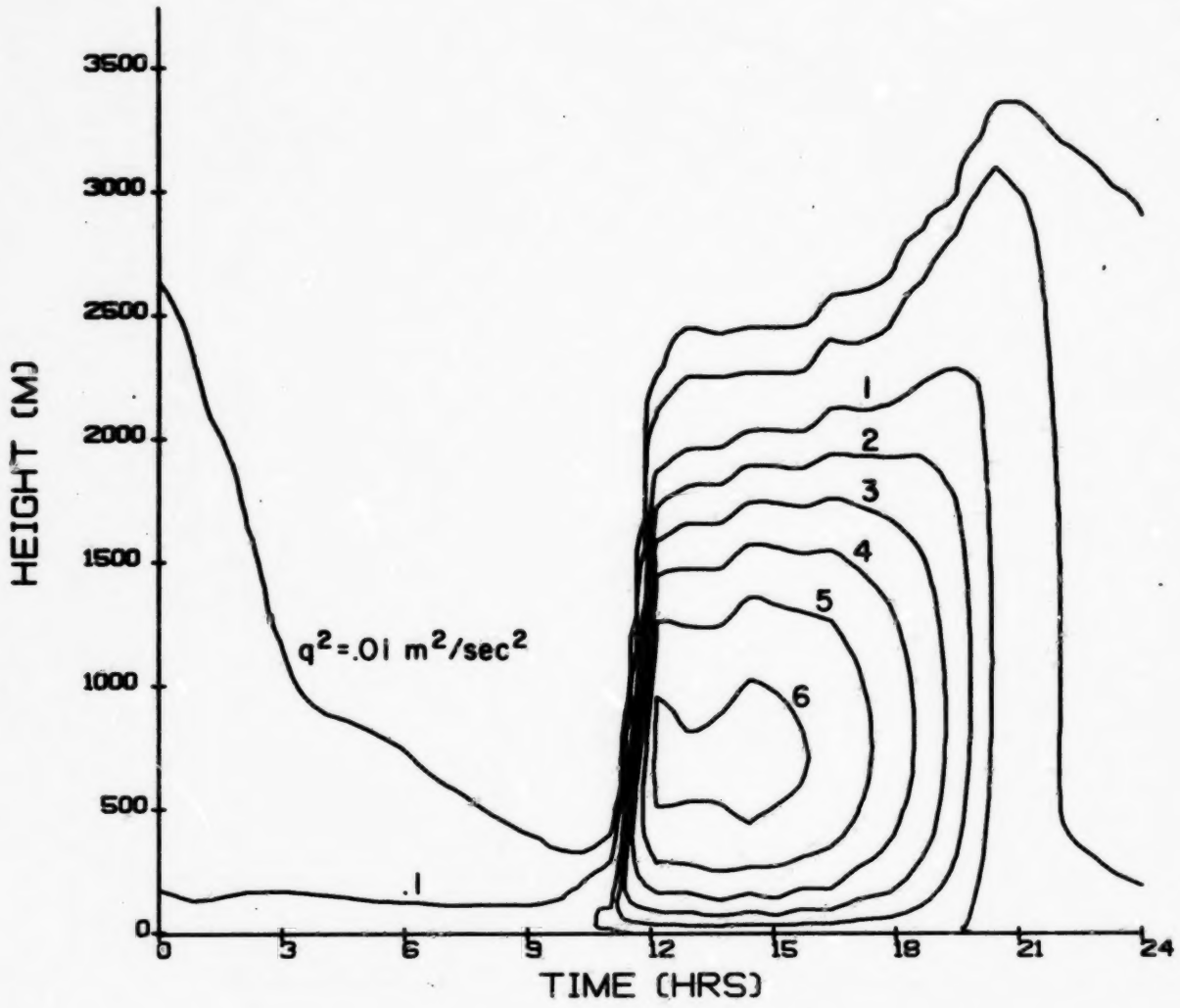

Figure 15: Contours of constant q^2 as a function of altitude and time of day as predicted by the model using the dynamic scale equation (compare with fig. A4).

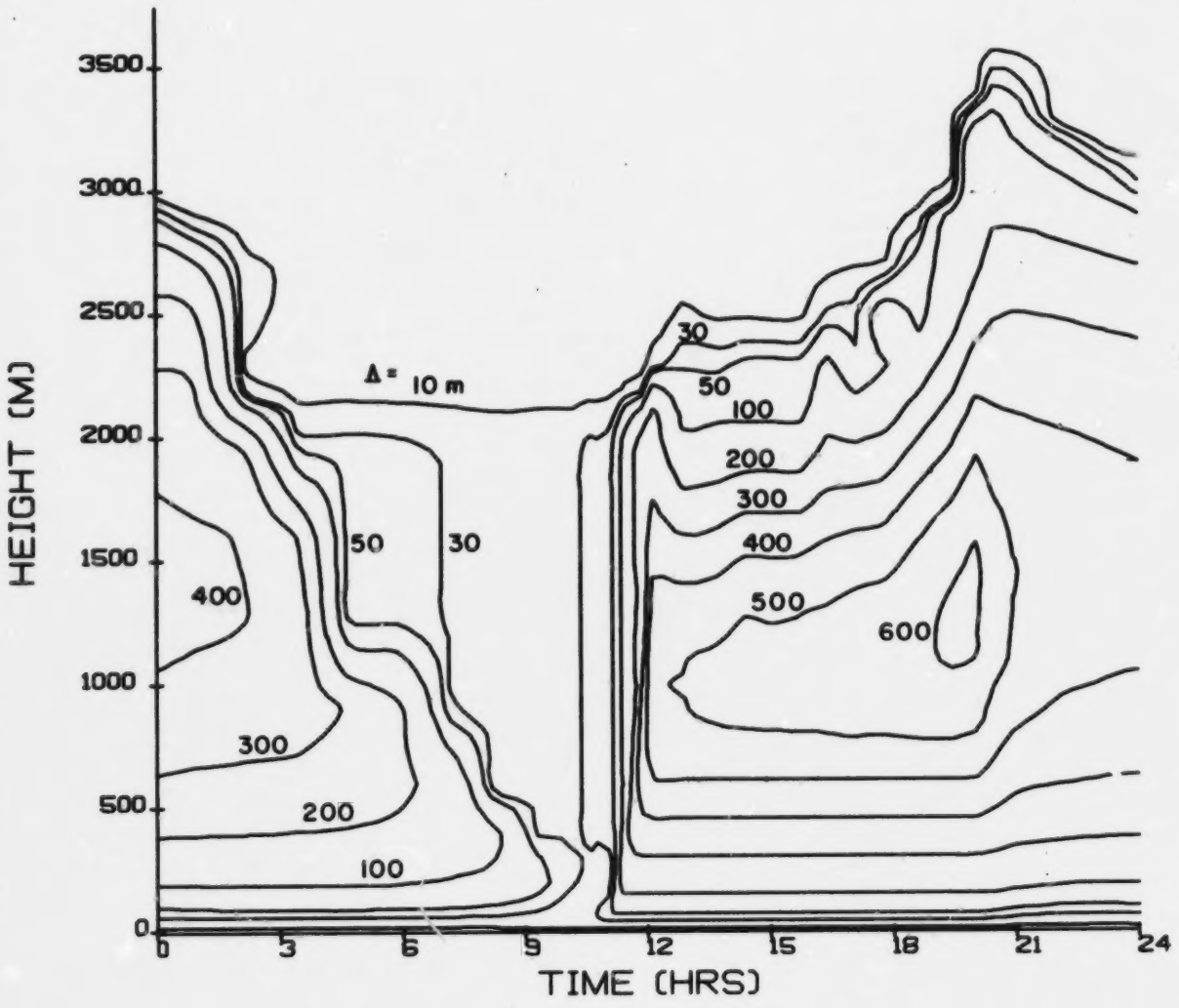

Figure 16: Contours of constant length scale Λ as a function of altitude and time of day as predicted by the model using the dynamic scale equation (compare with fig. A8).

His "rough" surface was a man-made structure of snipped reinforcing mesh for which $z_o \approx 0.25$ cm.

Our calculations begin with z_o fixed at one of these values and run until the variables appear to reach a steady state (remembering that we are mostly concerned with the response picture below about 10 m). With these steady profiles, then, we change the z_o to its other value and track the response of the boundary layer to this abrupt change in surface roughness. The results for both cases are shown in fig. 17. Comparison with a great deal of Bradley's data shows good agreement. Here we plot the shearing stress (normalized by its previous steady state value) versus the x distance downstream (denoted as "fetch"). When both runs are allowed to continue far downstream, they come into equilibrium with their new $z_o$values. The steady state value for smooth-to-rough is $\tau/\tau' = 1.88$ while rough-to-smooth gives $\tau/\tau' = 0.532$. Our results are very similar to the numerical results reported by Shir[19].

In a later section of this report we discuss the spatial dispersal of pollutants across a change in surface roughness. For this case we will increase the two z_o values by two orders of magnitude so that the transition corresponds roughly to that between grass land and suburban land using the rough rule of thumb that z_o = 1/30th of the physical height of the roughness elements[20].

Contours of constant stress for this case are shown in fig. 18 as a function of height and distance downstream of the change in roughness (smooth-to-rough transition). The largest values of shear stress occur in the immediate vicinity of the roughness discontinuity. At altitude, the shear stress remains constant until the influence of the step is felt, when the edge of the inner boundary layer growing from x = 0 reaches that altitude.

The turbulence components computed in this way are used in the pollutant dispersal calculations in Section VI D.4.

D. DISPERSAL OF A NEUTRAL PLUME UNDER VARIOUS TYPICAL CONDITIONS

Plume diffusion in typical turbulence has been computed using our three-dimensional program, 3PD (one flow direction x plus diffusion in two directions y and z). The wind and temperature distributions needed are taken from output of

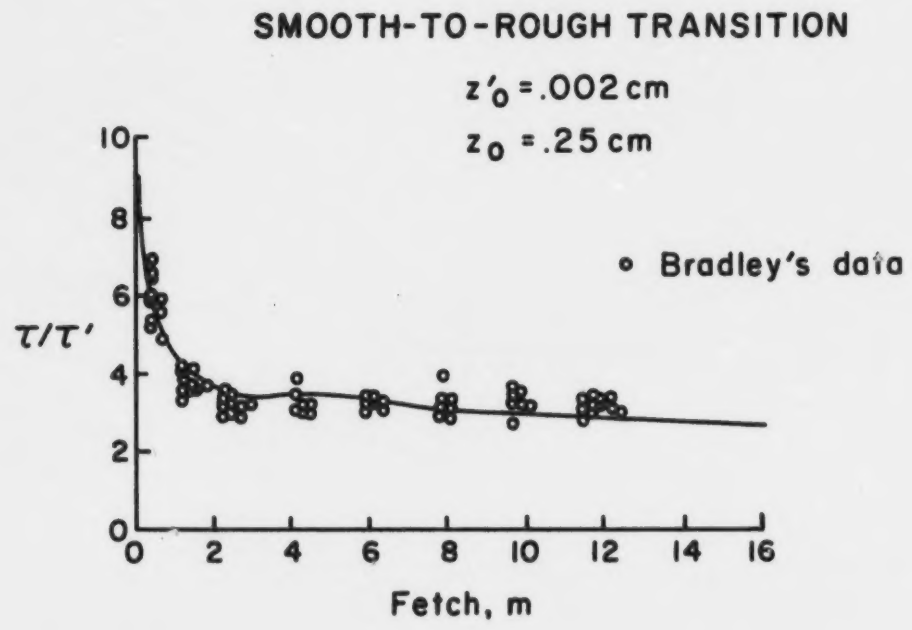

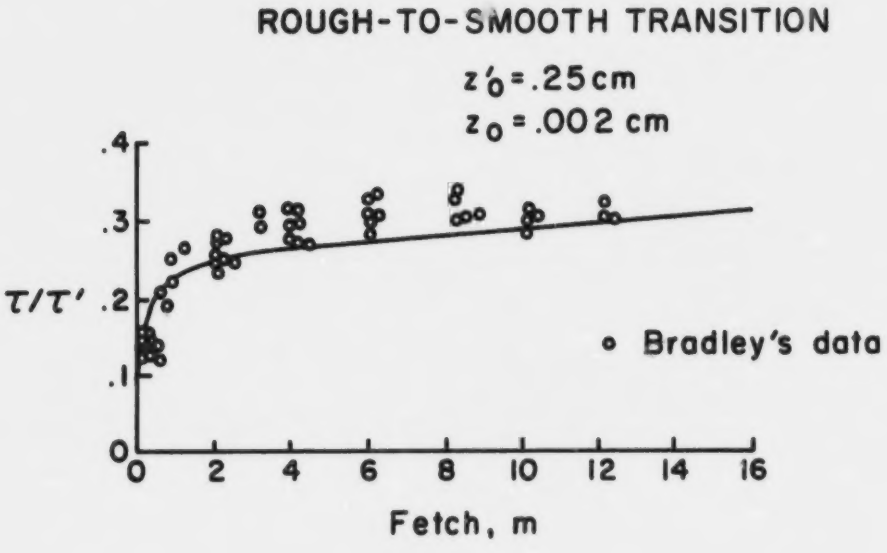

Figure 17: Surface shear stress as a function of distance downwind of a step change in surface roughness as predicted by the model (—) and as observed by Bradley (o) (ref. 18).

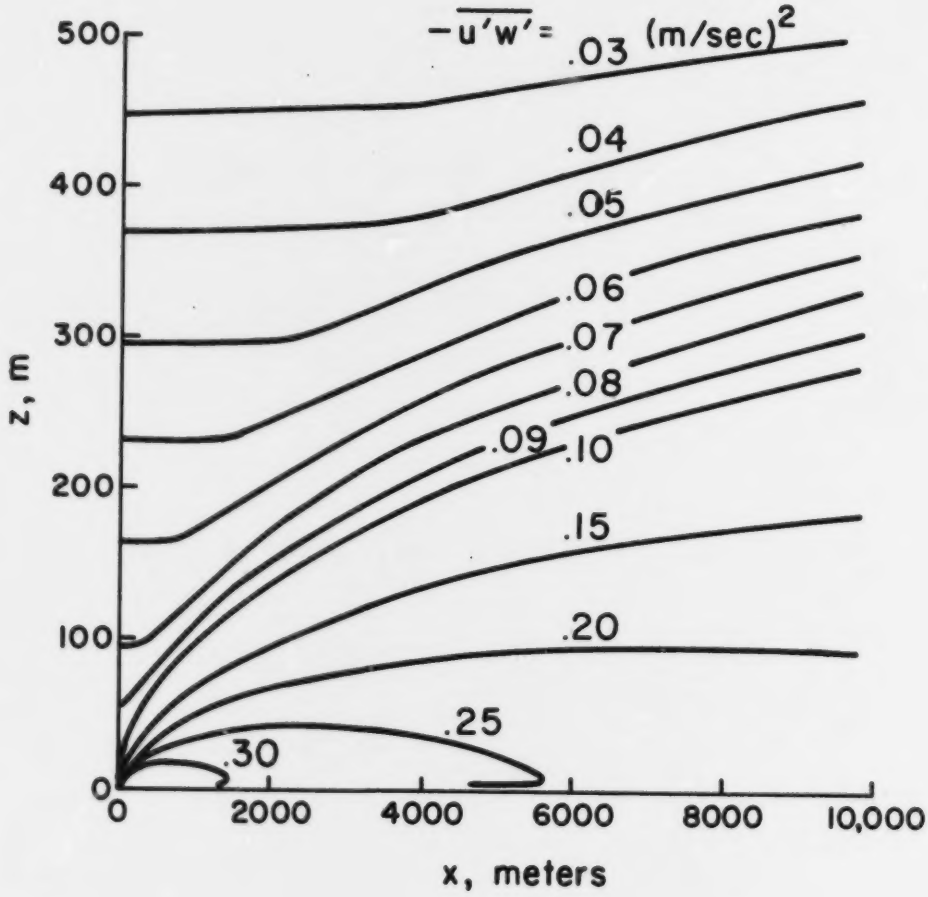

Figure 18: Contours of constant shear stress in the vicinity of a change in roughness from 0.002 m to 0.25 m (u_g = 10 m/sec, neutral stability).

the planetary boundary layer program. Variation with respect to three variables - time of day or atmospheric stability, stack height, and stack position with respect to surface innomogenities - have been exemplified.

D.1 In An Unstable Atmosphere

Results of the calculations for the diurnal variations in the planetary boundary layer[11] show that the average velocity and temperature profiles existing at noon on a typical summer day in Kansas are highly unstable. In order to simulate experimental measurements, the velocity and temperature profiles generated by the PBL model were time-averaged over one hour intervals and the average profiles input to the clear air turbulence program to obtain corresponding average equilibrium turbulence for each hourly interval. The wind, temperature and distribution used in the present calculation are shown in fig. 19. It should be noted that this is not equal to the output of PBL at any one time.

The pollutant was released into these turbulence fields from a point source at a height of 100 m with an assumed source strength of 100 units/sec. The initial concentration was bivariate normal with $\sigma_y = \sigma_z = 1$ meter. Plume diffusion was computed for 20 km or until a five-order-of-magnitude dilution of the maximum concentration was achieved.

Figure 20 shows the dilution of the maximum concentration as a function of distance downwind. Two significant irregularities stand out on this otherwise smoothly decaying curve. Close to the release point the meandering of the plume causes the maximum averaged concentration at any point to drop relatively rapidly. Then, as diffusion begins to overtake meandering as the dominant dispersal mechanism, the decay rate flattens out, since in this region the plume is diffusing into an area where an average concentration already exists because the plume occasionally meandered into it. The second kink in the curve, occurring at about x = 750 m, occurs as the plume impinges upon the ground. Since the ground acts as a reflecting plane (assuming no absorption at the surface), the altitude of the maximum concentration is gradually reduced until it reaches ground level.

The spatial history of the plume is displayed as a series of mean concentration isopleths in fig. 21. A cross section of the plume is shown at the prescribed x distances downstream of the release point. Each cross section contains contours of constant fractions of the (integer noted times 10^{x}) local

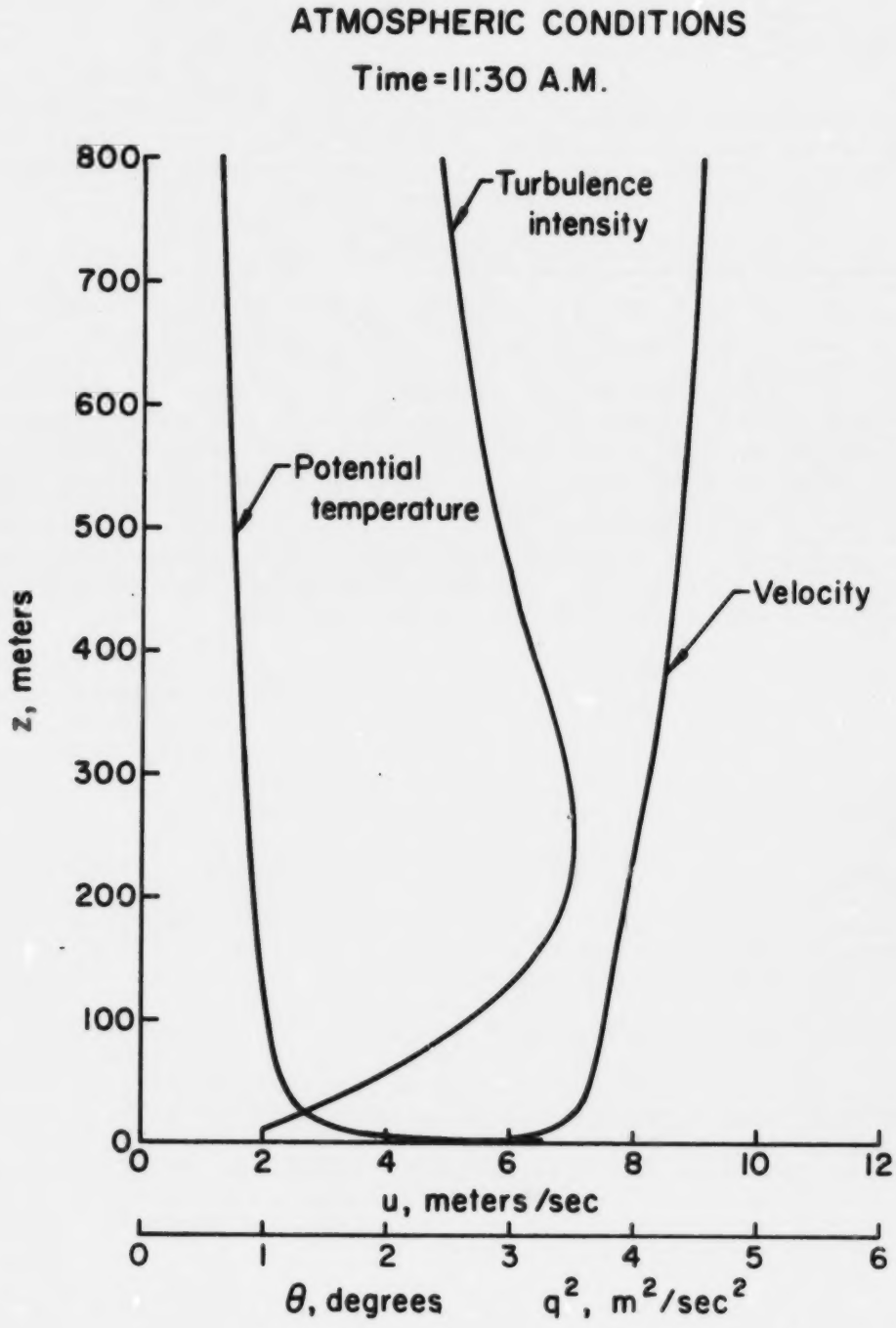

Figure 19: Atmospheric conditions assumed for the unstable plume calculations.

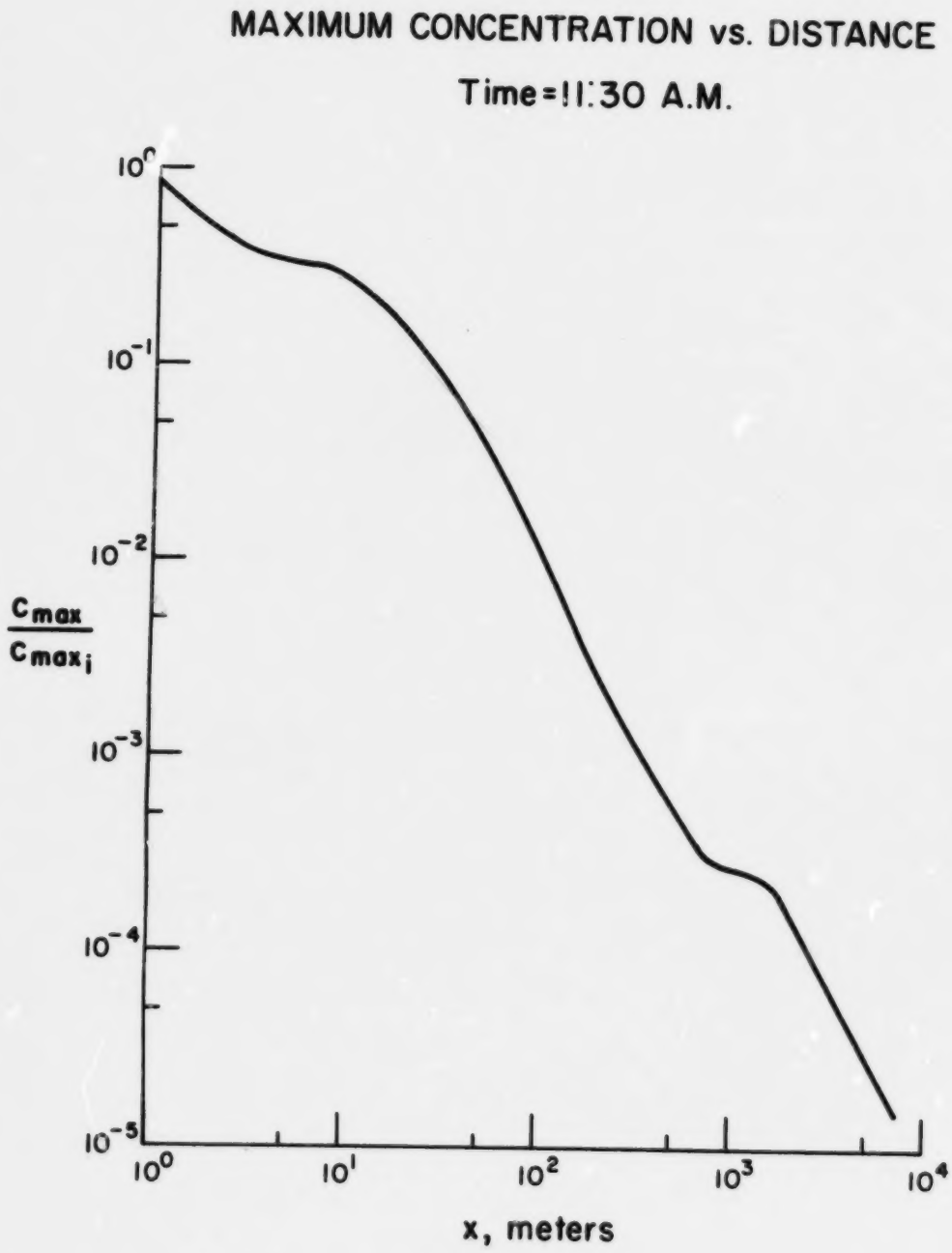

Figure 20: Decay of maximum concentration as a function of distance downwind of an effective 100 m stack in atmospheric conditions prescribed by fig. 19.

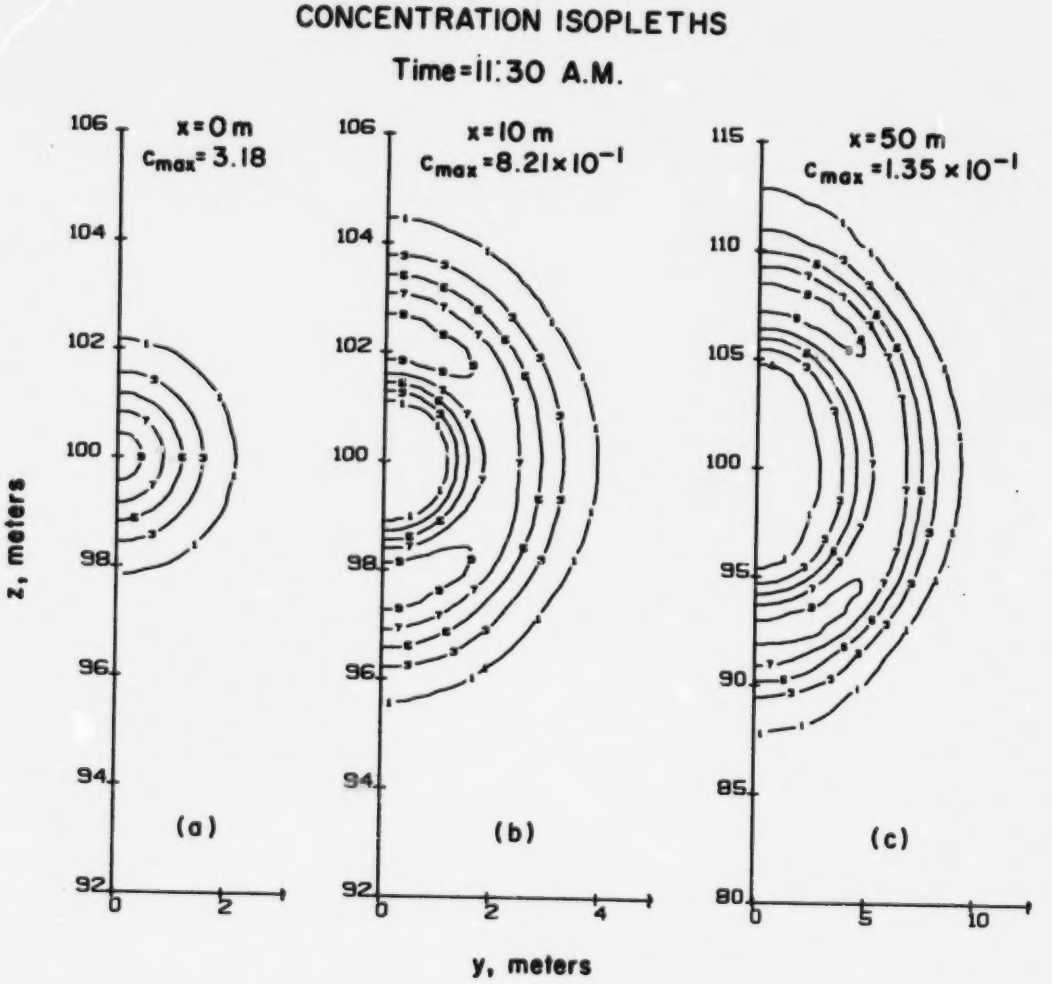

Figure 21: Contours of constant mean concentration at various distances downstream of a 100 m stack in atmospheric conditions prescribed by fig. 19 a) x = 0 m, b) x = 10 m, c) x = 50 m, d) x = 250 m, e) x = 500 m, f) x = 1 km (the contours are labeled with 9 = 90% of maximum, 7 = 70%, etc.).

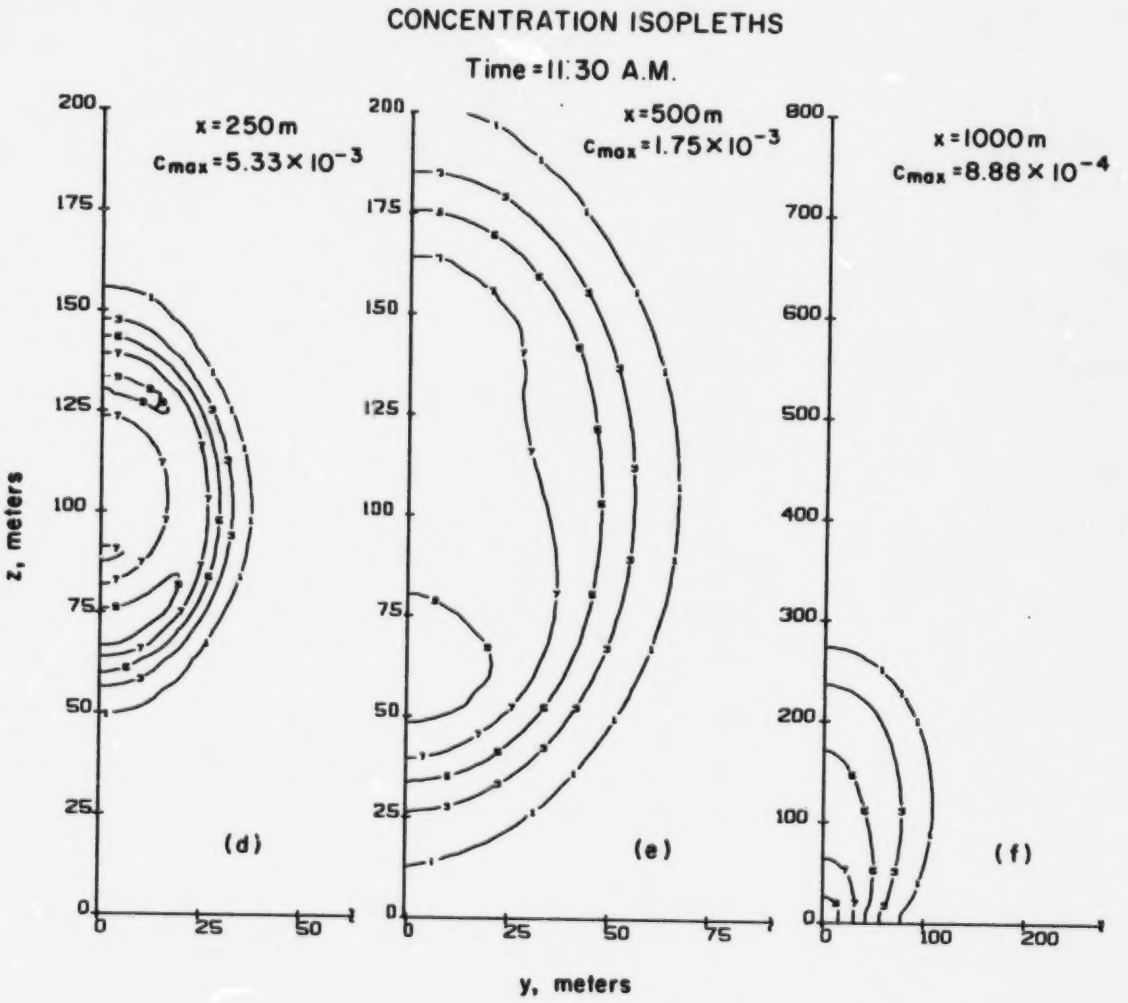

Figure 21: Continued

maximum concentration. Cross section (a) contains the initial Gaussian distribution. Cross section (b) shows the plume beginning to meander about its center (as the plume meanders over some area it spends a smaller fraction of its time at the center of that area than at its turning points so that the time averaged concentration has its maximum in an annulus around the centerline). Cross section (c) shows the meander area further increased with the plume spending a negligible fraction of its time along the centerline. Cross section (d) shows the plume centerline filling in as the scale of the plume approaches the scale of the background turbulence and the diffusion character of the transport equations begins to dominate the initial wave-like character. Cross section (e) shows the plume completely dominated by diffusion but it now shows a distortion in height mirroring the z variation in wind and turbulence intensity. Cross section (f) shows the maximum local concentration having reached the ground with the edges of the plume continuing to expand in y and z.

Figure 22 is a repeat of the last figure but shown in perspective computer drawings. Cross sections are shown at the same distances as in the previous figure but now the concentration level is illustrated by the height of curve to give a different view of the phenomena just described. Note that all of the drawings are not made to the same scale.

Figure 23 is a plot of the vertical and horizontal standard deviation of the concentration distribution as a function of distance downwind of the stack. The dashed lines show the same quantities as computed using the old model as given in ref. 1 prior to the modifications described in Section V of this report. The major difference is in the early phase of the plume where meander is important. These results compare favorably with the dispersion estimates presented by Pasquill and Gifford for various conditions of atmospheric stability[21]. The turbulence field described above approximates the Pasquill stability class C. At x = 1 km, the Pasquill curves yield σ_z = 65 m and σ_y = 100 m, whereas our computations yield σ_z = 70 m and σ_y = 50 m.

Figure 24 is an attempt to compare our model predictions with observations of meandering plumes. Wasko and Moses[22] observed plumes under stability conditions similar to that used in our computations. Although these background atmospheric conditions are not described adequately for us to make detailed comparisons, we have taken their ratio of the area over which the plume meanders to the instantaneous plume area and compared it to a rough measure of the same ratio from our calculations. Since we do not have computations of the

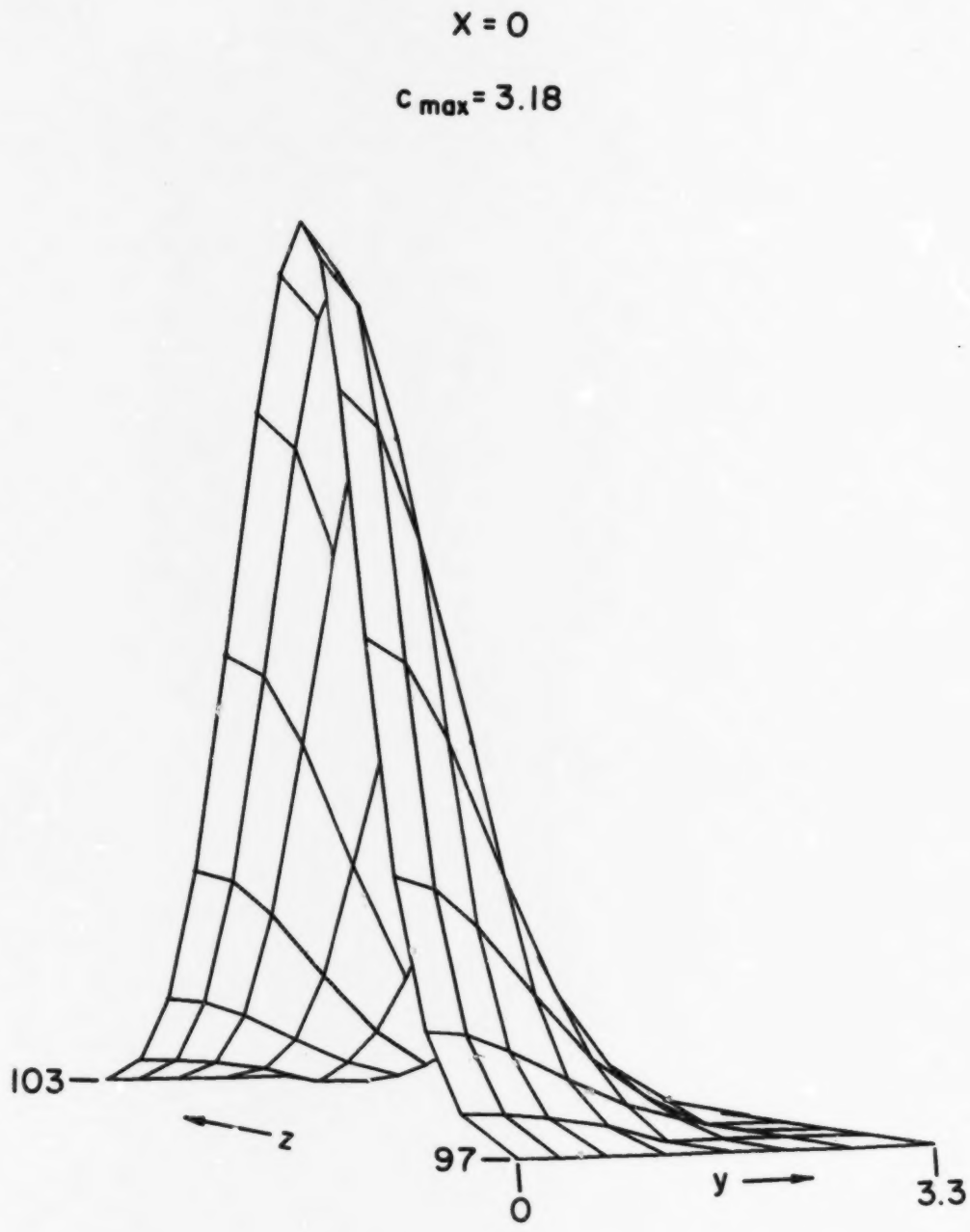

Figure 22: The same information as supplied in fig. 21 with the concentration profiles now shown in perspective. Note the scale changes at different x stations.

X=10

$c_{max}=8.21\times10^{-1}$

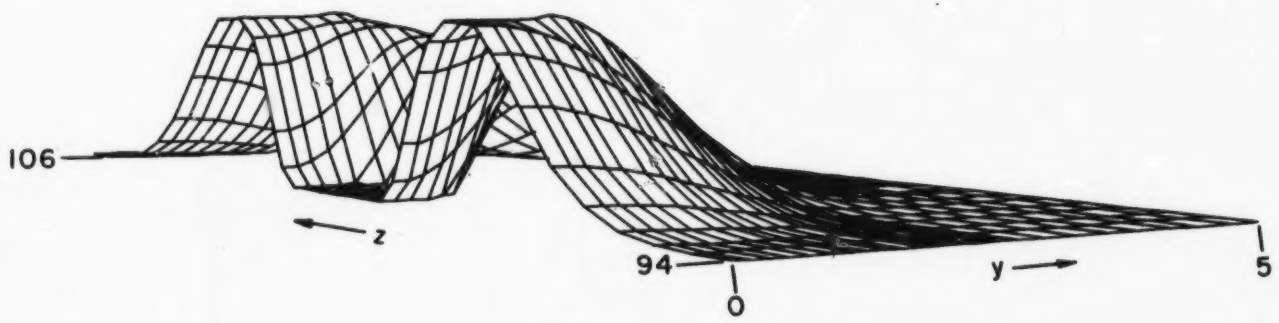

Figure 22: Continued

X = 50

$C_{max} = 1.35 \times 10^{-1}$

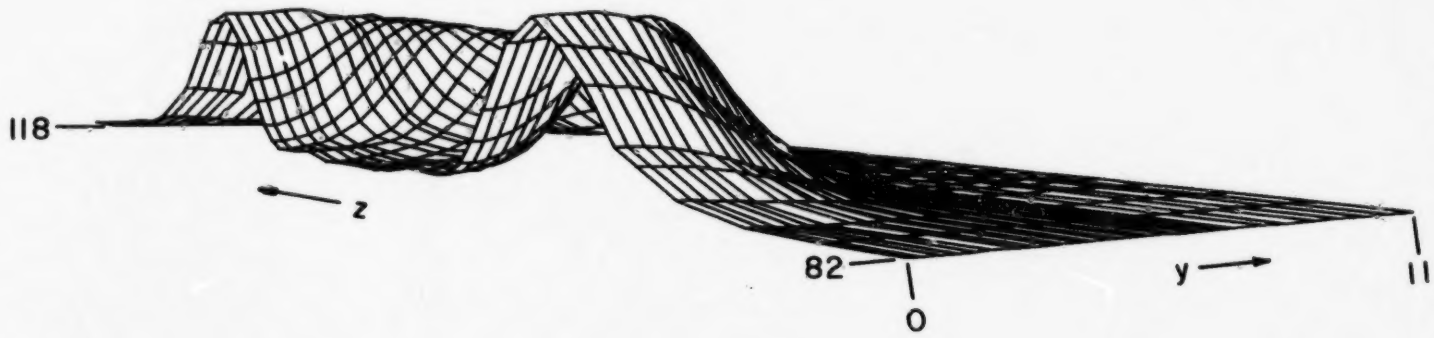

Figure 22: Continued

$X = 250$

$c_{max} = 5.33 \times 10^{-3}$

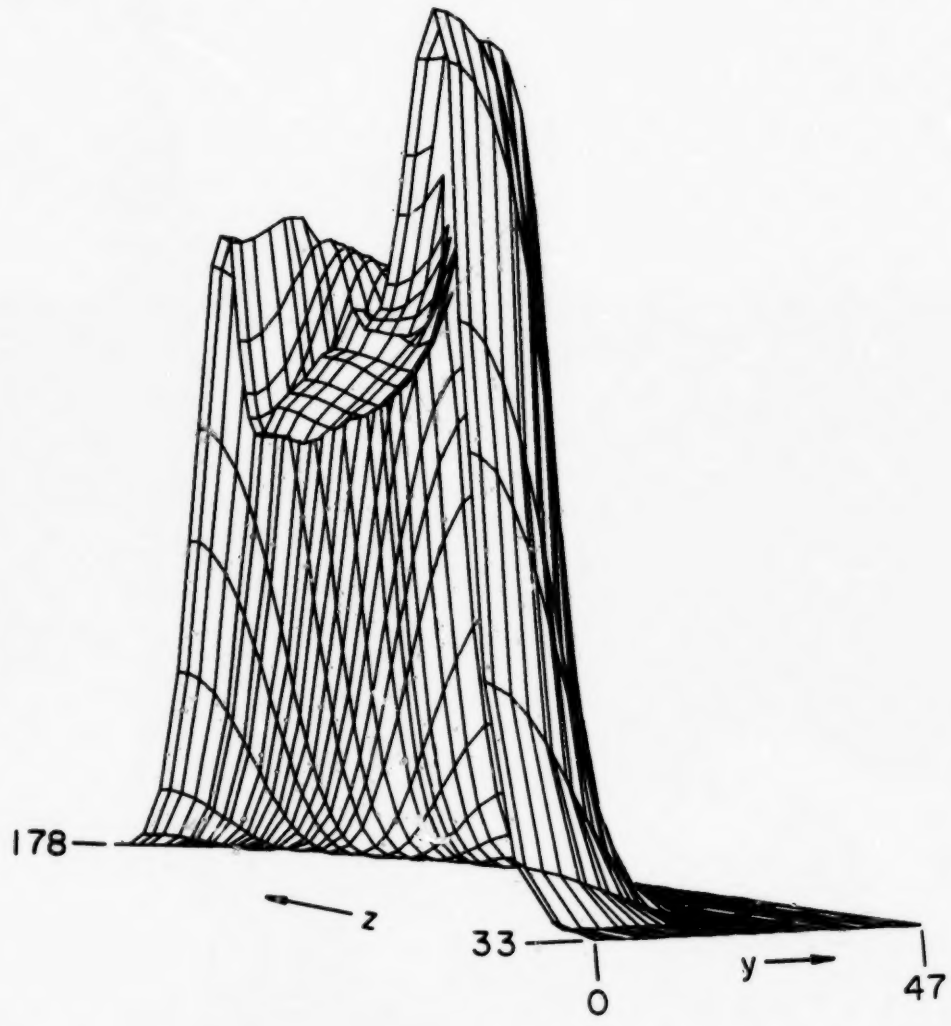

Figure 22: Continued

X = 500

$c_{max} = 1.75 \times 10^{-3}$

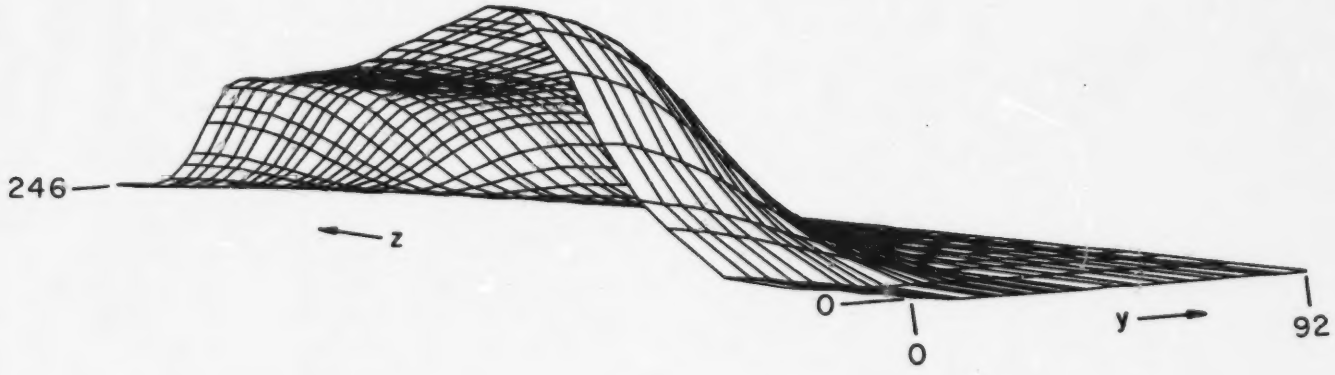

Figure 22: Continued

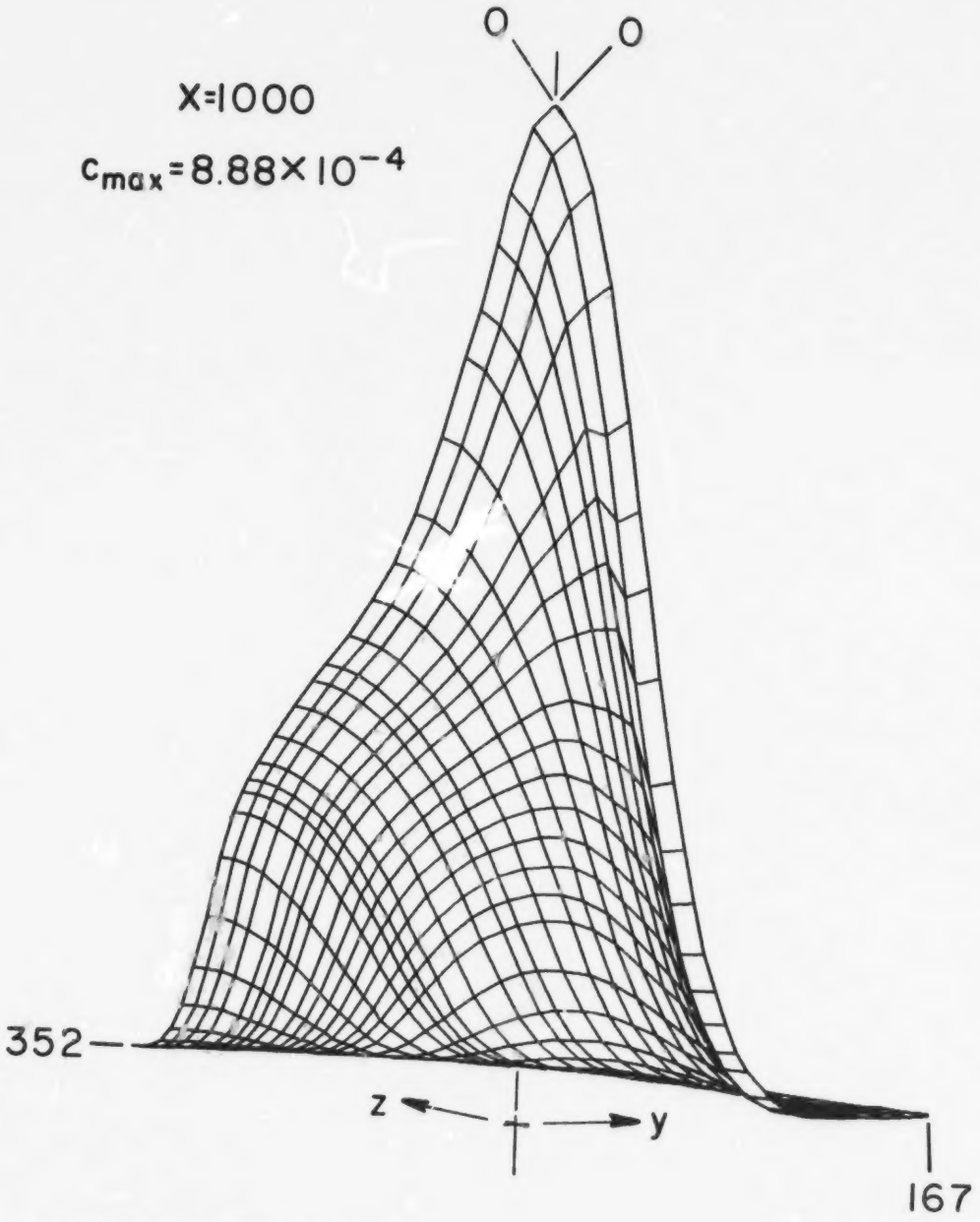

Figure 22: Continued

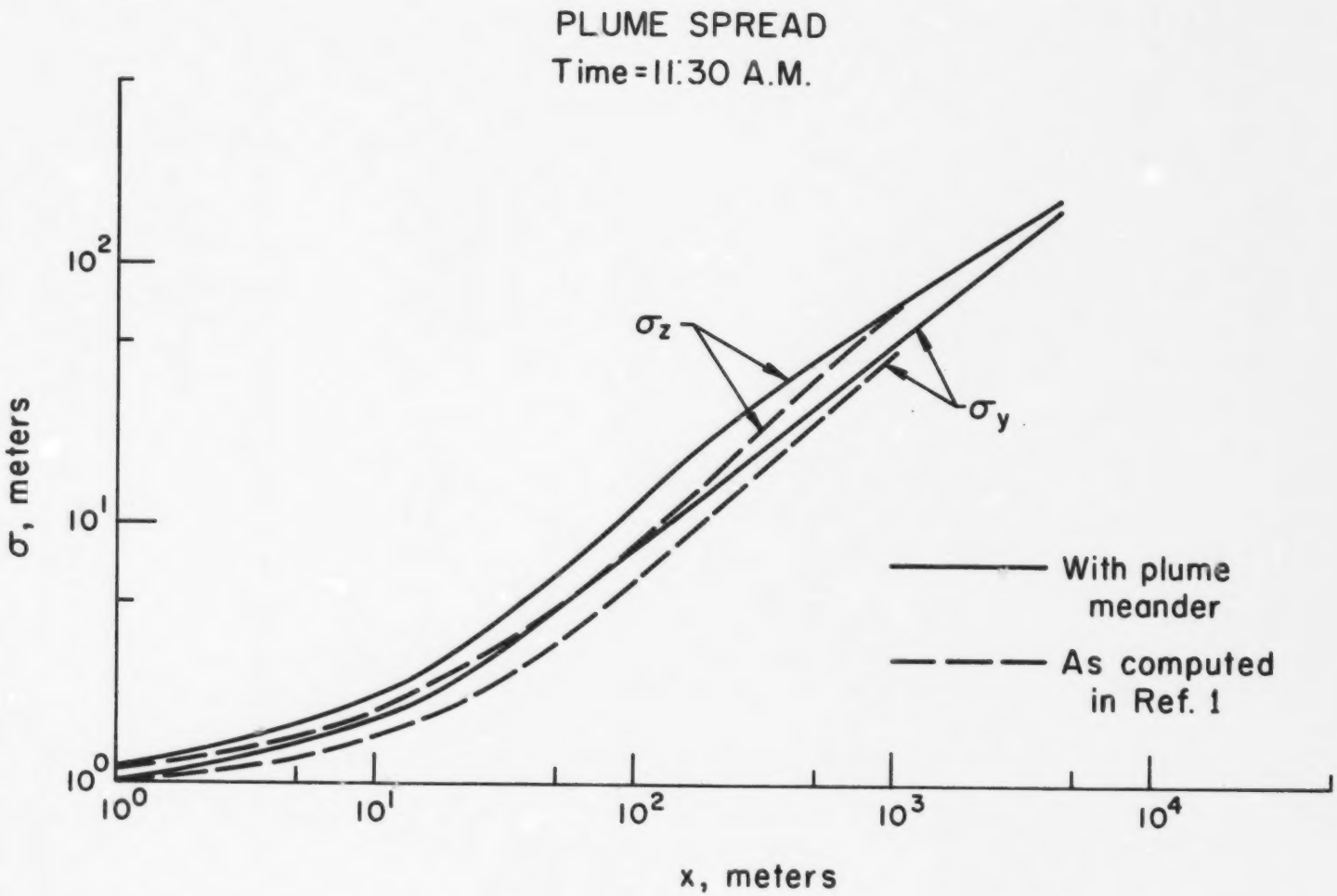

Figure 23: Standard deviation of the unstable plume as a function of distance downwind of release point.

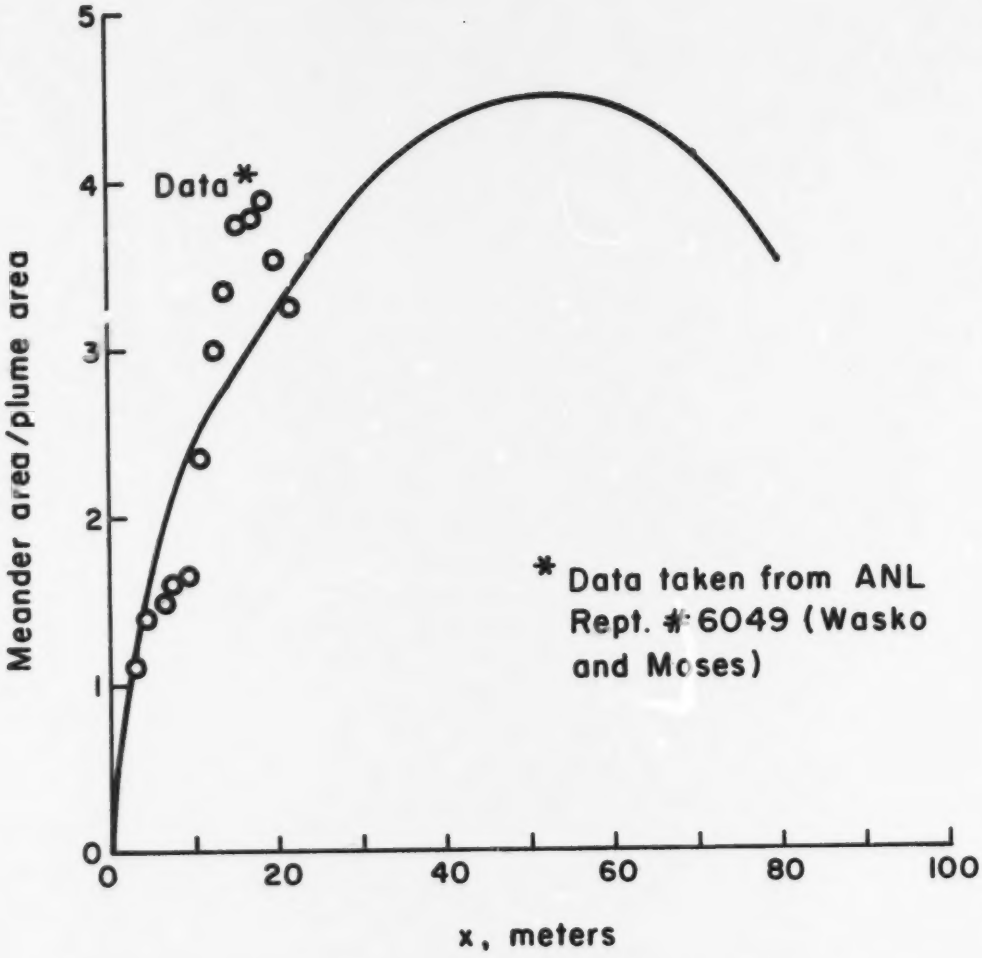

Figure 24: Ratio of meander area to instantaneous plume area as a function of distance downwind of release as predicted by the model for unstable conditions and as observed by Wasko and Moses[22].

instantaneous plume we have taken the square of the ratio of the shortest distance between 50% concentration lines and the maximum distance between 50% concentration lines to be a fair measure of the same quantity. Thus, although fig. 24 is not a precise quantitative verification of our model, it does constitute a qualitative check.

Figure 25 shows spatial plots of the contours of constant values of concentration fluctuation correlation, $\overline{C'C'}$, at the same downstream position as that of the concentration isopleths of fig. 21. The initial distribution is arbitrarily taken as Gaussian with a small maximum value as shown in (a). The fluctuation increases and spreads to that given in (b) 10 meters downstream of the initial station. At this station the maximum fluctuation occurs in an annulus as did the maximum mean concentration but the contours are more spread out.

Subsequent cross sections also show the $\overline{C'C'}$ contours to be more uniformly spaced than the mean concentration contours of fig. 21. The last cross-section at 1,000 m shows the maximum to have moved up in altitude rather than down to the surface as did C, demonstrating that the position of maximum concentration fluctuations can be far away from the position of maximum mean concentration.

D.2 In a Stable Atmosphere

A contrasting run was made for conditions at 0:30 hours obtained by averaging the mean wind and temperature distributions for the hour centered about this time in the same manner as was done in the unstable case. The input conditions are shown in fig. 26. Again we note that this does not correspond to the turbulence existing at any given time during the diurnal calculation but rather corresponds to equilibrium turbulence existing for the hourly averaged mean wind and temperature. The initial conditions of the plume are the same as those for the unstable case.

Figures 27 - 28 show the decay of the maximum concentration and the concentration isopleths at different cross sections. The maximum concentration decays at a much slower rate than in the unstable case due to the lower turbulence intensities. The meander phase of the plume exists for a longer distance, until approximately 500 meters, but we note a much weaker effect on the contours because of the reduced scale of the background turbulence. In following the plume to 20 km, the maximum concentration has only decayed by three orders of

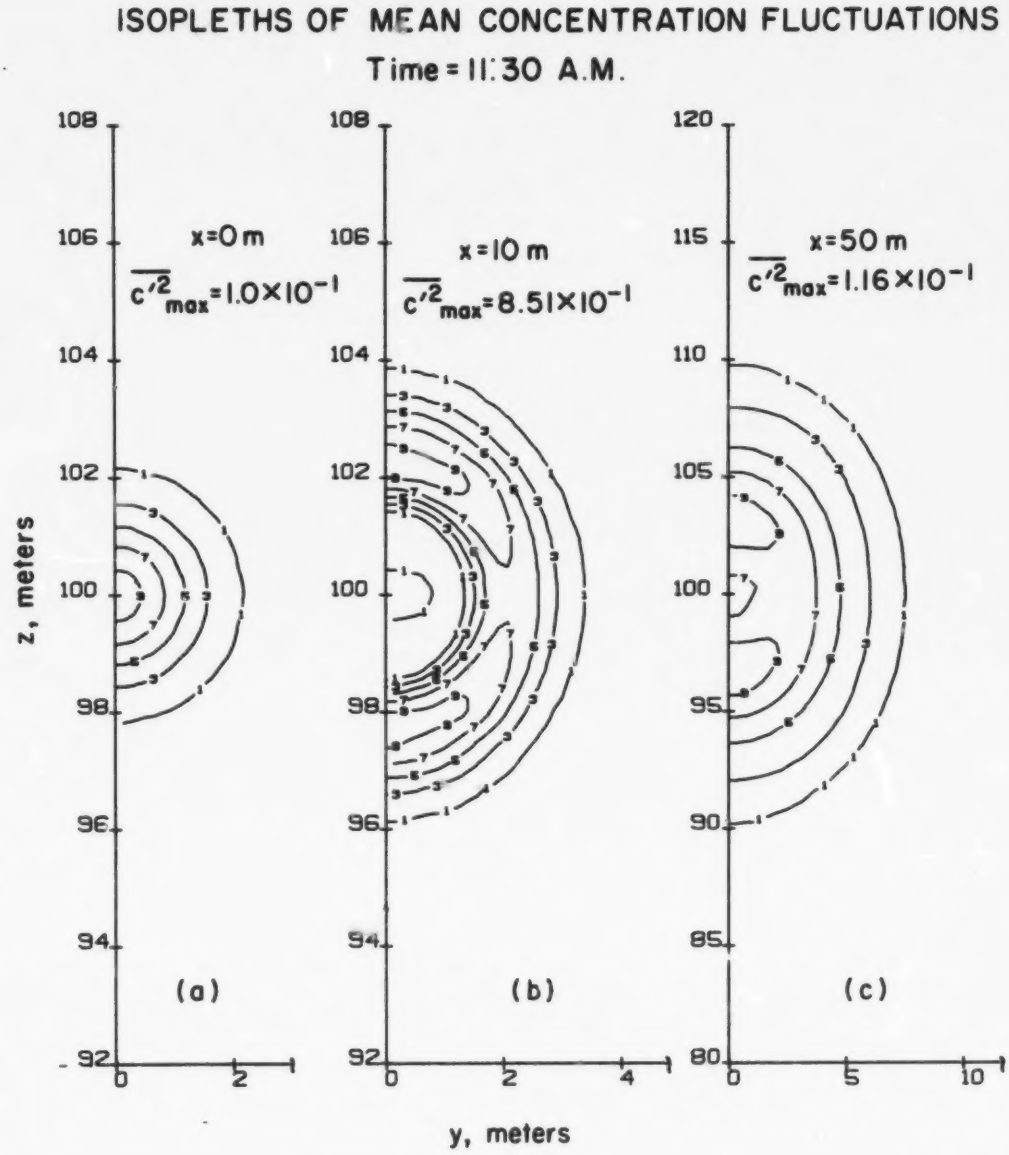

Figure 25: Contours of constant values of $\overline{C'C'}$ at the same x stations as given in fig. 21.

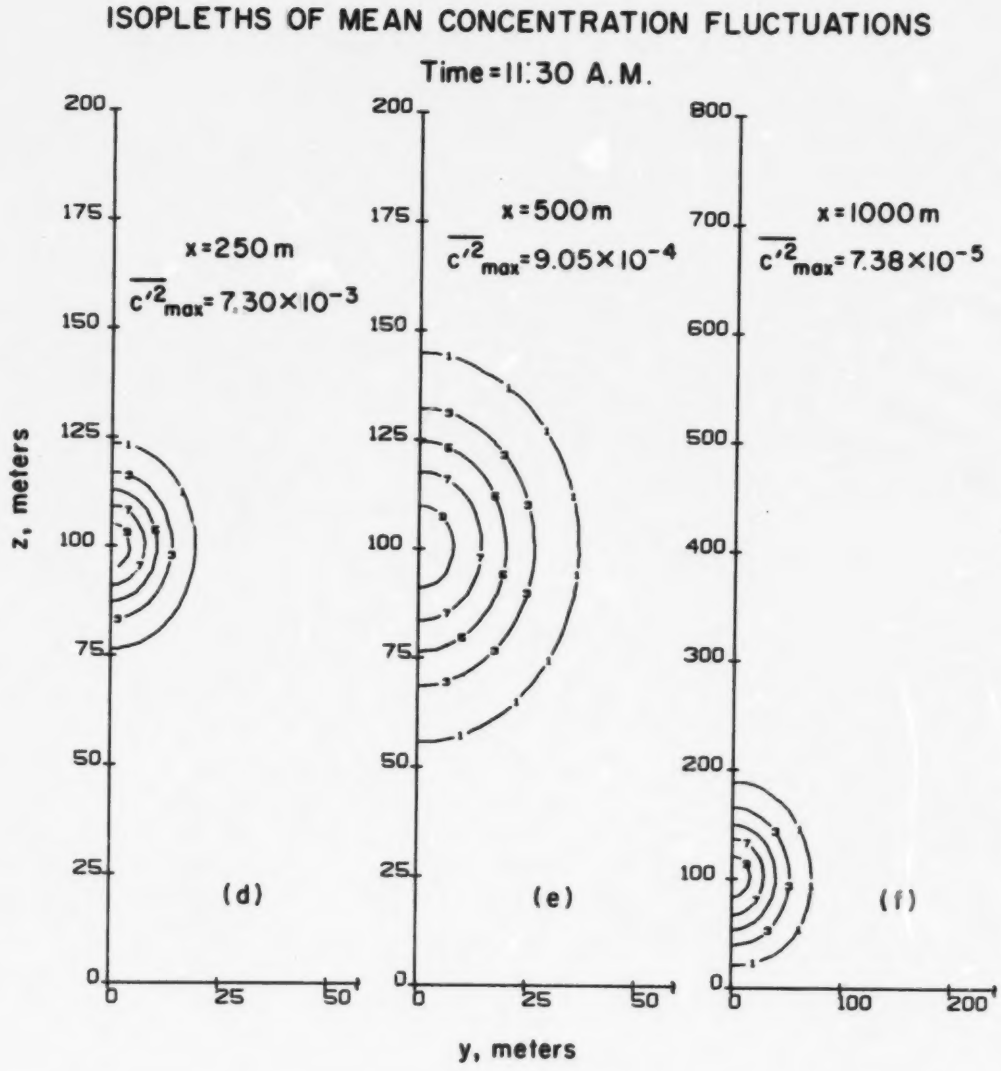

Figure 25: Continued

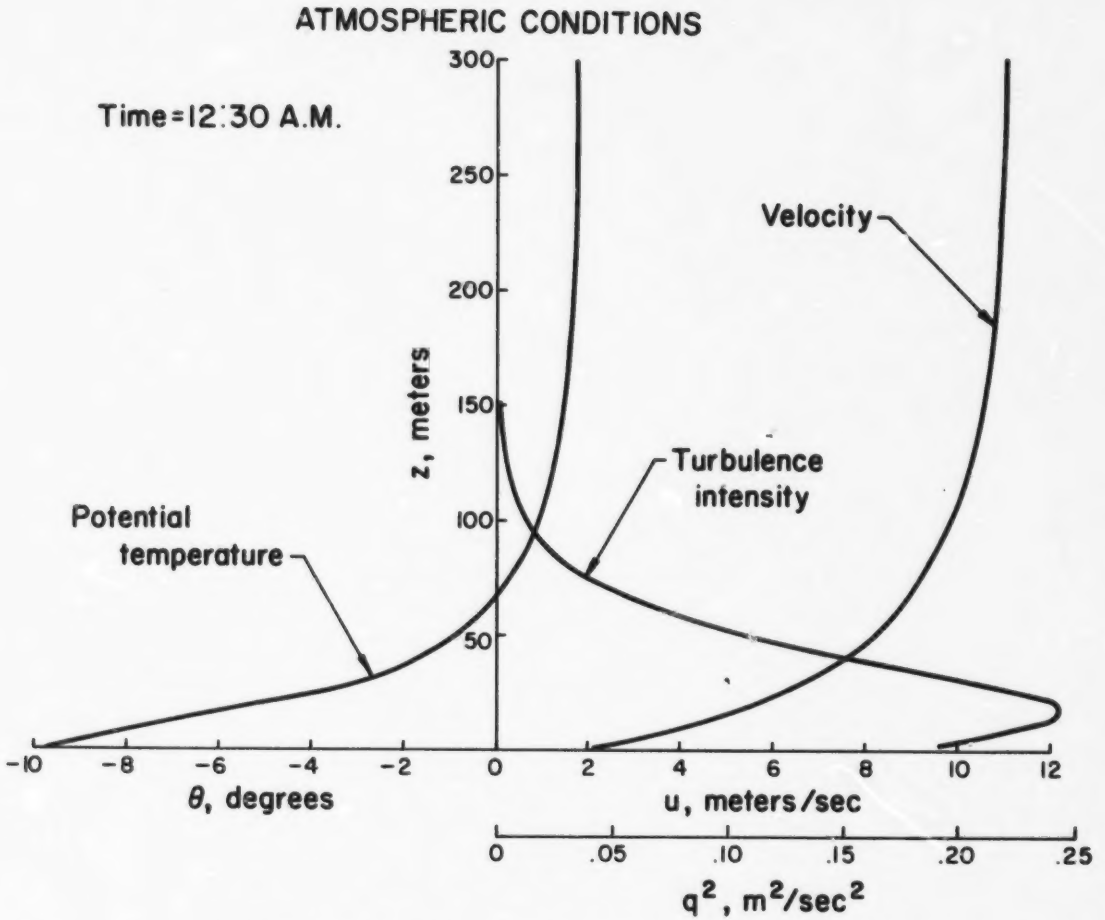

Figure 26: Atmospheric conditions assumed for the stable plume calculations.

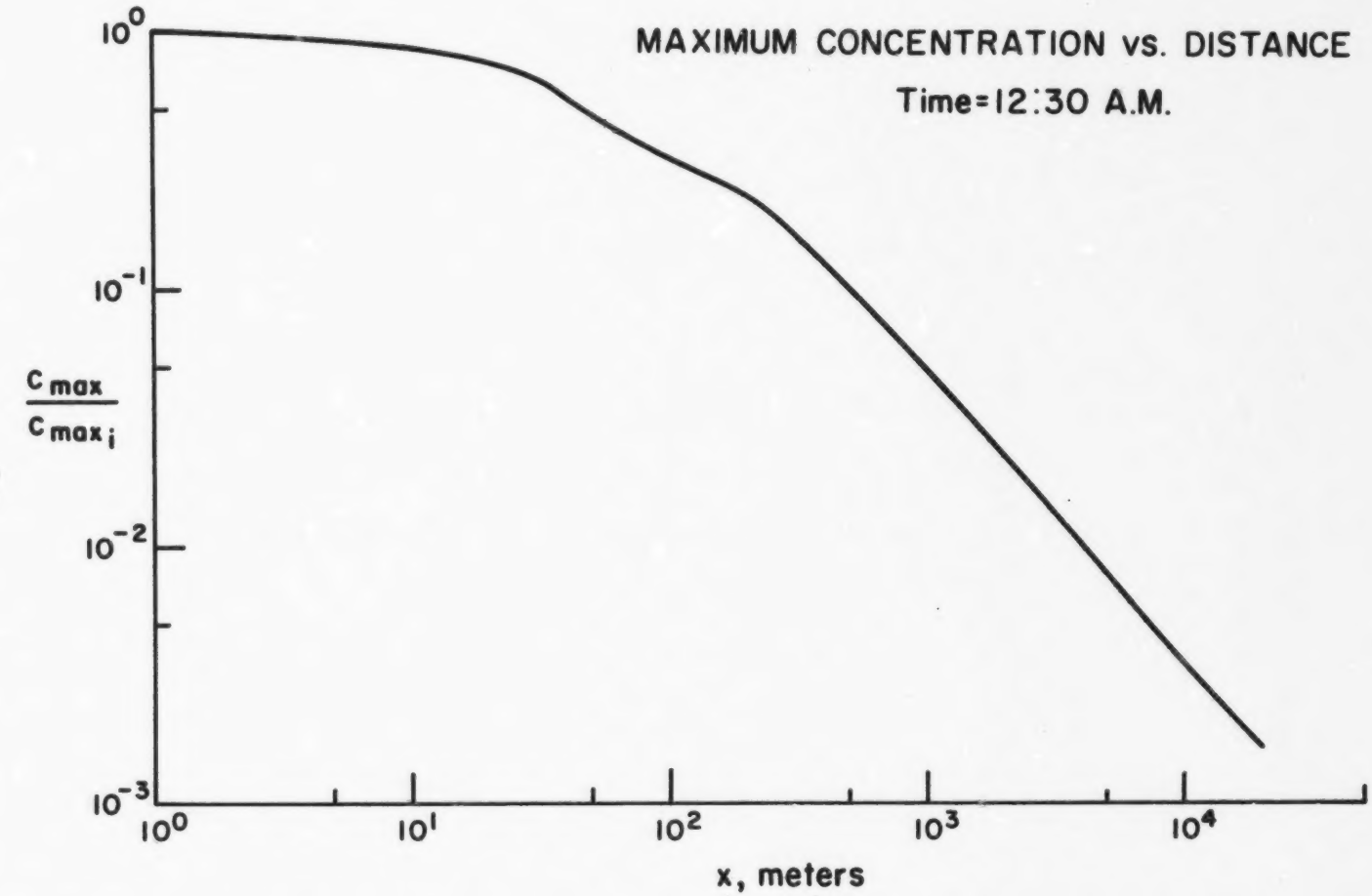

Figure 27: Decay of maximum mean concentration as a function of distance downwind of a 100 m stack in atmospheric conditions prescribed by fig. 26.

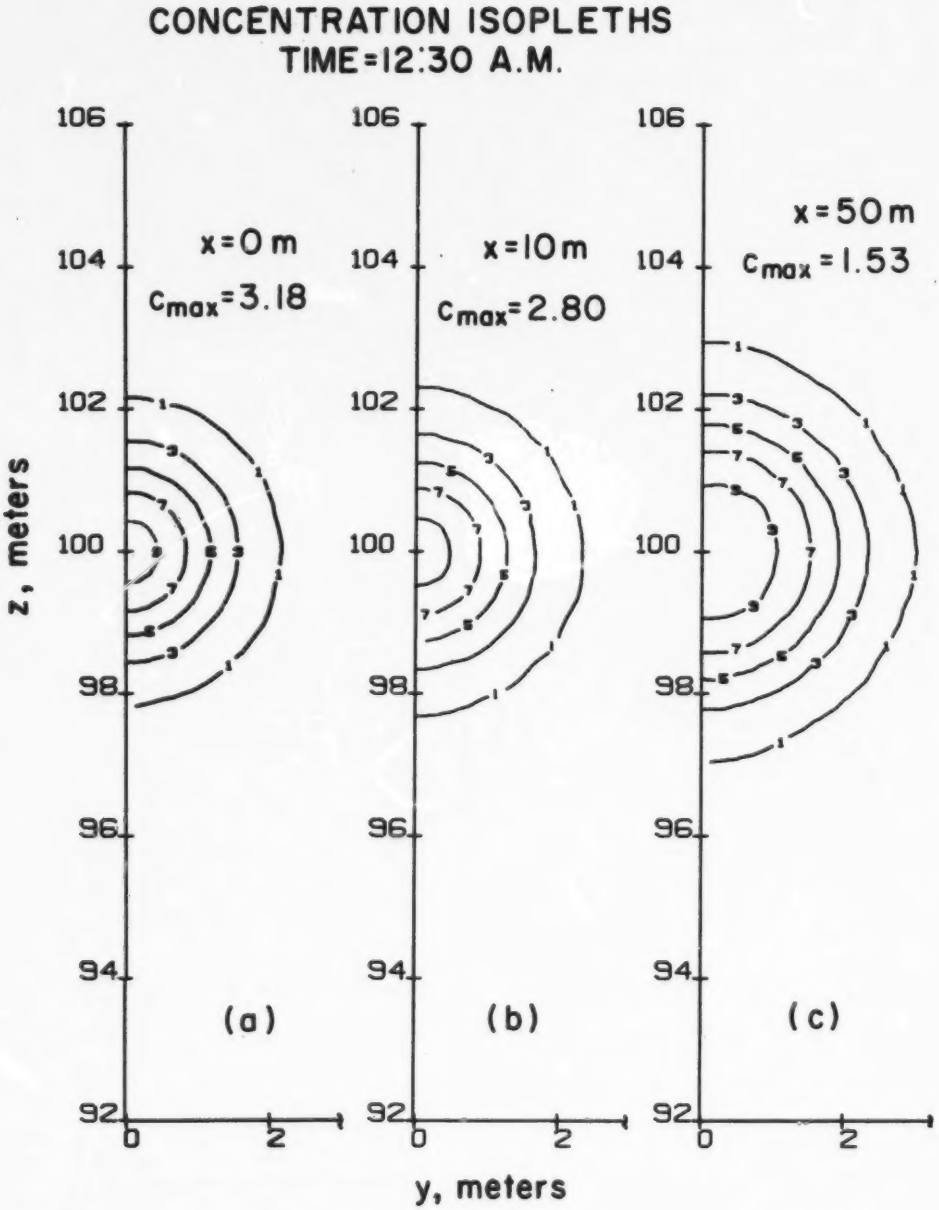

Figure 28: Contours of constant mean concentration at various distances downstream of a 100 m stack in a stable atmosphere. a) x = 0, b) x = 10 m, c) x = 50 m, d) x = 100 m, e) x = 250 m, f) x = 500 m, g) x = 5000 m, h) x = 10,000 m, i) x = 20,000 m.

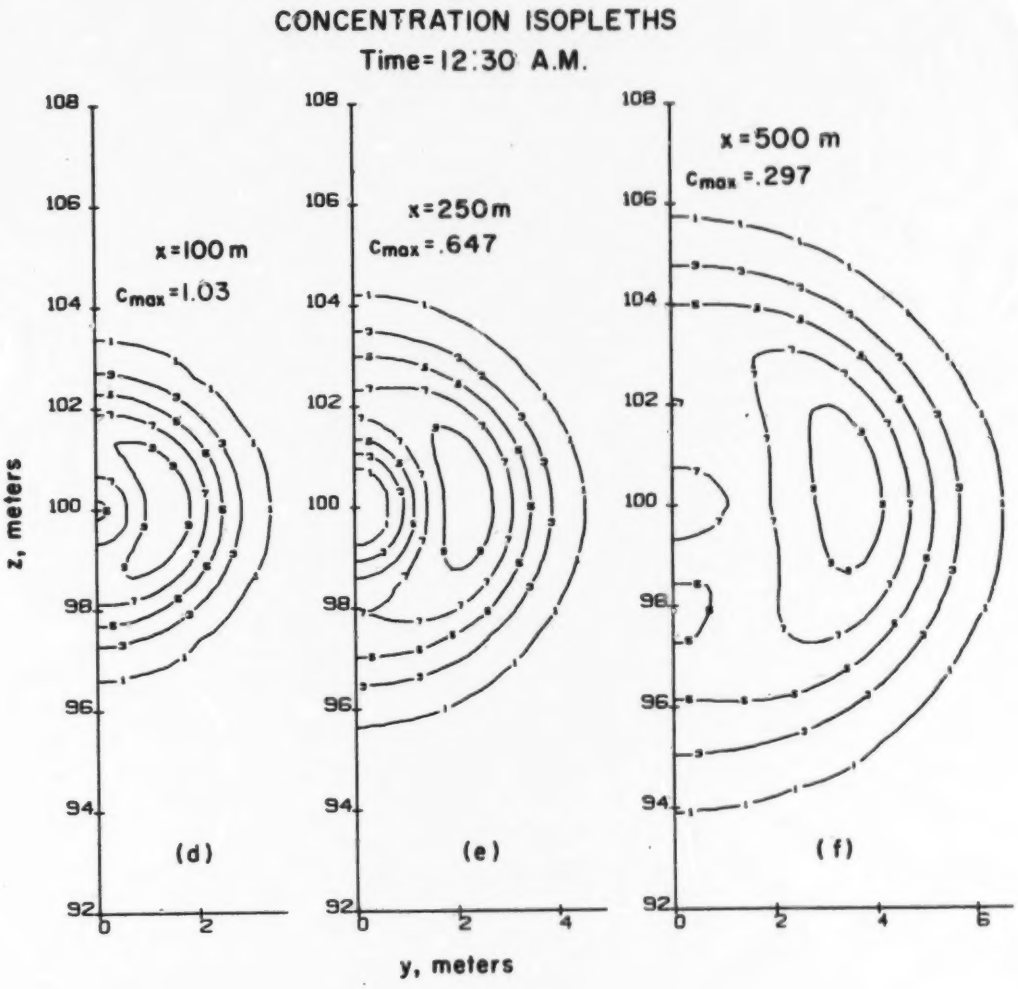

Figure 28: Continued

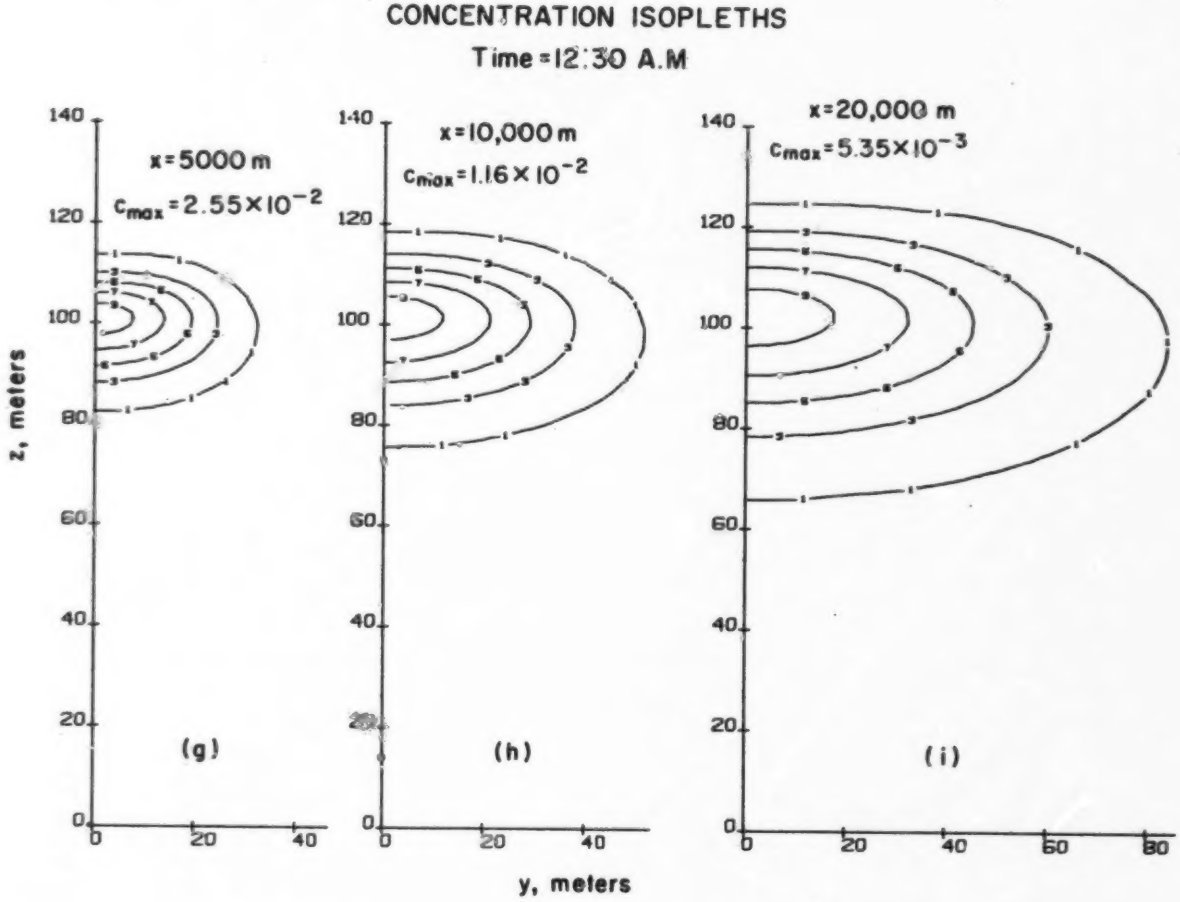

Figure 28: Continued

magnitude and the well-defined part of the plume has not reached the ground. The ground level concentration at this distance is roughly four orders of magnitude smaller than the local maximum concentration. Note that the stable plume spreads more horizontally than vertically while the reverse was true for the unstable plume. This is a direct result of the corresponding differences in the normal turbulence stresses $\overline{v'v'}$ and $\overline{w'w'}$, and qualitatively agrees with data[23,24].

Figure 29 shows the spatial plots of the contours of constant values of concentration fluctuation correlation. The fluctuations grow from their arbitrary initial values to a maximum between 50 and 100 meters and then decay. Near the end of the run the $\overline{C'C'}$ contours show much more distortion in height than do the C contours.

3 From Different Stack Heights

The effect of stack height on plume dispersion and ground level concentrations was investigated for stack heights of 25, 100, and 400 meters. The equilibrium turbulence field corresponded to the unstable conditions at 11:30 a.m. The turbulence profiles, initial conditions for the plume, and a detailed examination of the results for the 100 m stack were described in Section VI 5.1.

Figure 30 shows the maximum concentration decay for the three stack heights. Each of the curves exhibits the same general behavior including the two distinct kinks described earlier. The first kink, due to the plume meander, occurs slightly sooner for the higher stack because of the smaller Λ_p/Λ_t rates. The second kink, due to ground reflection, occurs considerably earlier for the shorter stack due to its proximity to the ground.

Figure 31 shows the ground level concentration history along the line running through the center of the stack. For the shorter stack, impingement ($C_{z=0} > 10^{-5}C_{max}$) occurs within 100 m of the stack. The impingement location for the taller stacks increases in direct proportion to the stack height. The concentration is a strong function of the stack height and is highest for the short stack for approximately 4 km. Beyond this point, the maximum concentration has reached the ground for the tallest stack and the ground level concentration becomes independent of the stack height.

Figure 32 shows the relationship between the maximum ground concentration and the stack height. It differs, although not very significantly, from the -2. power law dependence

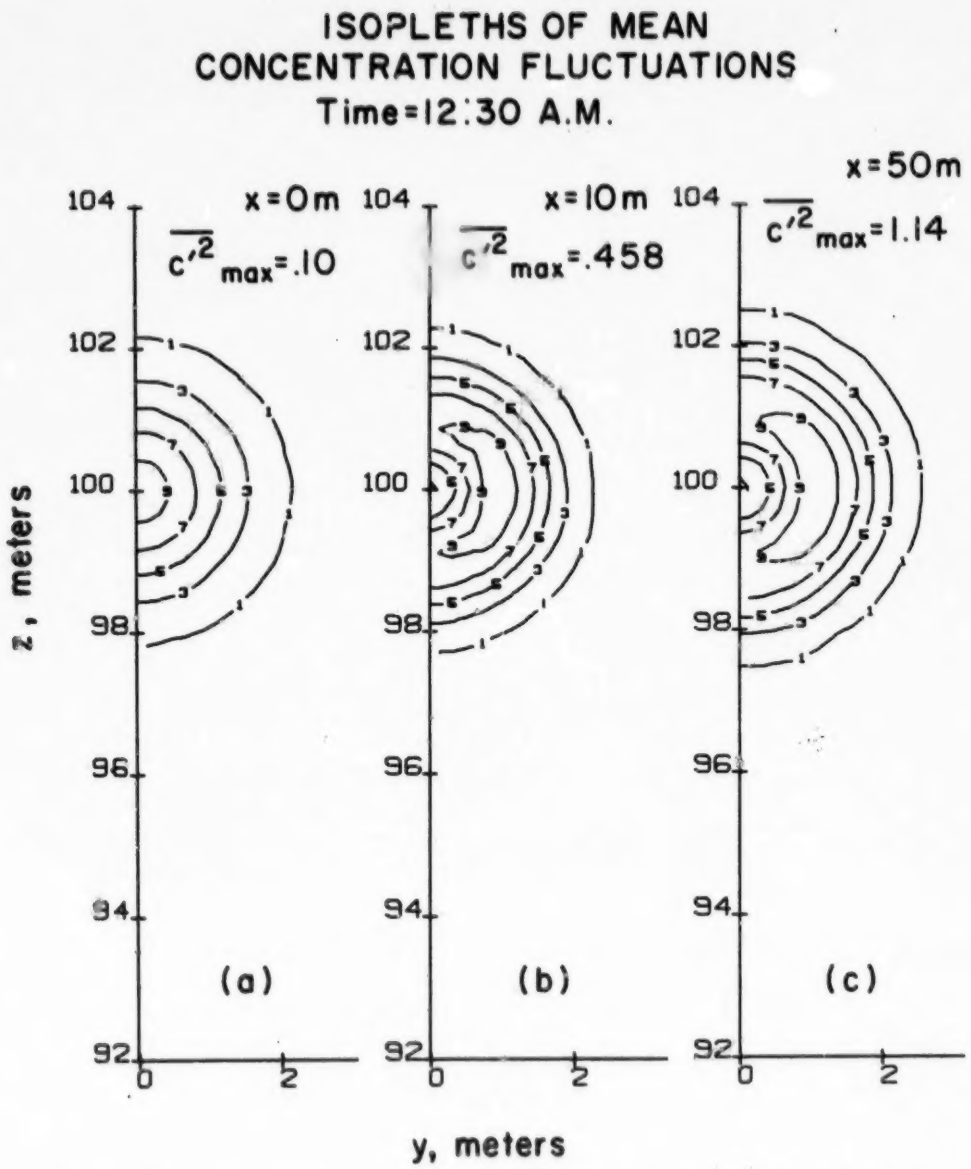

Figure 29: Contours of constant values of $\overline{C'C'}$ at the same x stations as given in fig. 28.

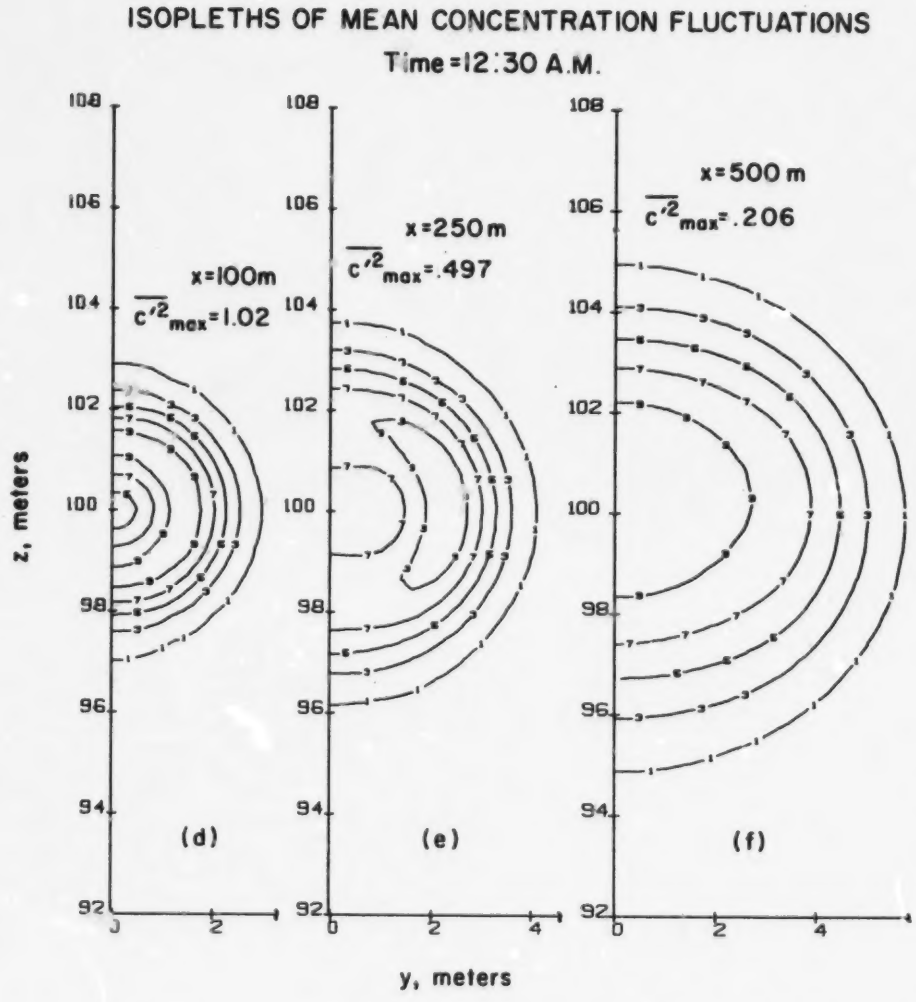

Figure 29: Continued

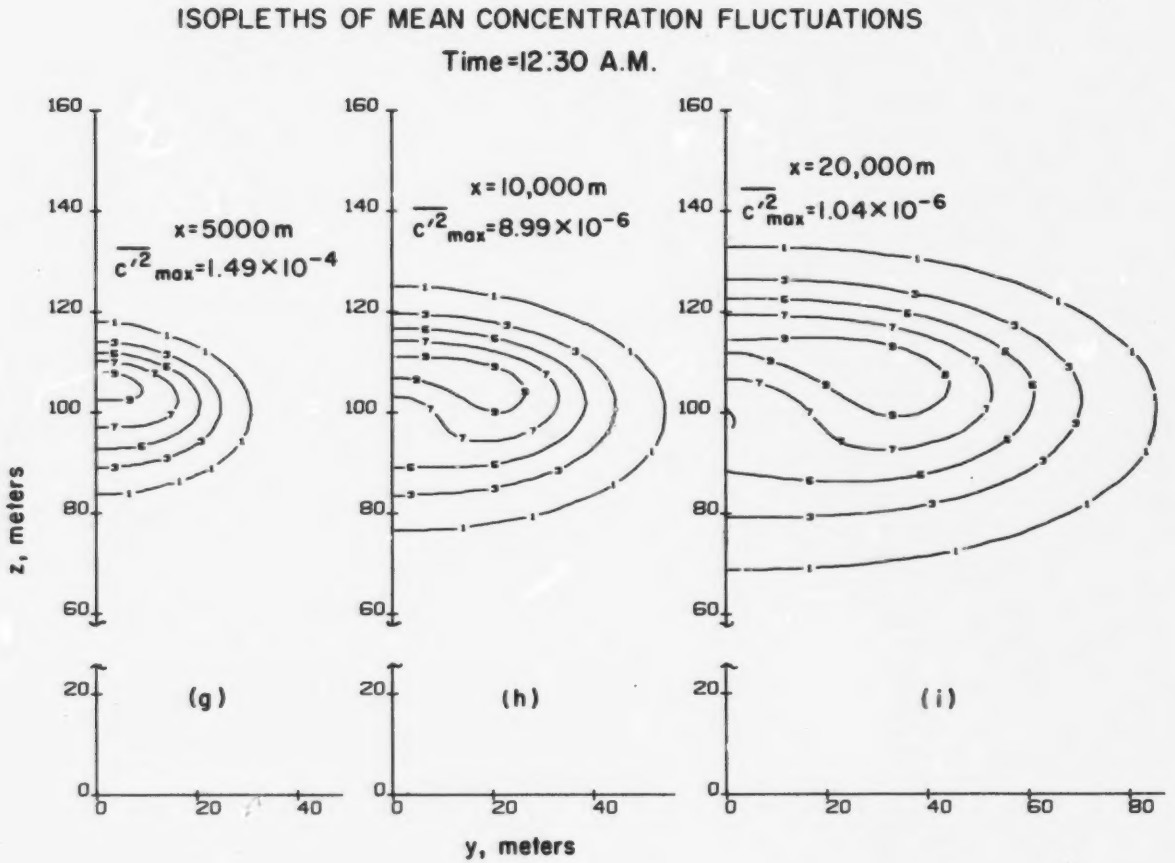

Figure 29: Continued

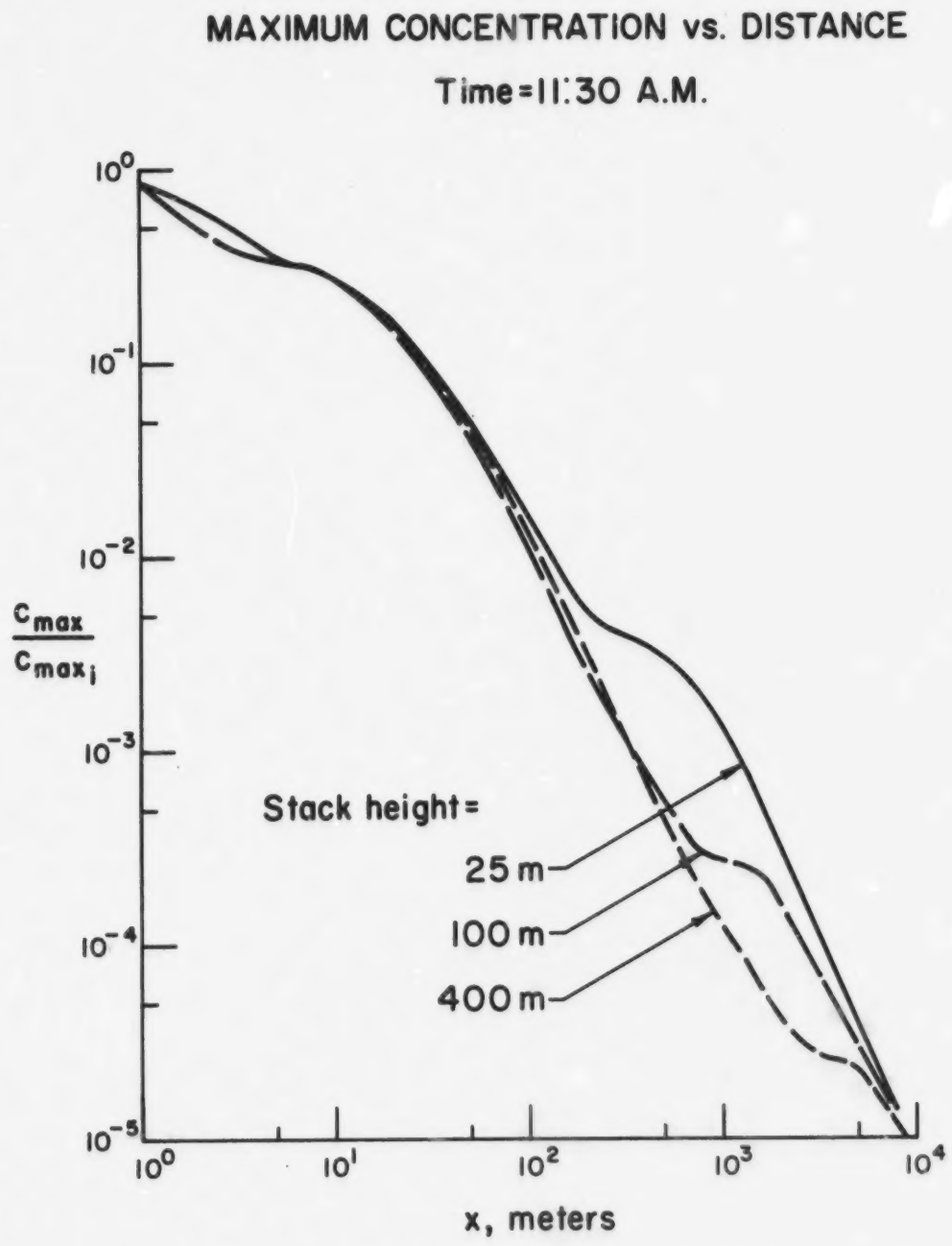

Figure 30: Decay of maximum concentration as a function of distance downwind of three different stack heights in an unstable atmosphere.

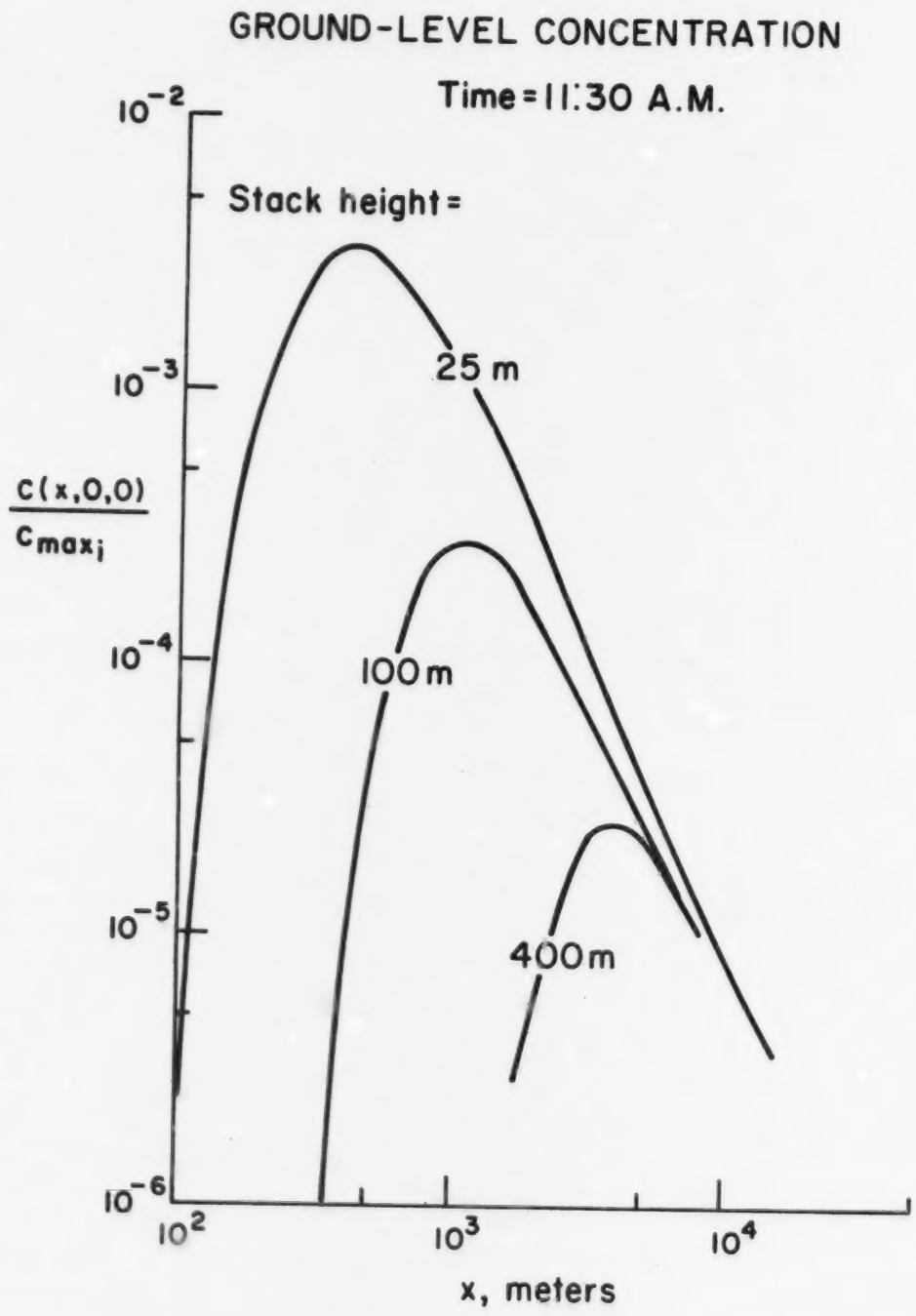

Figure 31: Ground level maximum mean concentration as a function of distance downwind of three different stack heights.

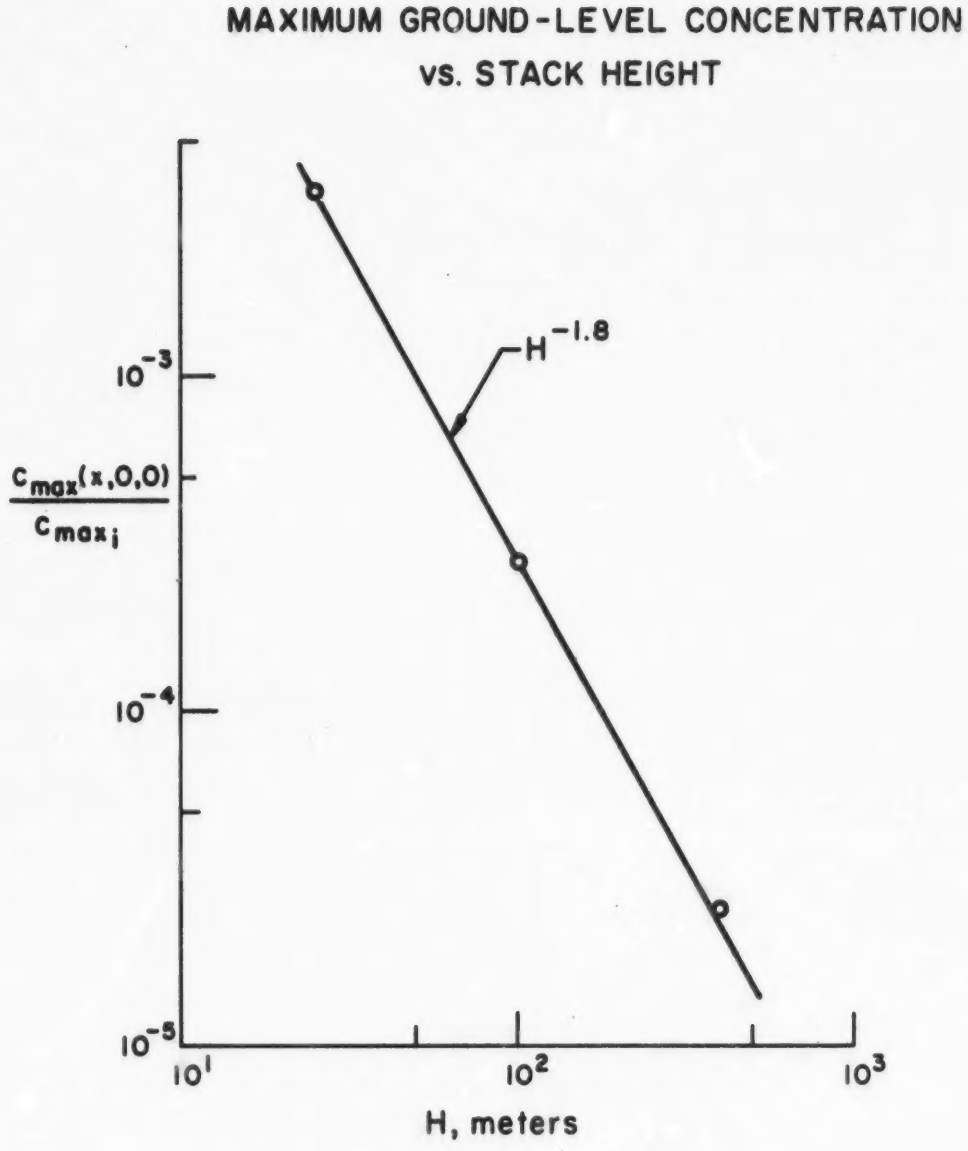

Figure 32: Maximum ground level mean concentration plotted as a function of effective stack height.

of maximum ground concentration of stack height, which is the dependence suggested by Sutton or Bosanquet and Pearson[23] for Gaussian plume dispersion. We expect this dependence of ground level concentration on stack height to vary as the vertical distribution of turbulence varies.

D.4 For Different Spatial Positions with Respect to A Suburban Community

In most cases, the areas surrounding pollutant sources contain numerous inhomogeneous surface features. As a first step towards incorporating such features in our model, we have coupled the pollutant dispersal model to two-dimensional spatial variation of the turbulence as described in Section V B. This gives us the capability of investigating plumes released at different spatial positions with respect to changes in meteorological surface conditions. Results of the calculations for two plumes are given in figs. 33 and 34. Both plumes are released at an altitude of 100 m with plume A released directly above the change in surface conditions and plume B released several km downwind of the surface transition point where the turbulence has reached equilibrium at the rougher surface conditions. The upwind value of z_o is .002 m corresponding to grass land, and the downwind value is .25 m corresponding to some type of suburban development. The atmospheric boundary layer is assumed to be neutral with the turbulence distributions as calculated in Section VI C.

In fig. 33, plume B shows the two features characteristic of the plumes in the previous sections - the meandering phase between 10 and 100 meters and the intersection of the plume with the ground at approximately 2 km. The meander phase is also evident in plume A but the intersection with the ground is masked by the changing field of turbulence. At a distance of 12 km downwind of the source, the maximum concentration in plume A is only 20% above that in plume B.

Ground level concentration isopleths for the two plumes are shown in fig. 34. The maximum difference in ground level concentration is only of the order of 30%. This difference would be decreased for larger stack heights and increased for lower stacks.

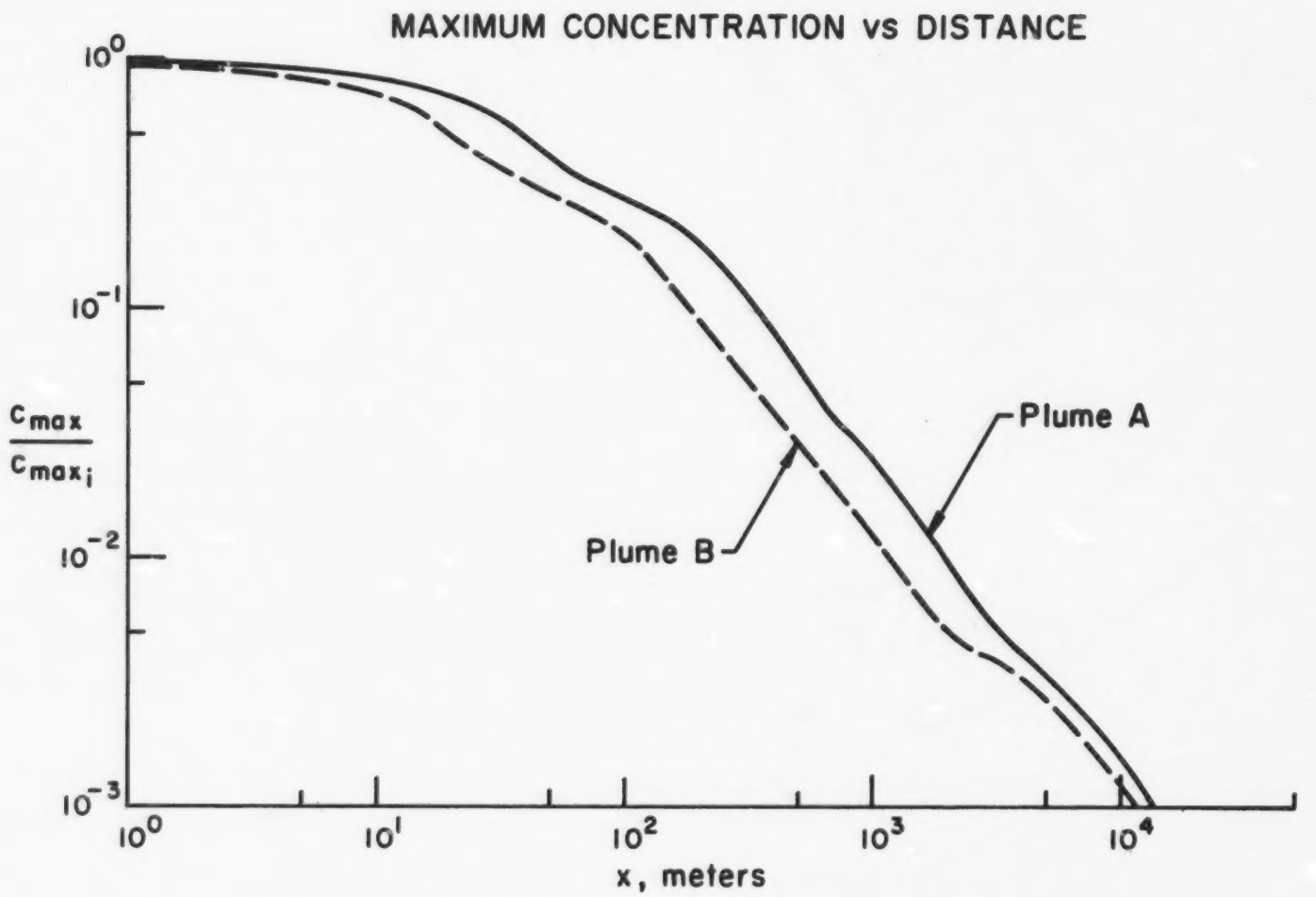

Figure 33: Decay of maximum concentration as a function of distance downwind of a 100 m stack in a neutral atmosphere. Plume A is released directly above an abrupt change in surface roughness (from z_o= .002 m to z_o= .25 m) and Plume B is released far downstream of the change in roughness.

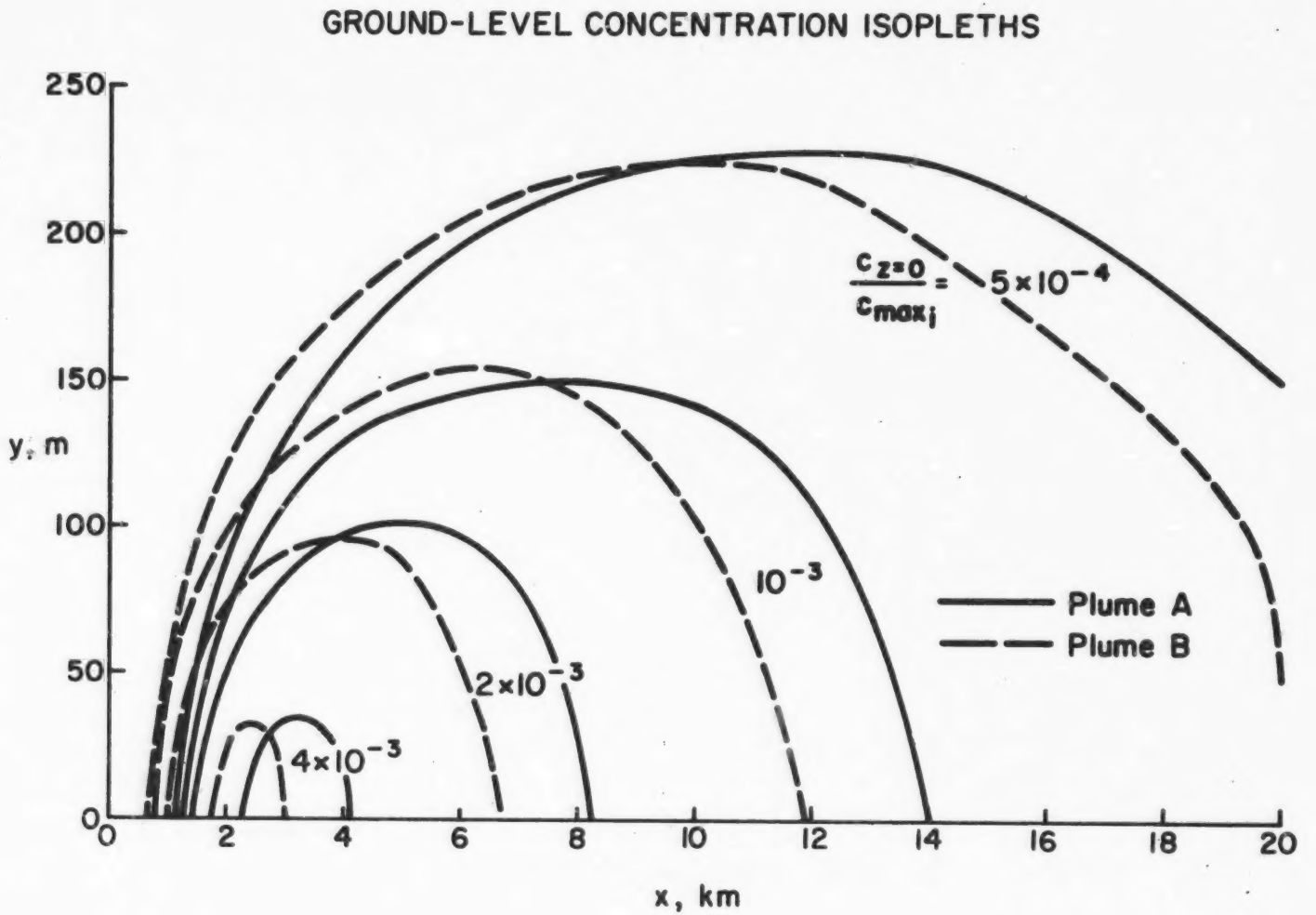

Figure 34: Ground level contours of mean concentration for Plumes A and B of fig. 33.

SECTION VII

REFERENCES

1. Donaldson, C. duP., "Atmospheric Turbulence and the Dispersal of Atmospheric Pollutants," EPA-R4-73-016a, March 1973.

2. Donaldson, C. duP., "Construction of a Dynamic Model of the Production of Atmospheric Turbulence and the Dispersal of Atmospheric Pollutants," American Meteorological Society Workshop in Micrometeorology, D. A. Haugen (ed.), Science Press, 1973 p. 313-390.

3. Lewellen, W. S. and M. Teske, "Prediction of the Monin-Obukhov Similarity Functions from an Invariant Model of Turbulence," J. of Atmos. Sci., 30, No. 7, pp. 1340-1345, 1973.

4. Lewellen, W. S., M. Teske and C. duP. Donaldson, "Application of Turbulence Model Equations to Axi-symmetric Wakes," AIAA J., 12, No. 5, pp. 620-625, May 1974.

5. Lumley J. L. and B. Khajeh-Nouri, "Computational Modeling of Turbulent Transport," (to be published in the Proceedings of the Second IUTAM-IUGG Symposium on Turbulent Diffusion in Environmental Pollution.)

6. Rodi, W., "The Prediction of Free Turbulent Boundary Layers by Use of a Two-Equation Model of Turbulence," Dissertation submitted to Mechanical Eng. Dept., Imperial College, London, Dec. 1972.

7. Daly, B. J. and F. H. Harlow, "Transport Equations in Turbulence," The Physics of Fluids, 13, pp. 2634-2649, Nov. 1970.

8. Bradshaw, P., "The Understanding and Prediction of Turbulent Flows," Aeronautical J., pp. 403-418, 1972.

9. Mellor, G. L. and H. J. Herring, "A Survey of Mean Turbulent Field Closure Models," AIAA J. pp. 590-599, May 1973.

10. Gad-el-Hak, M. and S. Corrsin, "Measurements of the Nearly Isotropic Turbulence Behind a Uniform Jet Grid," J. Fluid Mechanics, 62, pp. 115-143, 1974.

11. Lewellen, W. S., M. Teske and C. duP. Donaldson, "Turbulence Model of Diurnal Variations in the Planetary Boundary Layer," Proceedings of the 1974 Heat Transfer and Fluid Mechanics Institute, L. R. Davis and R. E. Wilson (eds.), Stanford U. Press, 1974 (included as an Appendix).

12. Lewellen, W. S., M. Teske and C. duP. Donaldson, "Second-Order, Turbulent Modeling Applied to Momentumless Wakes in Stratified Fluids," A.R.A.P. Report No. 206, 47 p., Nov. 1973.

13. Monin, A. S. and A. M. Yaglom, Statistical Fluid Mechanics, MIT Press, 1971.

14. Roache, P. J., Computational Fluid Dynamics, Hermosa Publishers, Albuquerque, N. M., 87108, 1972.

15. Deardorff, J. W., "Numerical Investigation of Neutral and Unstable Planetary Boundary Layers," J. Atmos. Sci., 29, pp. 91-115, 1972.

16. Panofsky, H. A., "The Atmospheric Boundary Layer Below 150 Meters," Annual Reviews of Fluid Mechanics, 6, pp. 147-178, 1974.

17. Wyngaard, J. C., "Notes on Surface Layer Turbulence," American Meteorological Society Workshop in Micrometeorology, D. A. Haugen (ed.), Science Press, 1973.

18. Bradley, E. F., "A Micrometeorological Study of Velocity Profiles and Surface Drag in the Region Modified by a Change in Surface Roughness," Quarterly J. of the Roy. Meteorological Soc., 94, pp. 361-379, 1968.

19. Shir, C. C., "A Numerical Computation of Air Flow Over a Sudden Change in Surface Roughness," J. Atmos. Sci., 29, pp. 304-310, 1972.

20. Schlichting, H., Boundary Layer Theory, McGraw Hill (6th edition), 1968.

21. Turner, D. B., Workshop of Atmospheric Dispersion Estimates, Office of Air Programs Publication No. AP-26, Environmental Protection Agency (5th printing), March 1972.

22. Wasko, P. E. and H. Moses, "Atmospheric Diffusion Studies," Argonne National Lab. Rept. No. 6049, 1959.

23. Pasquill, F. Atmospheric Diffusion, D. Van Nostrand Co., Ltd., 1962.

24. Hilst, G. R. and C. L. Simpson, "Observations of Vertical Diffusion Rates in Stable Atmospheres," J. of Meteorology, Vol. 15, pp. 125-126, February 1958.

SECTION VIII

NOMENCLATURE

A_1, a, b	model constants
C	species concentration
f	Coriolis parameter = $2\Omega \sin \phi$
g	gravitational acceleration
k	von Karman's constant = $u^*/(z \frac{\partial u}{\partial z})_o$ in the neutral surface layer
ℓ	proportionality constant in eq. (44)
L	Monin-Obukhov length = $- u^{*3} T_o / kg(\overline{w'\theta'})_o$
n	decay rate for grid turbulence
p	mean pressure
q	square root of twice the turbulent kinetic energy
$\dot{Q}$	heat source per unit mass
s	model constant
$s_{0,1,2,3}$ ---	constants in scale equation
T	temperature
u	mean velocity component in the direction of the geostrophic wind or the surface wind
u_i, u_j, u_k	Cartesian velocity components
u^*	surface shear stress velocity = $[\tau/\rho]^{\frac{1}{2}}$

v	mean horizontal velocity component normal to either the geostrophic wind or the surface wind
V_c	model constant
w	mean vertical velocity component
x_i, x_j, x_k	Cartesian coordinates
z	vertical coordinate
z_o	surface roughness height
α	constant slope of Λ near $z=0$; or angle to which the surface wind is rotated from the geostrophic wind direction
β	proportionality constant in eq. (52)
δ_{ij}	Kronecker delta
δ_T	height at which the turbulent energy falls to 1/4 its maximum value
ϵ	dissipation function
ϵ_{ijk}	alternating tensor
θ	potential temperature referenced to T_o
κ	coefficient of laminar diffusion for the potential temperature
Λ	macroscale of turbulent model
λ	microscale of turbulent dissipation = $\Lambda/(a + bq\Lambda/\nu)^{\frac{1}{2}}$
ν	kinematic viscosity
ρ	density
σ	standard deviation of plume
τ	surface shear stress

ϕ	latitude
ψ	stream function
Ω	earth's rotation, $\Omega_1 = \Omega(0, \cos\phi, \sin\phi)$

Superscripts

$\overline{\quad}$	denotes ensemble average
'	denotes fluctuation about the mean

Subscripts

o	denotes value at $z=z_o$
g	denotes geostrophic wind
i	initial condition
p	denotes plume value
t	denotes turbulence value

APPENDIX

TURBULENCE MODEL OF DIURNAL VARIATIONS IN THE PLANETARY BOUNDARY LAYER

W. S. Lewellen,* M. Teske,** and Coleman duP. Donaldson†

ABSTRACT

The dynamics of momentum and heat transfer in the atmospheric boundary layer is analyzed using an invariant modeling technique to provide second-order closure of the Reynolds stress equations. Spatially homogeneous boundary conditions are applied at the top of the boundary layer and at the surface where the heat flux is assumed to be cyclic in time approximating conditions over the Midwestern plains in the summer. Numerical results of the model show favorable comparison with field observations. Although the contribution of the time derivative term is small in the turbulence equations, there remains significant unsteady influences on the dynamics of the boundary layer through the relatively slow response of the mean velocities.

INTRODUCTION

One of the heat transfer and fluid mechanics problems of most direct concern to all of us is that of the atmospheric boundary layer. A better means of quantitatively predicting the dynamics of turbulent convection of heat, momentum and mass within this layer could be very beneficial. It would provide the basis for the prediction of when and to what degree air quality will be affected by the release of contaminants at given points; increase the accuracy of weather forecasting by more correctly accounting for air-surface interactions; make possible the prediction of local low-level winds around such places as airports; and perhaps even give engineers the capability of designing the arrangement of buildings, trees, and terrain features in such a way as to optimize the transfer of heat to and from the surroundings.

Classical methods of dealing with the dynamics of the planetary boundary layer [1] involve the assumption of some type of eddy viscosity relationships to determine turbulent transport. These methods have proved useful, but lack the flexibility of providing a consistent means for accurately predicting the eddy viscosity variation under untested conditions. At the other extreme, there is the sophisticated integration of the unsteady equations of motion for all of the turbulent fluctuations above a prescribed grid size [2]. These results can then be averaged to obtain mean velocities and turbulent flux transports. This approach has the capability of providing accurate results when proper care is paid to the inclusion of appropriate subgrid scale turbulent transport,

* Senior Consultant, Aeronautical Research Associates of Princeton, Inc., Princeton, New Jersey 08540 (A.R.A.P.)

** Senior Staff, A.R.A.P.

† President and Senior Consultant, A.R.A.P.

Reprinted from PROCEEDINGS 1974 HEAT TRANSFER, Japan Society of Mechanical Engineers, Tokyo, Japan, Sept. 3-7, 1974.

Copyright © 1974 by the Board of Trustees of the Leland Stanford Junior University.

but the computer requirements are too demanding for routine use. Simulation of a 24-hour day over an area of 5 x 5 km to a height of 2 km with 64,000 grid points recently required 350 hours of computing time on the CDC 7600 at NCAR [3].

Our approach lies between the above extremes, in using invariant modeling techniques to provide second-order closure of the Reynolds stress equations. Details of this approach have been given by Donaldson [4]. The basic assumption is that the dependence of the third-order correlations of the velocity fluctuations on the second-order correlations, the mean flow properties, and their derivatives, is invariant with respect to changes in the flow geometry. This permits data from relatively simple flow experiments to be used in evaluating the necessary coefficients in the modeled terms. Several other investigators are using similar approaches for turbulent flow problems [5-7]. Wyngaard, Coté and Rao [8] and Shir [9] have modeled the planetary boundary layer using this type of approach, but have published only steady state results.

We consider the atmospheric boundary layer for a region of the earth where the surface boundary conditions are homogeneous so that the flow is a function of time and altitude only. The upper boundary condition is assumed to be known, with the dynamics of the diurnal motion setting the altitude at which the condition is applied. The given geostrophic wind and upper level temperature lapse rate are constant. Time variation is provided by letting the surface heat flux be cyclic at conditions approximating those over the Midwestern plains during the summer [10].

The results compare favorably with field observations and demonstrate that there is significant lag in the dynamics of the layer behind the changing surface conditions, so that for the same stability conditions the wind angle is higher and the surface shear stress lower if the surface heat flux is increasing rather than decreasing. The significant difference at neutral conditions may explain much of the scatter in field observations.

DESCRIPTION OF THE MODEL

For homogeneous boundary conditions at the surface and at the top of the boundary layer, the equations of motion for the mean horizontal velocity within the boundary layer may be written as

$$\frac{\partial u}{\partial t} = v(2\Omega \sin \phi) - \frac{\partial \overline{u'w'}}{\partial z} + \nu \frac{\partial^2 u}{\partial z^2} \qquad (1)$$

$$\frac{\partial v}{\partial t} = (u_g - u)\, 2\Omega \sin \phi - \frac{\partial \overline{v'w'}}{\partial z} + \nu \frac{\partial^2 v}{\partial z^2} \qquad (2)$$

and the mean energy equation as

$$\frac{\partial \theta}{\partial t} = - \frac{\partial \overline{w'\theta'}}{\partial z} - \dot{Q}_R + \kappa \frac{\partial^2 \theta}{\partial z^2} \tag{3}$$

We have included the laminar diffusion terms in these equations (although they are certainly negligible over almost all of the region) because they cause no numerical difficulty and permit the solutions to be checked against the analytic Ekman spiral. Even with the radiation energy source $\dot{Q}_R$ prescribed, these solutions are not determined until the turbulent transport terms $\overline{u'w'}$, $\overline{v'w'}$, and $\overline{w'\theta'}$ are determined.

When the Boussinesq approximation is used, the Reynolds equations for these transport terms may be written as

$$\begin{aligned}\frac{D\overline{u_i'u_j'}}{Dt} = &- \overline{u_i'u_k'} \frac{\partial u_j}{\partial x_k} - \overline{u_j'u_k'} \frac{\partial u_i}{\partial x_k} + \frac{g_i}{T_o} \overline{u_j'\theta'} + \frac{g_j \overline{u_i'\theta'}}{T_o} \\ &- \frac{\partial}{\partial x_k} (\overline{u_k'u_i'u_j'}) - \frac{1}{\rho} \frac{\partial \overline{p'u_i'}}{\partial x_j} - \frac{1}{\rho} \frac{\partial \overline{p'u_j'}}{\partial x_i} \\ &+ \overline{\frac{p'}{\rho} \left(\frac{\partial u_i'}{\partial x_j} + \frac{\partial u_j'}{\partial x_i}\right)} + \nu \frac{\partial^2 \overline{u_i'u_j'}}{\partial x_k^2} - 2\nu \overline{\frac{\partial u_i'}{\partial x_k} \frac{\partial u_j'}{\partial x_k}} \\ &- 2\epsilon_{ik\ell} \Omega_k \overline{u_\ell'u_j'} - 2\epsilon_{j\ell k} \Omega_\ell \overline{u_k'u_i'}\end{aligned} \tag{4}$$

$$\begin{aligned}\frac{D\overline{u_i'\theta'}}{Dt} = &- \overline{u_i'u_j'} \frac{\partial \theta}{\partial x_j} - \overline{\theta'u_j'} \frac{\partial u_i}{\partial x_j} - \frac{\partial (\overline{\theta'u_i'u_j'})}{\partial x_j} - \frac{1}{\rho} \frac{\partial}{\partial x_i} (\overline{p'\theta'}) \\ &+ \overline{\frac{p'}{\rho} \frac{\partial \theta'}{\partial x_i}} + \overline{\theta'^2} \frac{g_i}{T_o} - \nu\theta' \overline{\frac{\partial^2 u_i'}{\partial x_j^2}} - \kappa u_i' \overline{\frac{\partial^2 \theta'}{\partial x_j^2}} \\ &- 2\epsilon_{ijk} \Omega_j \overline{u_k'\theta'}\end{aligned} \tag{5}$$

$$\frac{D\overline{\theta'^2}}{Dt} = - 2\overline{u_j'\theta'} \frac{\partial \theta}{\partial x_j} - \frac{\partial}{\partial x_j} \overline{u_j'\theta'^2} + \kappa \frac{\partial^2 \overline{\theta'^2}}{\partial x_j^2} - 2\kappa \overline{\frac{\partial \theta'}{\partial x_j} \frac{\partial \theta'}{\partial x_j}} \tag{6}$$

To close the system of equations at this order we must model the third-order correlations in terms of the lower-order correlations. For a discussion of the various methods that have been suggested for this purpose we refer the reader to Refs. [4-7]. We have attempted to choose the simplest models consistent with certain critical experiments. The models we currently use are

$$\frac{\partial}{\partial x_k}\left(\overline{u_i' u_j' u_k'}\right) + \frac{1}{\rho}\frac{\partial \overline{p' u_i'}}{\partial x_j} + \frac{1}{\rho}\frac{\partial \overline{p' u_j'}}{\partial x_i} = -V_c \frac{\partial}{\partial x_k} q\Lambda \frac{\partial \overline{u_i' u_j'}}{\partial x_k} \tag{7}$$

$$\overline{\frac{p'}{\rho}\left(\frac{\partial u_i'}{\partial x_j} + \frac{\partial u_j'}{\partial x_i}\right)} = -\frac{q}{\Lambda}\left(\overline{u_i' u_j'} - \frac{\delta_{ij} q^2}{3}\right) \tag{8}$$

$$\overline{\frac{\partial u_i'}{\partial x_k}\frac{\partial u_j'}{\partial x_k}} = \frac{\delta_{ij} q^2}{3\lambda^2} + \frac{a}{\Lambda^2}\left(\overline{u_i' u_j'} - \frac{\delta_{ij} q^2}{3}\right) \tag{9}$$

$$\overline{\frac{\partial \theta'}{\partial x_i}\frac{\partial \theta'}{\partial x_i}} = s\frac{\overline{\theta'^2}}{\lambda^2} \tag{10}$$

$$\overline{\frac{p'}{\rho}\frac{\partial \theta'}{\partial x_i}} = -\frac{A_1 q}{\Lambda}\overline{u_i' \theta'} \tag{11}$$

with $\lambda^2 = \Lambda^2/(a + bq\Lambda/\nu)$. This gives five coefficients to be determined by critical experiments and one of these, a (set = 2.5), is unimportant in high Reynolds number flows.

The coefficient in the dissipation term, b, may be determined to be 1/8 by equating the dissipation terms to the production terms in the constant stress wall layer of a boundary layer. The diffusion coefficient V_c is set equal to 0.3 by comparing model results with axisymmetric jets and wakes [11]. The most uncertainty in the present model is probably introduced in the evaluation of the scale Λ. Other researchers have used a dynamic equation for the scale, such as is obtained from modeling the dynamic equation for the dissipation function. Although the form of the equation used by different people is similar, there is no general agreement on the values of the coefficients introduced in the equation. In fact, there is some evidence that different values are required for different flow geometries. Since this would violate our basic assumption of invariancy, we have not yet incorporated a dynamic scale equation into our model. We are, however, currently seeking an equation that will be invariant to changes in the flow geometry. Until such time as we achieve this, we are using an algebraic relationship for Λ. Three limits are imposed to define it in the atmospheric boundary layer

$$\text{i)} \quad \Lambda \leq 0.6z \tag{12-a}$$

$$\text{ii)} \quad \Lambda \leq 0.15\ \delta_T \tag{12-b}$$

and in either the neighborhood of the upper level inversion layer or in the surface layer

$$\text{iii)} \quad \Lambda \leq 0.5\ q \sqrt{\frac{T_o}{g\partial\theta/\partial z}} \tag{12-c}$$

The first two of these limits come from comparison with laboratory boundary layer flows, while the last recognizes that there is a limit on the size of an eddy with a fixed energy which can overcome a given gravitational force.

The remaining coefficients A_1 and s were determined by comparison with measurements in the atmospheric surface layer [12]. Near the surface the turbulence equilibrates rapidly to the changing surface conditions and the flow may be considered steady so that Eqs. (1)-(3) reduce to the condition that the shear stress and heat flux be independent of the height. In this constant flux layer Eqs. (4) and (6) with the modeled terms from Eqs. (7) to (11) lead to a set of ordinary differential equations as a function of the single dimensionless variable, the height z normalized by the Monin-Obukhov scale length L. Figure 1 gives the resulting dimensionless velocity and temperature gradients as a function of the Monin-Obukhov variable for our chosen values of $A_1 = 0.75$ and $s = 1.8$. The parameter A_1 was chosen to make the temperature gradient agree with observations as $z \to 0$ and s was chosen so that the temperature variance was properly scaled. Comparisons of the variables $\overline{w'w'}$, $\overline{u'\theta'}$ and $\overline{\theta'\theta'}$ with observations are given in Ref. [12]. All the comparisons are quite favorable.

With the turbulence model set we turn to the specification of the boundary conditions for the planetary boundary layer calculation. The surface heat flux variation assumed (Fig. 2) is that obtained by averaging over 3 weeks of data gathering in Kansas [10]. Between sunset and sunrise the heat flux is a negative constant (heat flows from the atmosphere to the ground). Between approximately 8:00 a.m. and 8:00 p.m. the heat flux is positive and nearly follows a sine wave. Over the 24-hour cycle there is a net positive heat flux to the atmosphere which must be removed (in simulation of long wave radiation) if there is to be no long term heating of the boundary layer. In the present model this is accomplished by assuming Q_R uniformly distributed in time and space between the ground and the initial inversion altitude of 2 km.

The lower boundary condition is applied at a reference level z_r which must be much less than the absolute value of the Monin-Obukhov length. At $z = z_r$ we require that

$$\frac{\partial u}{\partial z} = u/[z\ \ell n(z/z_o)]$$

$$\frac{\partial v}{\partial z} = v/[z\ \ell n(z/z_o)]$$

$$\frac{\partial \theta}{\partial z} = -5.4\left(\frac{\overline{w'\theta'}\ \ell n\ z/z_o}{z(u^2+v^2)^{\frac{1}{2}}}\right)$$

$$q^2 = 5.77\left(\frac{u^2+v^2}{(\ell n\ z/z_o)^2}\right) \qquad (13)$$

with the roughness height, z_o, held constant (= 0.008 meters). The two numbers in these expressions come from matching to the neutral surface layer.

The altitude of the top of the boundary layer is controlled by the motion dynamics. As $z \to \infty$ we require that

$$u \to u_g = 10 \text{ m/sec}$$

$$v \to v_g = 0$$

$$q^2 \to 0$$

$$\theta \to \begin{cases} 0.007\ (z - 2\text{ km})\ ^\circ\text{C} & z > 2\text{ km} \\ 0\ ^\circ\text{C} & z < 2\text{ km} \end{cases} \qquad (14)$$

The steady state neutral boundary layer for our initial conditions has a height of approximately 1.6 km. We have permitted the boundary layer to grow somewhat larger than this before it is affected by the upper level inversion. If the upper level inversion were completely removed, the unstable boundary layer in the afternoon would grow unboundedly.

Calculations are started at equilibrium neutral conditions and allowed to proceed for three complete 24-hour cycles. Results for the second and third days are very nearly identical.

Two simplifications to the system of partial differential equations have been made to expedite numerical computations. First, the terms involving the Coriolis parameter are ignored in the second-order correlation equations. In addition to the algebraic simplification offered, this approximation also allows $2\Omega \sin \phi$ to be treated as a single parameter; and, an a posteriori check of the results shows that $4\Omega\Lambda/q$ rarely exceeds 0.1 in the time and space domain considered, and over most of the domain is much less than this so that inclusion of the terms would have very little effect on the numerical solutions. (This is also borne out by Shir's computations [9].) The other approximation has more influence on the accuracy of the results. It is to assume that the turbulence is in quasi-equilibrium so that the relationships between

all of the second-order correlations are obtained by dropping the time derivatives and the diffusion terms in Eqs. (4)-(6) to yield

$$\overline{u_i'u_j'} = \delta_{ij}\frac{q^2}{3}[1 - 2(b - c)]$$

$$- \frac{\Lambda}{q}\left[\overline{u_i'w'}\frac{\partial u_j}{\partial z} + \overline{u_j'w'}\frac{\partial u_i}{\partial z} - \delta_{3i}g\frac{\overline{u_j'\theta'}}{T_o} - \delta_{3j}g\frac{\overline{u_i'\theta'}}{T_o}\right] \quad (15)$$

$$\overline{u_i'\theta'} = -\frac{\Lambda}{A_1 q}\left(\overline{u_i'w'}\frac{\partial\theta}{\partial z} + \overline{w'\theta'}\frac{\partial u_i}{\partial z} - \delta_{3i}g\frac{\overline{\theta'^2}}{T_o}\right) \quad (16)$$

$$\overline{\theta'^2} = -\frac{\Lambda}{sbq}\overline{w'\theta'}\frac{\partial\theta}{\partial z} \quad (17)$$

where the function c(t,z) has been added to allow the equation for q^2 to be carried in full

$$\frac{\partial q^2}{\partial t} = -2\overline{u'w'}\frac{\partial u}{\partial z} - 2\overline{v'w'}\frac{\partial v}{\partial z} + \frac{2g}{T_o}\overline{w'\theta'}$$

$$+ \frac{\partial}{\partial z}\left(V_c q\Lambda\frac{\partial q^2}{\partial z}\right) + \nu\left(\frac{\partial^2 q^2}{\partial z^2} - \frac{2q^2}{\lambda^2}\right) \quad . \quad (18)$$

Comparison of the results of this type of quasi-equilibrium approximation with results of integration of the full equations for other problems suggests that the difference is of the order of 10% or less in the diurnal day calculation. In fact, an a posteriori check of the present calculation shows that $(\Lambda/q\ \overline{u'w'})(\partial\overline{u'w'}/\partial t)$ and $(\Lambda/A_1 q\ \overline{w'\theta'})(\partial\overline{w'\theta'}/\partial t)$ are only of the order of 5% at z = 1 km and t = 12 hrs. where q^2 is undergoing its most rapid changes. The simplification of reducing 9 of our 13 differential equations to algebraic expressions appears to justify accepting a slight loss in solution accuracy. With these simplifications, the computation of a day's variation in the boundary layer (using the implicit tridiagonal algorithm [11]) requires 45 minutes on Digital Scientific's Meta 4 computer. Equivalent time on a CDC 6600 would be 3 minutes.

Height variation of the velocity and turbulent kinetic energy for the neutral, steady-state boundary layer predicted by our model is given in Fig. 3. The distributions closely resemble those obtained by scaling Deardorff's results [13] to match the same boundary conditions. The value of the surface drag coefficient falls well within the scatter of field data for the same value of Ro. The q at the surface is 14% lower than Deardorff's result. A large part of this discrepancy occurs in the $\overline{v'v'}$ component and may indicate the need for some refinement of our model coefficients. It also appears that the accuracy of Deardorff's result may be affected by his choice of too low a height for the boundary layer.

RESULTS FOR A TYPICAL DAY CALCULATION

The space and time variations of the turbulent kinetic energy is given in Fig. 4. The boundary layer thickness grows during the day and shrinks during the night. The turbulent kinetic energy reaches a maximum of 5% of the geostrophic mean kinetic energy in midafternoon at an altitude of approximately 700 meters. As the sun sets, the turbulence decays until at midnight, the maximum turbulent kinetic energy is only 0.1% of the mean kinetic energy and is restricted to the lowest 100 m altitude. The most rapid changes in turbulent energy occur around noon in the neighborhood of 1 km with the buildup in turbulent kinetic energy much more rapid than the decay in late afternoon. However, in either case the turbulence does not appear to be far out of equilibrium, with $\partial q^2/\partial t$ smaller than the dissipation term $2bq^3/\Lambda$. This tends to substantiate our quasi-equilibrium approximation, although a detailed validation of the approximation must await a calculation using the full set of equations.

Space and time variations of velocity and temperature are given in Figs. 5 through 7. Several realistic features may be observed. There is a distinct low-level nocturnal jet evidenced in Fig. 5. This wind in excess of the geostrophic value could be predicted for a planetary boundary layer in steady-state equilibrium under stable conditions. Integration of Eq. (2) with respect to z under steady conditions shows that the overshoot must exist as long as $\overline{v'w'} \leq 0$ at the surface as it will be for $\sigma > 0$. Velocity shear is principally concentrated in two layers, one at the surface and a second at the bottom of the upper inversion layer. This upper level shear zone moves up in the afternoon and back down in the early morning. The contours of potential temperature in Fig. 7 also show that the boundary layer is rather uniformly mixed between approximately 200 m and 2 km, even when this region is above the majority of the turbulence as it is in the late night and early morning hours. Note also that there is a very clear nocturnal, low-level inversion in the temperature.

Contours of turbulent length scale are given in Fig. 8. Although Λ has been set equal to its lowest upper bound everywhere as defined by Eq. (12), the time rate of change of the scale nowhere exceeds q. Thus, the dynamics of the scale appear reasonable although a dynamic equation for it has not been used. This is plausible because of the near local equilibrium of the turbulence everywhere.

Surface shear stress and wind angle are plotted in Figs. 9 and 10. There is a relatively low surface shear stress and large wind angle at night and conversely large shear stress and small wind angle in the afternoon. Thus, in the early morning hours the wind shifts dramatically with altitude particularly below 100 m. This type of wind shear is similar to that which often presents pilots with aircraft landing difficulties in the early morning hours.

Figure 11 is a plot of surface shear stress as a function of the dimensionless stability variable μ. Data points for $Ro \approx 10^7$ as taken from Tennekes summary of data [14] are included on the plot. The model predictions show a hysteresis loop with the

surface shear stress significantly larger when the stability is increasing (i.e., surface heat flux decreasing) rather than decreasing. The data show some scatter, particularly at neutral conditions, but tend to agree with the upper bound of the model prediction. We know of no good reason for this bias. However, it may be noted that the transition from +30 to -50 in the morning only takes about 1/3 the time that the reverse transition takes in the evening so more time is available for obtaining data along the upper boundary.

The preferred way of presenting data on surface shear stress and wind angle in the literature appears to be in terms of the variation in the parameters required to fit a logarithmic variation between u and z_o. We follow the notation established in the Russian literature [15] to define the two dimensionless variables

$$B = \ell n \frac{u^*}{fz_o} - k \frac{u_g}{u^*}$$

$$A = - kv_g/u^* \qquad (19)$$

where u_g and v_g are measured relative to a coordinate system aligned with the surface shear. In terms of our present variables this yields

$$A = \frac{ku_g \sin \alpha}{u^*}$$

$$B = \ell n \frac{u^*}{fz_o} - \left\{ \frac{k^2 u_g^2}{u^{*2}} - A^2 \right\}^{\frac{1}{2}} \qquad (20)$$

which are expected to be a function of stability μ only. These dimensionless variables are presented in Figs. 12 and 13. Predictions from the model yield a hysteresis loop which appears to be within the scatter of the field data. Although steady-state, dimensional analysis of the matching between the surface layer and the outer boundary layer implies that A and B should be a function of μ only [14], it seems clear that the unsteady hysteresis loop will be a function of the surface heat flux variation with time and the surface roughness. The large scatter in the data is not surprising.

For an analysis which assumes that the planetary boundary layer is always locally in steady state equilibrium, it would be necessary to have $(\partial u/\partial t)/ vf << 1$ everywhere. However, there are large regions in the space and time plots of Figs. (4) and (5) where this ratio is greater than 1. Thus, although there is an approximate equilibrium balance between production and dissipation of turbulence over most of the boundary layer, there remains significant unsteady influence on the dynamics of the boundary layer through the slow response of the mean velocities.

CONCLUDING REMARKS

Important features of the real atmospheric boundary layer which are not included in our current model are: large scale terrain roughness, geostrophic wind variations, thermal wind, moisture transport between the surface and the atmosphere, coupling of the surface temperature to surface heat flux through the soil energetics. Undoubtly, some of the model parameters will require adjustments as more realistic features are added. However, we believe the numerical results described herein demonstrate that this model is a step toward improved predictions of the turbulent dynamics within the planetary boundary layer.

ACKNOWLEDGEMENTS

This work has been partially funded with federal funds from the Environmental Protection Agency under Contract No. EPA 68-02-1310. The content of this publication does not necessarily reflect the views or policies of the U. S. Environmental Protection Agency.

NOMENCLATURE

A = dimensionless parameter used in correlating atmospheric surface shear (Eq. (20))

A_1, a = model constants

B = dimensionless parameter used in correlating atmospheric surface shear (Eq. (20))

b = model constant

f = Coriolis parameter = $2\Omega \sin \phi$

g = gravitational acceleration

k = von Kármán's constant = $u^*/(z \frac{\partial u}{\partial z})$ in the neutral surface layer

L = Monin-Obukhov length = $- u^{*3} T_o / kg(\overline{w'\theta'})_{z = z_o}$

p = pressure

q = square root of twice the turbulent kinetic energy

$\dot{Q}_R$ = strength of radiative heat sink

Ro = Rossby number based on surface conditions = u^*/fz_o

s = model constant

T = temperature

u = mean velocity component in the direction of the geostrophic wind

u_g = geostrophic wind

u^* = surface shear stress velocity = $[\overline{u'w'}^2 + \overline{v'w'}^2]^{\frac{1}{4}}_{z = z_o}$

u_i, u_j, u_k = Cartesian velocity components

v = mean horizontal velocity component normal to the geostrophic wind

V_c = model constant

w = mean vertical velocity component

x_i, x_j, x_k = Cartesian coordinates

z = vertical coordinate

z_o = surface roughness height

z_r = reference height at which surface condition is applied

α = angle to which the surface wind is rotated from the geostrophic wind direction

δ_{ij} = Kronecker delta

δ_T = height at which the turbulent energy falls to $\frac{1}{4}$ its maximum value

ϵ_{ijk} = alternating tensor

θ = potential temperature referenced to T_o

κ = coefficient of laminar diffusion for the potential temperature

Λ = macroscale of turbulent model

λ = microscale of turbulent dissipation = $\Lambda/(a + bq\Lambda/\nu)^{\frac{1}{2}}$

μ = stability parameter = ku^*/fL

ν = kinematic viscosity

ρ = density

ϕ = latitude

Ω = earth's rotation, $\Omega_i = \Omega\ (0, \cos\phi, \sin\phi)$

Superscripts

$\overline{}$ = denotes ensemble average

$'$ = denotes fluctuation about the mean

REFERENCES

1. Estoque, M.A., "Numerical Modeling of the Planetary Boundary Layer," American Meteorological Society Workshop in Micrometeorology, (Science Press, D.A. Haugen, ed.) 1973.

2. Deardorff, J.W., "Three-Dimensional Numerical Modeling of the Planetary Boundary Layer," American Meteorological Society Workshop in Micrometeorology, (Science Press, D.A. Haugen, ed.) 1973.

3. Tennekes, H., "The Atmospheric Boundary Layer," Physics Today, 1974, 27, 52-63.

4. Donaldson, Coleman duP., "Construction of a Dynamic Model of the Production of Atmospheric Turbulence and the Dispersal of Atmospheric Pollutants," American Meteorological Society Workshop in Micrometeorology, (Science Press, D.A. Haugen, ed.) 1973.

5. Bradshaw, P., "The Understanding and Prediction of Turbulent Flows," Aeronautical Journal, 1972, 403-418.

6. Lumley, J.L. and Khajeh-Nouri, B., "Computational Modeling of Turbulent Transport," (to be published in the Proceedings of the Second IUTAM-IUGG Symposium on Turbulent Diffusion in Environmental Pollution).

7. Mellor, G.L., "Analytic Prediction of the Properties of Stratified Planetary Surface Layers," J. Atmospheric Sciences, 1973, 30, 1061-1069.

8. Wyngaard, J.C., Coté, O.R., and Rao. K.S., "Modeling the Atmospheric Boundary Layer," (to be published in the Proceedings of the Second IUTAM-IUGG Symposium on Turbulent Diffusion in Environmental Pollution).

9. Shir, C.C., "A Preliminary Numerical Study of Atmospheric Turbulent Flows in the Idealized Planetary Boundary Layer," J. Atmospheric Sciences, 1973, 30, 1327-1339.

10. Wyngaard, J.C., "Notes on Surface Layer Turbulence," American Meteorological Society Workshop in Micrometeorology, (Science Press, D.A. Haugen, ed.) 1973.

11. Lewellen, W.S., Teske, M., and Donaldson, Coleman duP., "Application of Turbulence Model Equations to Axisymmetric Wakes," A.R.A.P. Rept. 191, 1973 (to appear in the AIAA J.).

12. Lewellen, W.S. and Teske, M., "Prediction of the Monin-Obukhov Similarity Functions from an Invariant Model of Turbulence," J. Atmospheric Sciences, 1973, 30, 1340-1345.

13. Deardorff, J.W., "Numerical Investigation of Neutral and Unstable Planetary Boundary Layers," J. Atmospheric Sciences, 1972, 29, 91-115.

14. Tennekes, H., "Similarity Laws and Scale Relations in

Planetary Boundary Layers," American Meteorological Society Workshop in Micrometeorology, (Science Press, D.A. Haugen, ed.) 1973.

15. Monin, A.S., and Yaglom, A.M. Statistical Fluid Mechanics, MIT Press, 1971.

16. Hess, Dale, Unpublished seminar.

17. Businger, J.A., Wyngaard, J.C., Izumi, Y., and Bradley, E.F., "Flux-Profile Relationships in the Atmospheric Surface Layer," J. Atmospheric Sciences, 1971, 28, 181-189.

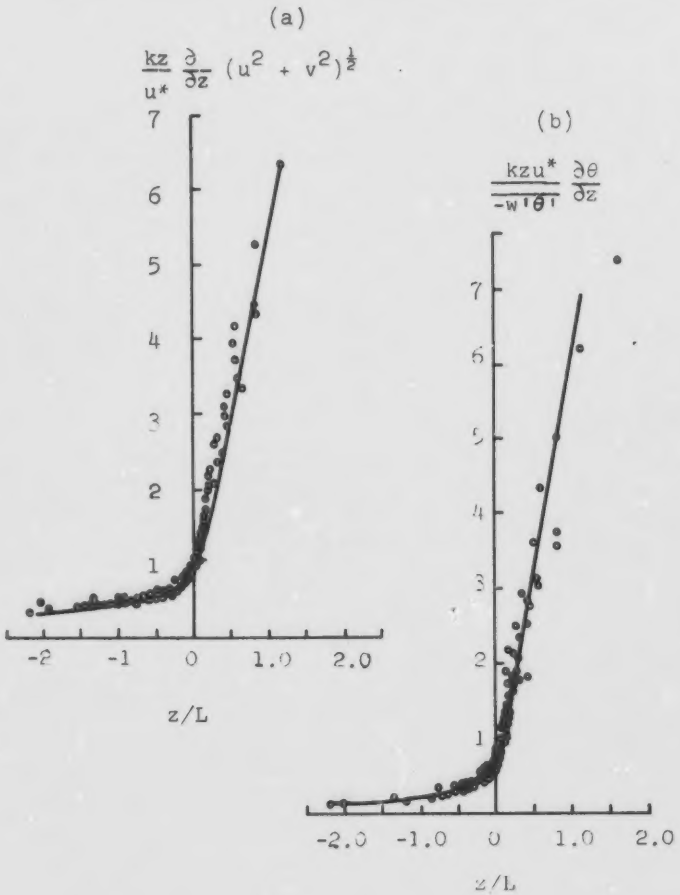

Fig. 1. Normalized (a) velocity gradient and (b) temperature gradient in the surface layer as a function of height normalized by the Monin-Obukhov length. —— model predictions [12], o observations [17].

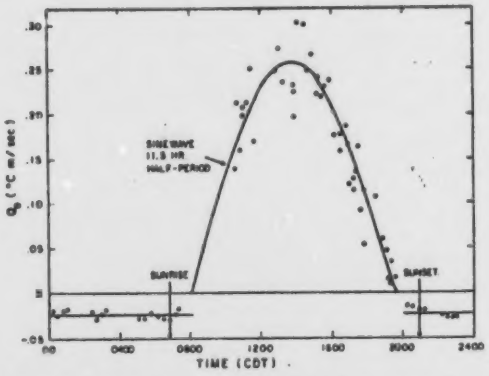

Fig. 2. Surface heat flux variation used in the diurnal calculation as taken from Ref. [10]

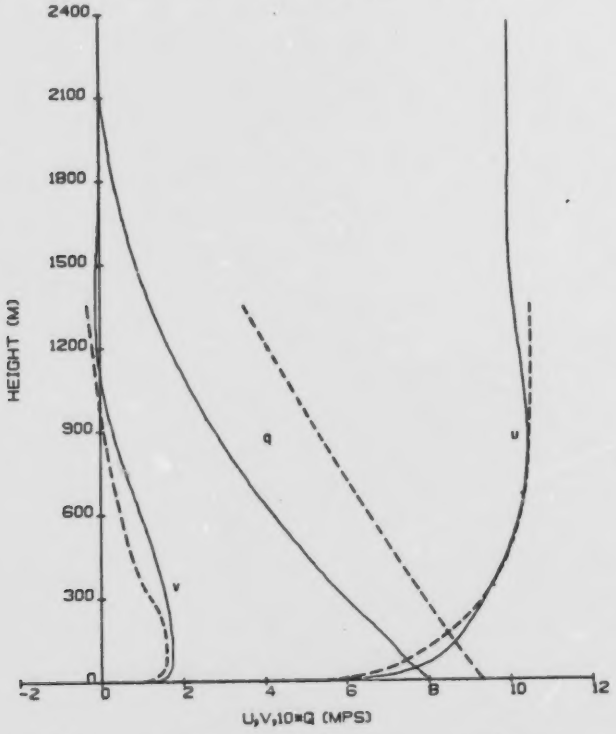

Fig. 3. Model predictions for velocity distributions in the steady state, neutral boundary layer (z_o = 0.008 m, f = 10^{-4} sec^{-1}, u_g = 10 m/s); --- Deardorff's model predictions for similar surface conditions and a fixed boundary layer height of 0.45 u^*/f (Ref. [13]).

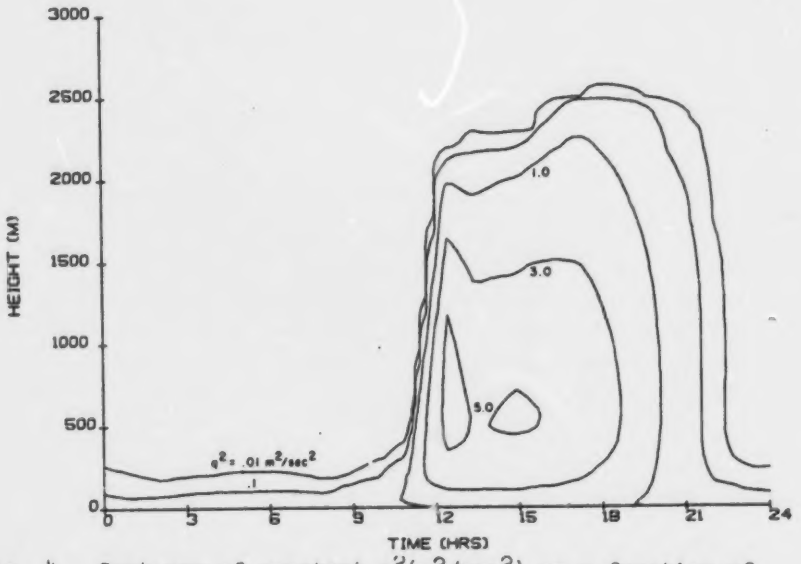

Fig. 4. Contours of constant $q^2(m^2/sec^2)$ as a function of altitude and time for one day. (z_o = 0.008 m, $f = 10^{-4}$ sec^{-1}, u_g = 10 m/sec, $\overline{w'\theta'}_o(t)$ as given in Fig. 2.)

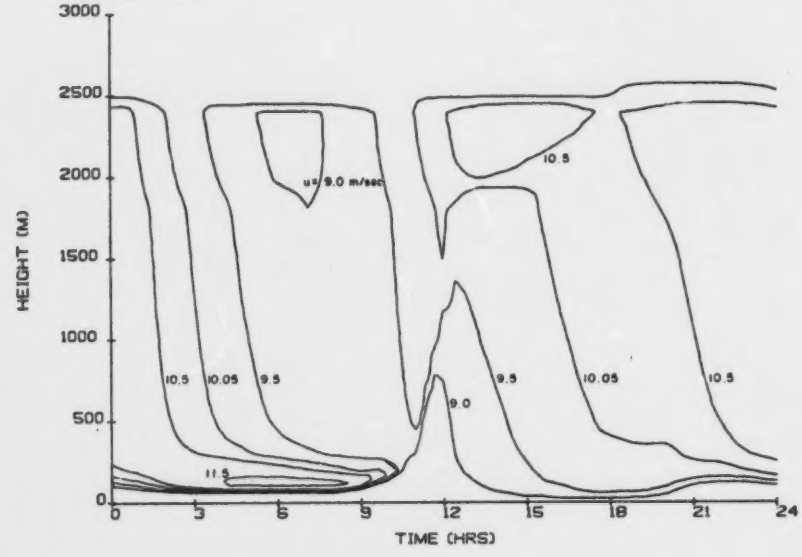

Fig. 5. Contours of constant u velocity (m/sec) parallel to the geostrophic wind as a function of altitude and time for the same conditions as Fig. 4.

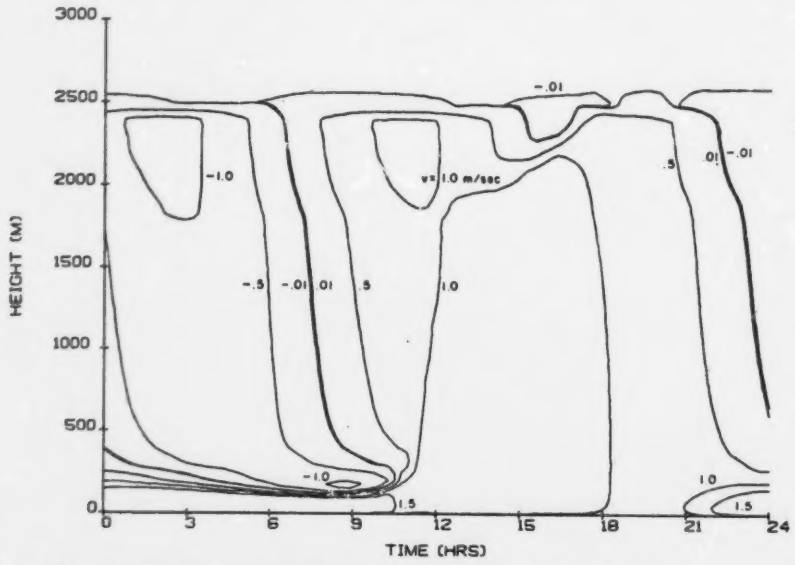

Fig. 6. Contours of constant v velocity (m/sec) normal to the geostrophic wind as a function of altitude and time for the same conditions as Fig. 4.

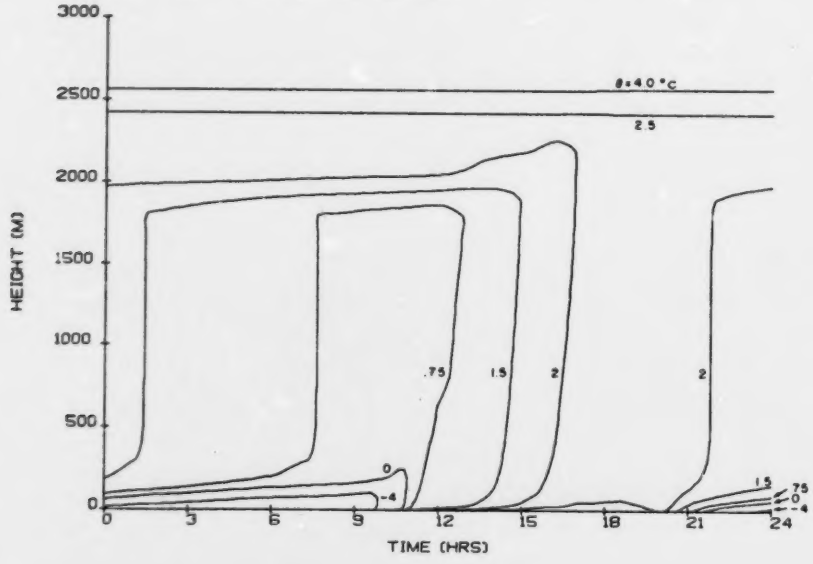

Fig. 7. Contours of constant potential temperature θ (^{o}C) as a function of altitude and time for the same conditions as Fig. 4.

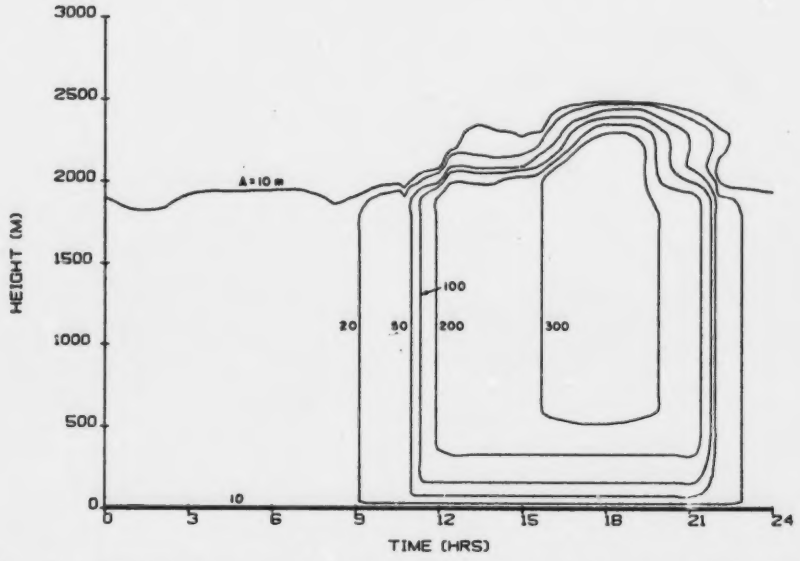

Fig. 8. Contours of constant length scale Λ (m) as a function of altitude and time for the same conditions as Fig. 4.

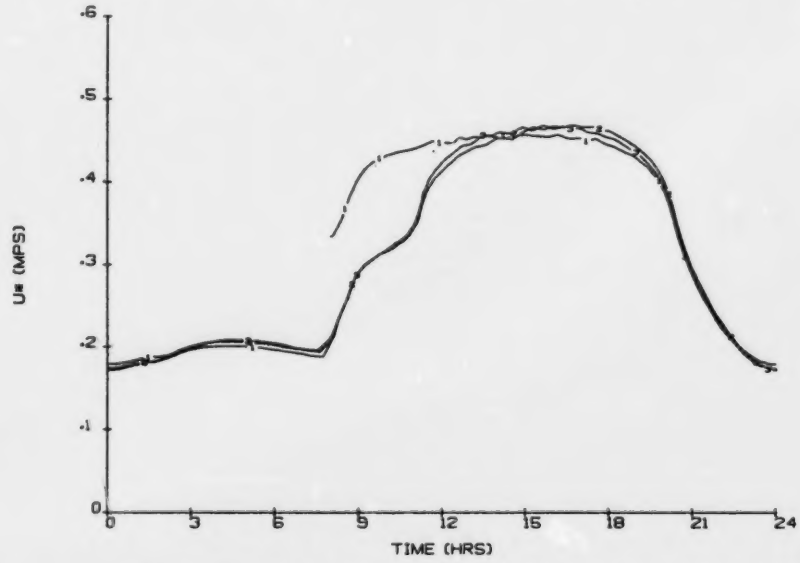

Fig. 9. Surface shear stress u* (m/sec) as a function of time -1- first day, (starting from steady state, neutral conditions) -2- second day, -3- third day.

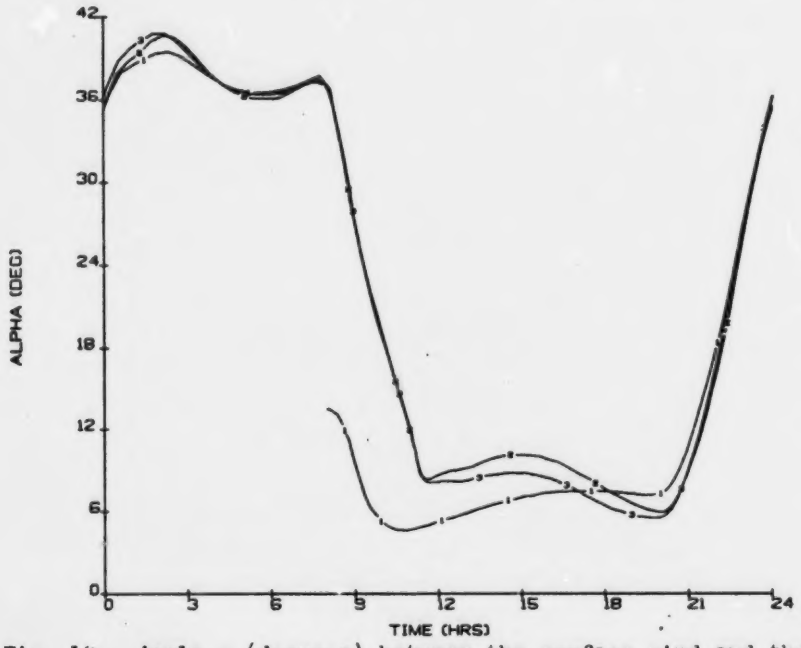

Fig. 10. Angle α (degrees) between the surface wind and the geostrophic wind as a function of time. -1- first day, -2- second day, -3- third day.

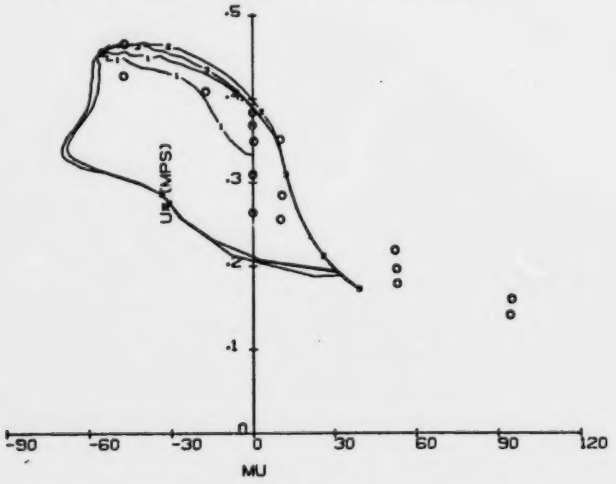

Fig. 11. Surface shear stress u^* (m/sec) as a function of the dimensionless stability variable μ. -1- first day, -2- second day, -3- third day. Data points o taken from Ref. [14].

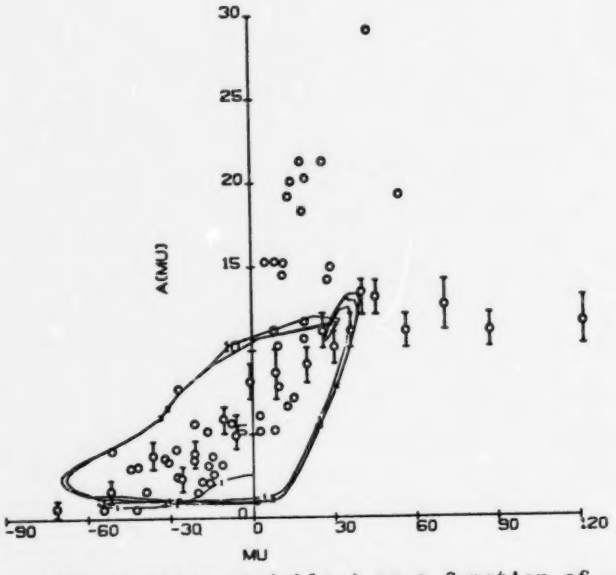

Fig. 12. Dimensionless variable A as a function of μ. -1- first day, -2- second day, -3- third day. Data points o taken from Ref. [14] and ⊖ from Ref. [16].

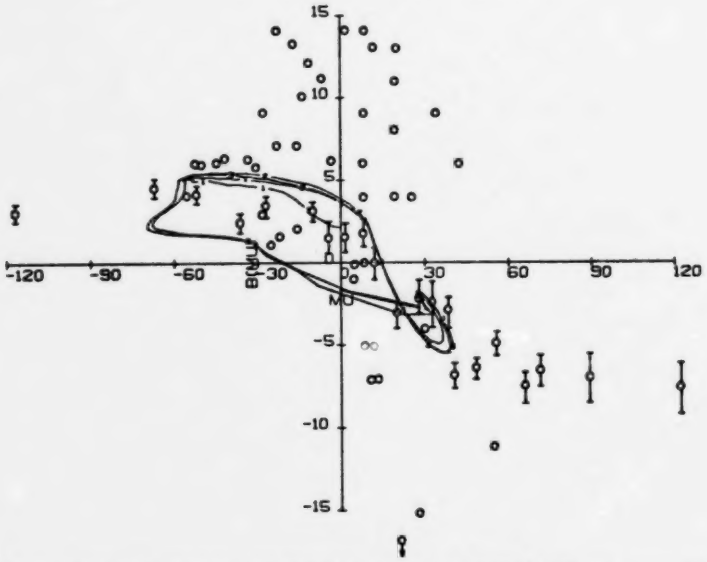

Fig. 13. Dimensionless variable B as a function of μ. -1- first day, -2- second day, -3- third day. Data points o taken from Ref. [14] and ⊖ from Ref. [16].